# MOLECULAR MODELING OF SOLUTION-PROCESSED GRAPHENE NANORIBBONS

A Dissertation
Presented to the Faculty of the Graduate School
of Cornell University
in Partial Fulfillment of the Requirements for the Degree of
Doctor of Philosophy

by
Jonathan David Saathoff
August 2016

# MOLECULAR MODELING OF SOLUTION-PROCESSED GRAPHENE NANORIBBONS

Jonathan David Saathoff, Ph.D.

Cornell University 2016

There has been much recent success in producing solution-processed graphene nanoribbons (GNRs). These GNRs, built up from smaller chemical precursors, have desirably small widths and pristine, functionalizable edges for use in electronic applications. However, there are difficulties associated with their fabrication. When the GNRs are synthesized in solution, they exhibit strong interactions between each other, causing them to aggregate unless specific solvents or functional groups are used. Rather than the trial-and-error approach that is typically used to determine the optimal solvent/functional group combination, this dissertation investigates using molecular modeling as a tool to understand how various edge functionalizations act in solution as well as using modeling as a tool to screen possible candidates for maximizing the GNRs' dispersibility. In this dissertation, the binding enthalpies of GNRs with many different edge-configurations will be examined in two different solvents: water and *n*-methyl-pyrrolidone. Here, a qualitative description of the disposition of different functionalizations and aggregate morphologies will be described as well as their relative enthalpies of binding. This will demonstrate how the functional groups, GNRs, and solvent interact with each other as well as provide information on what parameters would promote dispersion over aggregation. Second, the results of more computationally expensive free energy calculations applied to the aggregation of GNRs will be discussed. Energy barriers to aggre-

gation are used to rank the ability of different edge-configurations to promote dispersibility. Since this property is path dependent (the GNRs can approach each other following different trajectories), two entirely different paths – face-to-face and sliding – are followed, each showing the similar trends. Finally, the electronic properties of functionalized GNRs and their aggregated forms will be presented. This includes single-particle excitations (band structures) and double-particle excitations (optical spectra) as calculated by many body perturbation theory. These results will be compared to previous experimental work where solution-processed GNRs are used to fabricate field effect devices [1].

# BIOGRAPHICAL SKETCH

Jonathan was born in 1986 and was raised in McHenry, IL. He went to Northwestern University to study Chemical Engineering from 2005 to 2010 earning a Bachelors in Science Degree. In that time, he participated in the cooperative engineering program and worked at Applied Thin Films, Inc. from 2007 to 2010. In addition he worked in Prof. John Torkelson's lab at Northwestern at 2010. In August 2010, he began attending Cornell University's school of chemical and biomolecular engineering. There, he joined Prof. Paulette Clancy's group to study the molecular modeling of electronic materials. He finished in May 2016 to work at ExxonMobil's Corporate Strategic Research.

This dissertation is dedicated to my parents, David and Cheryl, for their patience with my excessively long education.

# ACKNOWLEDGEMENTS

First, I would like to thank Paulette Clancy for her remarkable patience as my advisor, and the enormous amount of positive support she provided through finding new opportunities for me, driving me towards more ambitious goals, and financially supporting my research so that I only rarely had to TA. While it goes without saying this work would have been impossible without her, I am very thankful for her giving me the opportunity to learn and apply molecular modeling techniques that I will continue to use for the foreseeable future.

Next I would like to thank my committee: Tobias Hanrath, Richard Hennig, and William Dichtel, for providing critique of my work through my A and B exams. I would also like to thank Mike Thompson for stepping in as a minor committee member after Hennig moved to the University of Florida.

In addition to thanking William Dichtel for being a committee member, I also deeply appreciate working with him as an experimental collaborator. His group provided experimental inspiration for the work this dissertation covers in addition to other projects. I would also like to thank his students, especially Hasan Arslan, Sam Hein, Colin Crick, and Fernando Uribe Romo, with whom I worked on those projects. Another collaborator I am deeply indebted to is Lynn Loo for her support through the graphene nanoribbon project and for the opportunity to work with her group one summer to make and model organic photovoltaic devices. I would like to thank Jia Gao for his relentless efforts to get the experimental graphene nanoribbon work published. I would also like to thank Anna Hiszpanski for our collaboration to understand the electronic properties of contorted hexabenzocoronenes.

I appreciate collaborating with the experimental groups lead by Zhenan Bao and M. Benedetta Casu. I enjoyed working with the materials being studied in these groups as well as learning about the computational techniques necessary to study them.

There are many people who I worked with, and received help from, in the Clancy group over the years for which that I am extremely thankful, including students Rebecca Cantrell, Alex Raymunt, Ananth Kaushik, Krishna Iyengar, Vikram Thapar, Kristina Lenn, James Stevenson, Victoria Sorg, Yaset Acevedo, Henry Herbol, Ryan Heden, Mardochee Reveil, Taha Ezzyat, Cheng-Wei Lee, Nikita Sengar, Binit Lukose, Blaire Sorenson, Sai Vineeth Bobbili, and Jingyang Wang. I would especially like to thank Ananth Kaushik for his mentorship in my early years and introducing me to LAMMPS and Marcus Theory. Outside of work, I would like to thank Rambert Nahm, Sarai Meyer, Poornima Padmanabhan, and Sai Pooja Majahan for their friendship and support over the years, as well as any welcomed distractions including going out to eat, board and card game nights, dinner parties (with absolutely amazing food prepared by Sarai), and the ill-fated book club. Without these distractions, it would have been much more difficult to get through the last few years.

Finally, I would like to thank Intel for their generous donations in terms of computational resources. Without their assistance, my thesis work would have been rendered impossible. With that, I also appreciate all of the help from Steve Thompson. He was very responsive to any troubles I had and his dry humor made the most frustrating problems in terms of allocating computational resources at least a little bit entertaining. Also, I would like to thank Extreme Science and Engineering Discovery Environment (XSEDE), whose supercomputing resources were used for parts of this work. The optical excitation calculations would not have been possible without the computational resources provided by Peter Frazier. The majority of the funding of this work was provided by the NSF and the Semiconductor Research Corporations Nanoelectronics Research Initiative, without whom this work would not have happened.

## TABLE OF CONTENTS

# LIST OF TABLES

# LIST OF FIGURES

CHAPTER 1

# INTRODUCTION

## 1.1 Graphene

Graphene has been under intense investigation since the seminal work of Novoselov and Geim in which they isolated few-layer and single-layer graphene [2]. This was accomplished through mechanical exfoliation, where tape was used to remove layers of graphite from highly oriented pyrolytic graphite (HOPG) that was bound to glass using photoresist. After many applications of the tape, the photoresist was dissolved in acetone. Few-layer and single-layer graphene were then obtained by dipping silicon into an acetone bath. Two-dimensional (2D) crystals, such as this suspended graphene, was previously thought to be inherently unstable [3]; however, this method has been shown to be successful with graphene as well as other 2D materials [4]. This work inspired efforts to investigate other 2D materials of which $MoS_2$, $TaS_2$, BN, and $NbSe_2$ are examples [5, 6].

While the creation of a method for producing suspended 2D crystals was interesting, graphene has a number of unusual properties that could make it particularly useful for a number of applications. For example, graphene boasts electron mobilities of over 200,000 $cm^2/Vs$ [7, 8], and exhibits current densities several times that of copper [9, 5]. Graphene has an intrinsic breaking strength and Young's modulus of 130 GPa and 1 TPa, respectively [10]. A single layer also has an opacity of 2.3% across the visible spectrum, making it suitable to be used as a transparent electrode. (Interestingly, the opacity is $\pi a$ where $a$ is the fine structure constant. A light transmission experiment can be used to estimate its value) [11]. In addition, graphene can transmit heat at 3000 W/mK [12].

Since the original low-technology method to create graphene, a number of additional methods have been developed to produce the material. Graphene can be dispersed by ultrasonication from HOPG in solvents such as *n*-methyl-pyrollidone (NMP) [13]. In chemical exfoliation, graphite is oxidized to form layers of graphene oxide, which are soluble in polar solvents. When the graphene oxide is reduced in solution, graphene sheets of moderate quality remain [14, 15]. Deposition of organics on copper can be used to produce single layers of graphene through chemical vapor deposition [16]. Finally, an older method of producing graphite from annealing SiC [17] has been fine-tuned to produce single layers of high quality graphene sheets [18, 19].

Due to graphene's many unique properties and a variety of viable fabrication methods, there are a number of potential applications for the material. Taking advantage of graphene's high conductivity, transparency, and flexibility, researchers are developing graphene as a replacement for indium tin oxide (ITO) as a transparent electrode in flexible electronics applications [20]. The low dimensionality and high mobility of graphene can potentially be used to make high frequency transistors [21] and transistors for logic applications [22]. Graphene can be used as an anode material for lithium storage in batteries [23]. Taking advantage of its unusual mechanical properties, graphene can be used to make a number of nanocomposites [24]. With its unique properties and a number of directions can be taken to manufacture graphene for unusual applications, it is likely that graphene will be an active area of research for some time.

Graphene's electronic properties ultimately derive from its unique electronic structure. The electronic structure of graphene was first studied *via* a tight binding approach as a first step towards studying graphite almost seventy years ago [25]. The tight-binding model had the following form:

$$E_{\pm} = \pm t\sqrt{3 + 2cos\left(\sqrt{3}k_y a\right) + 4cos\left(\frac{\sqrt{3}}{2}k_y a\right)cos\left(\frac{3}{2}k_x a\right)} \tag{1.1}$$

where $E_{\pm}$ make up the valence and conduction bands, $t$ is the nearest neighbor hopping energy (2.8 eV), and $a$ is the lattice constant (1.42 Å). A representation of this band structure is shown in Figure 1.1.A. At points K ($k_x = \frac{2\pi}{3a}$, $k_y = \frac{2\pi}{3\sqrt{3}a}$) and K′ ($k_x = \frac{2\pi}{3a}$, $k_y = -\frac{2\pi}{3\sqrt{3}a}$), the bands come together at a singular point. Around these points, a simple first-order expansion can be written:

$$E_{\pm} \approx \pm v_F\,|\mathbf{q}| \tag{1.2}$$

where $v_F$ is the Fermi velocity ($3ta/2$), and $\mathbf{q}$ is the vector $\mathbf{k} - \mathbf{K}$ or $\mathbf{k} - \mathbf{K}'$[26]. This is shown in Figure 1.1 C.

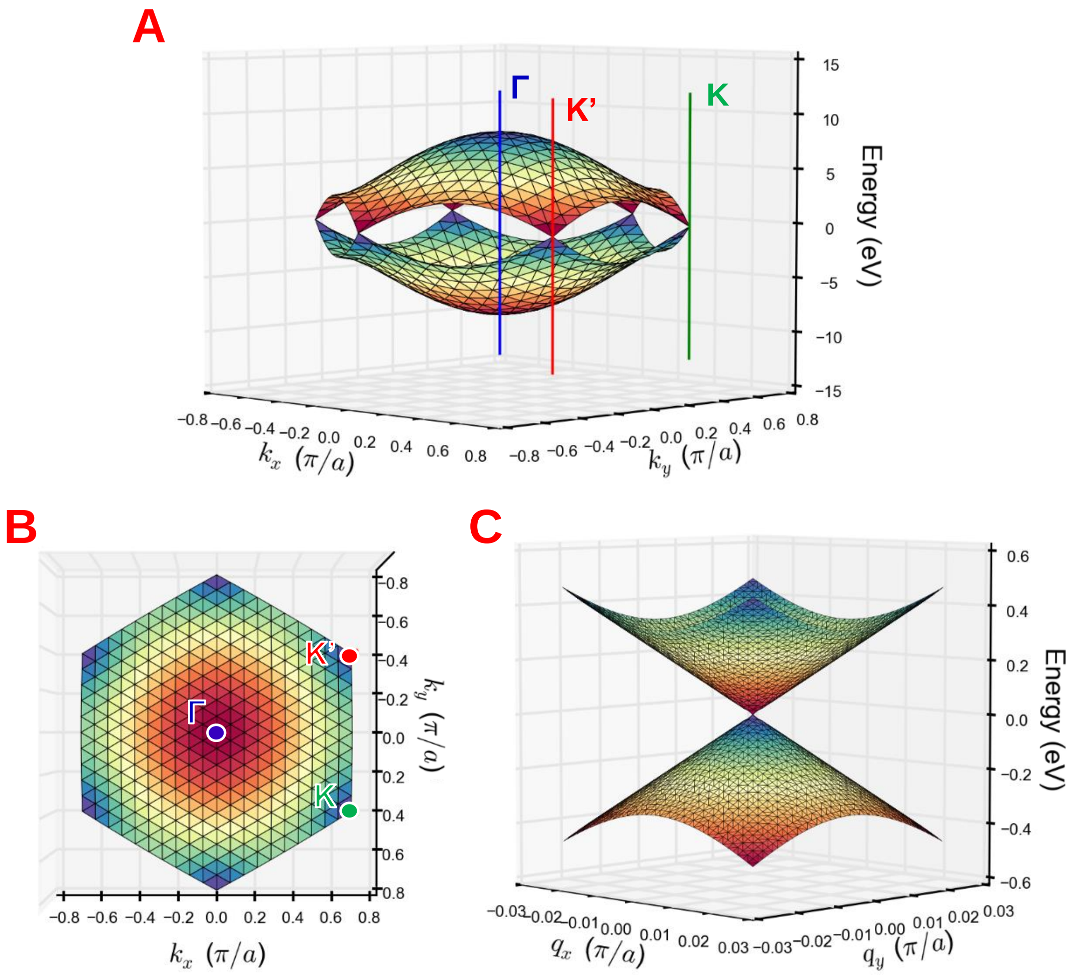

Figure 1.1: Two-dimensional band diagrams of graphene following Equation 1.1. (A) shows both conduction and valance bands in the first Brillouin zone. (B) provides a top view of (A) showing the exact location of the high symmetry points. (C) shows a zoomed-in view of the Dirac points centered around $\mathbf{q} = \mathbf{k} - \mathbf{K}$ and $\mathbf{q} = \mathbf{k} - \mathbf{K}'$. In all cases, $a$ is the lattice parameter (1.42 Å). The color is added to emphasize depth.

Equation 1.2 is also a solution to the Dirac Equation for free, massless fermions, with the speed of light being replaced with $v_F = 1 \cdot 10^6 m/s$. For this reason, physicists have wanted to synthesize graphene as a model system to study quantum field theory since the 1980s [27, 28]. For the purposes of this dissertation, what is immediately important is that the effective mass of a charge carrier is zero about the points K and K′. This, in combination with the high Fermi velocity, leads to ballistic transport and the high mobilities found in graphene [26]. This has inspired many researchers to investigate the use of graphene in electronic applications, such as field effect transistors for logic applications.

The electronic structure shown in Figure 1.1 also demonstrates a serious problem using pristine single-layered graphene as a gate material for a FET. While graphene has been shown to have high mobilities and a demonstrable field effect [2], it is a semi-metal with no band gap. Without a band gap, there is no distinction between “on” and “off” states, which is necessary for the switching function of a transistor. In order for a potential channel material to be useful for application in a FET, the ratio of current between “on” and “off” states must be between $10^4$ and $10^7$ [22]. Since bulk graphene always exists in an “on” state, this is not the case.

Different strategies have been attempted to induce a band gap in graphene. One method involves making bilayer graphene. With two layers of graphene and the addition of an electric field perpendicular to the sheets, a band gap can be opened [29, 30]. Also, if graphene is strained, it will produce a band gap [31]. This has also been seen in silicon carbide [32]. However, both these methods produce band gaps that are too small for the necessary on/off ratios [26]. Another method involves reducing the width of graphene sheets to a few nanometers. These graphene nanoribbons, or GNRs, have band gaps that equal, and even surpass, that of silicon [33]. Therefore, they have sufficient band gaps for logic application. GNRs will be discussed more thoroughly in the next section.

## 1.2 Graphene Nanoribbons

Depending on their structure, there is great variability in the electronic properties of GNRs. While there are many ways to cut GNRs from a sheet of graphene, there are two extreme cases in the resulting material: GNRs with zigzag edges and GNRs with armchair edges (Figure 1.2). Early tight-binding calculations showed that the electronic properties of GNRs vary greatly depending on whether or not they fall into either of these two categories, and their width. In tight-binding calculations, zigzag ribbons are shown to have flat valence and conducting bands at their $\Gamma$ point, with the related electronic states residing predominately on the GNR's edges. Armchair GNRs, which will be the focus of this dissertation, have conduction and valence states that cover either face of the GNR. Tight-binding results show that there are three families of widths of armchair GNRs that have different electronic properties, which are dependent on width. With N being the number of carbon dimers that make up the width of a GNR and M being some integer, GNRs with N=3M+2 are metallic (Figure 1.2). GNRs with N=3M and N = 3M+1 are semiconducting, with the latter typically having a slightly larger band gap than the former. The band gaps of the two semiconducting variants increase with decreasing GNR width [34].

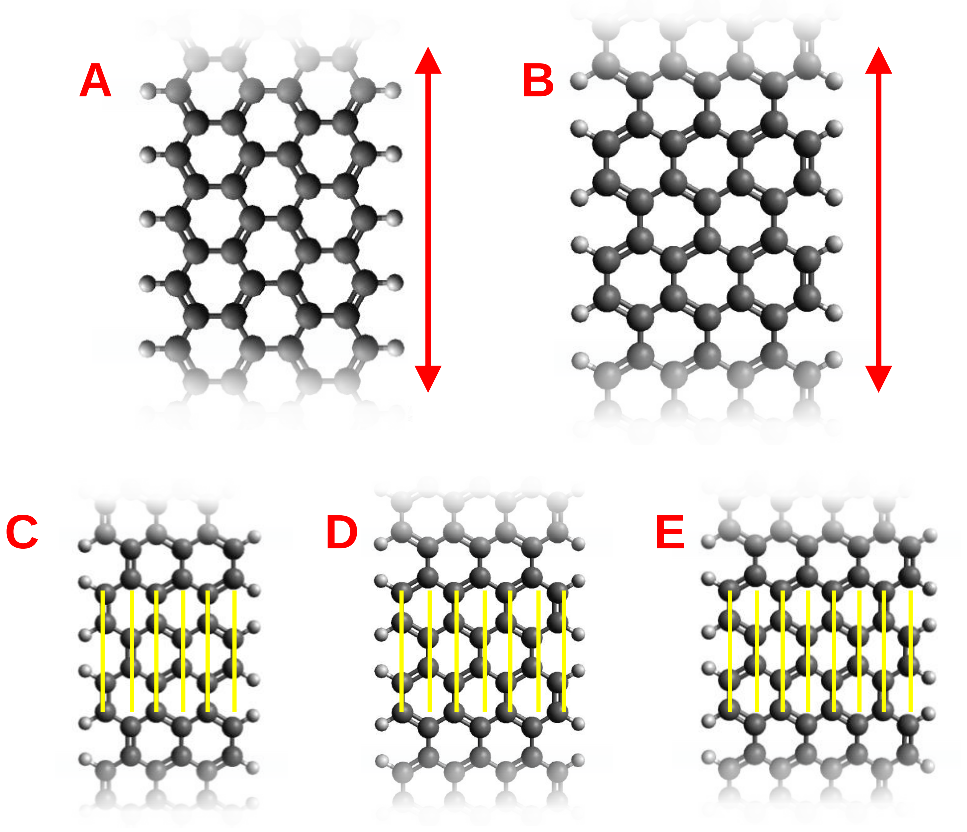

Figure 1.2: GNRs with different edge configurations extending in the vertical direction. (A) and (B) are zigzag and armchair GNRs, respectively. (C), (D), and (E) are armchair GNRs with different numbers of carbon dimers indicated by the yellow lines. With M=2, (C) is a N=3M semiconducting GNR, (D) is a N=3M+1 semiconducting GNR, and (E) is a N=3M+2 metallic GNR.

With higher levels of theory, more details about armchair GNRs can be found. Density Functional Theory (DFT) studies made on GNRs showed that it is not only nanoconfinement that contributes to the band gap (as demonstrated by the tight binding study). Edge effects - different electronic environments of the carbon atoms on the edges *vs.* the center of the GNR - can also induce a band gap. These edge effects open band gaps further, even causing the metallic family of armchair GNRs to exhibit a band gap [35]. A limitation with using DFT is that it is incapable of being used to accurately calculate band gaps. To build on past studies, more accurate $G_0W_0$ calculations have been made to estimate the electronic band gap. While these calculations followed the trends of the different calculation methods used before, the magnitudes of the band gaps increased. For the family of armchair GNRs with N=3M+1, GNRs that are 3.7 Å, 7.7 Å, and 10.6 Å have band gaps at 5.5 eV, 3.9 eV, and 3.0 eV, respectively. Since these band gaps are significantly larger than silicon (1.1 eV), they will be capable of producing on/off ratios within the range of $10^4$ and $10^7$, making them viable, in principle, for logic applications [33].

Like sheets of graphene, there are multiple methods for producing GNRs. These fabrication methods fall into roughly two categories: "top-down" and "bottom-up" methods [36]. In top-down processes, a material, such as a graphene sheet, is physically cut into smaller GNRs. Whereas, in bottom-up processes, material is transformed or built up from appropriate molecular precursors to form GNRs effectively ring-by-ring. A simple example of a top-down approach involves cutting GNRs out of graphene sheets *via* electron beam lithography [37, 38]. Carbon nanotubes can also be opened by chemical oxidation or plasma etching to form GNRs [39, 40]. Unfortunately, it is often difficult to obtain regular edge geometries and widths, which are necessary to get optimal and consistent electronic properties [22]. Alternatively, bottom-up processes involve polymerizing bulky monomer units and then, through an oxidative cyclodehydrogenation step, form graphene nanoribbons. These GNRs can be fabricated with a variety of polymerization methods [41, 42, 43, 44, 45, 46]. In addition, the synthesis process can be surface-catalyzed [47, 48]

## 1.3 Dispersing Graphene-Based Materials

In many of the previously described fabrication methods for graphene, it has become apparent that the graphene must be dispersed at some stage in the process. In addition, dispersing graphene is important for some applications, such as making composites [49]. The simplest method to do this is to use a solvent that readily disperses graphene. Like carbon nanotubes, graphene is readily dispersed in NMP [50, 13]. Further work showed that Hansen solubility parameters could be estimated for graphene, in which the solutes hydrogen-bonding, polarity, and dispersion characteristics can be quantified for matching with preferred solvents [51]. The use of Hansen solubility parameters here could be considered inappropriate, since graphene is typically dispersible, but not soluble. A "good" solvent in the case of graphene is one in which a large concentration of graphene can be dispersed and one that takes a long time for the graphene to aggregate out of dispersion. There were a couple of computational Molecular Dynamics (MD) studies to understand why different solvents dispersed graphene better than others [52, 53]. It was found that a solvent that was adept at wetting graphene formed metastable solvent layers that provided a large activation energy for graphene to fully aggregate.

In addition to choosing dispersible solvents, an alternative approach is to introduce other molecules into the "solution" with graphene that can aid in dispersion. A very common method that has been used successfully with carbon nanotubes involves adding a detergent like sodium dodecyl sulfate [54, 55, 56]. Here, the hydrophobic end of the detergent adsorbs onto the graphene sheet, while the charged, hydrophilic end is soluble in solvents such as water. As an uncharged alternative, block copolymers can be added where one block adsorbs onto the graphene and the other is soluble in the solvent. This provides steric repulsion between graphene sheets that are in close proximity with each other [57]. Even single-block, partially adsorbed polymers can play this role [58].

A more aggressive step to dispersing and even solubilizing graphene is to functionalize graphene. In a similar way to the strategy of adding surfactants, the addition of charged groups has also been employed. A simple way to do this is by chemically oxidizing graphene to form graphene oxide [59, 60]. The addition of charged oxide groups permit the sheets to be soluble in water. Further reduction removes the oxide groups to form defective graphene sheets. However, graphene in either oxidized or reduced form is detrimental to many of the properties that are graphene's more attractive characteristics. In addition to oxidizing graphene, additional groups can be added to provide steric hindrance to the aggregation process, much like the addition of block copolymers to the dispersing liquid [61, 62].

In the synthesis of bottom-up GNRs and nanographenes (*i.e.,* large, non-polymerized polyaromatic molecules), the incorporation of functionalities is relatively straightforward because they can be included in the chemical precursors for these products. Using various branched and linear alkyl chains along the edge a nanographene (hexi-peri-hexabenzocoroene), Kastler *et al.* determined which side-chain made the nanographene the most dispersible [63]. The side-chains that were successful were then applied to GNRs in order to disperse them [46]; however, dispersing these GNRs remains difficult. While it is possible to use intuition to design dispersing edge groups [64], little has been done to understand the mechanism by which these dispersing edge groups work which, in turn, has prevented our ability to design dispersing, or even solubilizing, groups more intelligently.

## 1.4 Dissertation Summary

As already stated, dispersing graphene in solution is difficult. The large-area surfaces consist of strongly self-interacting carbon sheets which give the material a strong tendency to aggregate. While many strategies exist to mitigate this problem, each one has their own difficulties: Solvents might be expensive or have undesirable properties; additives might have undesirable effects on the final electronic properties of the materials; and functionalization might damage the graphene sheets. In addition, the extent of the dispersion is frequently insufficiently high for subsequent processing, such as deposition of single GNRs on a substrate. Therefore, there is still an unmet need to understand and hence provide better solutions to this problem.

With solution-processed, bottom-up GNRs, edge functionalization adds an additional “knob” with which to tune the properties of the material. Branched alkane side-chains have been used in the past to disperse GNRs; however, aggregation was still admitted to be a problem. This is a common way to disperse large polyaromatics, and have been studied on other materials. However, various side-chains are typically chosen by a trial-and-error process. When a particular edge-chain is found to be successful in the laboratory, the reason why it works is generally left as a mystery because the mechanism of dispersion is not easily resolvable through experiment. However, molecular simulation methods, such as Molecular Dynamics (MD), can be used to build a molecular-level "picture" of the mode of action of these side-chain choices, and computational methods show promise to being used as a predictive tool.

In this dissertation, the MD method will be used to investigate the properties of a variety of edge-chains on GNRs in different solvents. First, we will examine a wide range of linear polyethylene glycol (PEG) and *n*-alkoxy chains with different lengths and grafting densities for their ability to disperse GNRs, using a series of relatively quick simulations that probe the enthalpy of the solution. Here, the focus will be to calculate the edge-chain dispositions, aggregate morphologies, and aggregation enthalpies. These simulations are meant to provide a rapid screen of candidate side-chain/solvent combinations that efficiently finds promising edge-chain configurations for dispersing GNRs. Next, a few experimentally relevant edge-chain configurations will be examined in more detail using more computationally expensive free energy calculations to look directly at the mechanism of aggregation and inherently incorporate entropic contributions that could be significant [46].

While there have been many first-principles studies of the electronic properties of GNRs, they are typically done on pristine GNRs with hydrogen-terminated edges. However, the GNRs that we, and the overwhelming majority of experimental groups, are investigating are not hydrogen-terminated, but have side-chains that may or may not wrap around the GNRs. In addition, GNRs are highly likely to aggregate, potentially insulating them from one another; this, again, will affect the electronic properties of the material. We have investigated the effect of aggregation and of side-chains on the GNRs using both Density Functional Theory (DFT) and $G_0W_0$/Bethe-Salpeter equation calculations to understand how both the electronic and optical band gaps change under these non-ideal circumstances. We will then compare these results with experiment [1].

CHAPTER 2

# COMPUTATIONAL METHODS

In the following chapters, we used several different computational methods to study GNRs. Throughout most of this dissertation, we will explore the properties of the GNRs in a solvent dispersion. To accomplish this, Molecular Dynamics (MD) was our primary tool. The electronic properties of the GNRs were studied using *ab initio* electronic structure calculations including both Density Functional Theory, DFT, to calculate ground state properties and built a qualitative understanding of the band gaps of different aggregated GNR structures [65, 66]. Finally, $G_0W_0$ and the Bethe-Salpeter Equation, BSE, calculations were used to study the electronic and optical band gaps of the GNRs quantitatively [67, 68].

## 2.1 Molecular Dynamics

In MD, the positions and momenta of atoms evolve with time according to Newton's laws of motion. Information from these simulations allows us to estimate the kinetic and thermodynamic properties of the GNR systems under study. The MD simulations employed the LAMMPS package (Large-scale Atomic/Molecular Massively Parallel Simulator) [69]. This software was chosen for several reasons: it is very flexible in terms of available models and methods, it runs efficiently on multiple cores in parallel, the source code is easy to read and modify, and it is very well documented. In all simulations, we employed time steps ranging from 1.0 to 2.0 fs. Long-ranged interactions (van der Waals and Coulombic) were treated with a 10.0 Å cut-off. Past that distance, a tail correction was used to estimate the long-ranged van der Waals interactions.

A particle-particle, particle-mesh scheme was used to estimate Coulombic interactions with a $10^{-5}$ error tolerance [70]. To maintain temperature and pressure at 300 K and 1 atmosphere, we used Nosé-Hoover thermostats and barostats.

### 2.1.1 General Force Field Description

Following the motion of a molecular system according to Newton's laws, requires that the forces between the atoms that comprise the system have been defined. While this could, in principle (and in fact using techniques such as Car-Parrinello MD [71]), be performed using a first principles simulation, this is often too computationally expensive. Instead, for larger-scale simulations involving thousands of atoms, it is far more common to define the inter- and intramolecular forces as simplified sets of equations for each interaction, accompanied by semi-empirically defined parameters, called "force fields". In our study, we used Jorgensen *et al.*'s Optimized Potential for Liquid Simulations All-Atom (OPLS-AA) force field for all of our MD calculations [72]. The equations used for components of this force field are the following:

$$E_{bond} = k_r (r - r_0))^2 \tag{2.1}$$

$$E_{angle} = k_\theta (\theta - \theta_0))^2 \tag{2.2}$$

$$E_{torsion} = \frac{V_1}{2}[1 + cos(\phi)] + \frac{V_2}{2}[1 - cos(2\phi)] + \frac{V_3}{2}[1 + cos(3\phi)] \tag{2.3}$$

$$E_{vdw} = 4\epsilon\left(\left(\frac{\sigma}{r}\right)^{12} - \left(\frac{\sigma}{r}\right)^{6}\right) \tag{2.4}$$

$$E_{coul} = \frac{q_1 q_2 e^2}{r} \tag{2.5}$$

which describe the bond energies ($E_{bond}$), bond-angle energies ($E_{angle}$), torsion energies ($E_{torsion}$), van der Waals energies ($E_{vdw}$) and Coulombic energies ($E_{coul}$), respectively.

In this study, two solvents were used: NMP and water. NMP represents a "good" solvent, while water is likely to be a "poor" solvent. In an analogous previous simulation study of rigid bulk graphene sheets [52], the partial charges on the NMP solvent were adjusted such that the dipole moment matched the results of DFT studies of the same system [73]. The errors in density as a result of this change were less than 1%. This same alteration was included in our model. The SPC/E model was used to represent the water force field [74]. Since no spring coefficients were incorporated in the model, the SHAKE algorithm was used to keep bonds close to their equilibrium lengths and angles [75].

### 2.1.2 GNR Force Field Description

It was unclear at the outset if a classical force field would be adequate to describe graphene. In addition, the OPLS-AA force field was parameterized for small molecules. Since bulk graphene and GNRs are not small molecules, we reinvestigated their parameterization. First, the long-ranged interactions were examined (specifically the van der Waals and Coulombic terms in the force field). Depending on the method of determining the parameters for the Lennard-Jones (LJ) function to describe van der Waals interactions, it is possible to determine different sets of LJ parameters. In several recent MD studies of graphene [76, 52], LJ parameters were used that had originally been applied to systems involving gas adsorbing on graphite [77]. Different parameterizations can also be derived from the absorption of aromatics of increasing size on graphite [78]. Finally, Quantum Monte Carlo results of the interlayer binding energy in graphite were available as an information source to obtain yet another parameterization [79]. In this study, we used the parameters determined by Cheng and Steele because a number of researchers have used them successfully for MD simulations and related them back to experiment [77, 52]. However, this is not to say that these are definitively the most accurate set of LJ parameters for this system. In a study where quantitatively accurate binding energies are required, rather than trends, this issue may need to be revisited.

The electrostatic interactions of graphene are also complicated. Due to the existence of $\pi$ electrons above and below the plane of a graphene sheet or GNR, the material has a net quadrupole moment perpendicular to the sheet. This has been studied in depth by Kocman *et al.* [80]. They found that, while the quadrupole moment has a vanishingly small effect on a system with larger graphene sheets, it can have a more significant impact on smaller graphene-based systems, like GNRs. There is always a significant change in electrostatic potential near the edge of the sheet. Even away from the edge, the quadrupole moment has some (often structure-directing) effects on the solvent. It was shown by Kocman *et al.* that the quadrupole moment of graphene may be involved with the different dispersibilities of graphene in benzene and hexafluorobenzene [80]. Without a quadrupole moment, MD simulations suggest that both solvents perform identically. However, with the inclusion of the quadrupole moment, there are higher energy barriers associated with the aggregation of graphene in hexafluorobenzene. This coincides with results from experiment that show that graphene in hexafluorobenzene is more dispersible than in benzene.

Examining differences in aggregation free energies as we vary the nature of the solvent is beyond the scope in our study. Instead, we look at the effects of a variable electrostatic charge along the edge of our GNRs, which is important because of the small dimensionality of the material. For a single benzene ring, the smallest motif representative of graphene-like materials, the OPLS-AA force field describes a single benzene ring as having a charge of -0.115 *e* for the carbon atoms and 0.115 *e* for the hydrogen atoms providing the molecule with a quadrupole moment, where *e* is the magnitude of the charge on an electron ($1.602 \cdot 10^{-19}$ C). It was necessary to test if these charges would be adequate, given a GNR of similar size to the ones that would be simulated *via* MD. To do this, the GNR shown in Figure 2.1 was simulated using DFT through Gaussian 09 [81] calculations. The structure was optimized with the 6-31G(d) basis set and a B3LYP functional [82, 83, 84]. With the same basis set and functional, the partial charges on the atoms were estimated using the Merz-Kollman scheme [85]. Since a finite GNR was used, only the middle section, away from the edge, was used in the evaluation of the partial charges. Three regions were identified: Edge hydrogens, edge carbons (bonded to edge hydrogens), and core carbons (only bonded to other carbons). The average charges for each of these respectively were 0.13 *e*, -0.185 *e*, and 0.01 *e*. Since the benzene model had no core carbons, the core charge was shifted to the edge carbons for a direct comparison. The resulting charges of 0.13 *e* for the hydrogens and 0.13 *e* for the edge carbons were very close to the OPLS-AA parameters of 0.115 *e* and -0.115*e* respectively. Since the differences between the calculated charges and OPLS-AA charges were smaller than partial charges typically used for the OPLS-AA force field (above 0.05 *e*), the OPLS-AA charges for benzene were used to simulate partial charges on the simulated GNRs, with the core carbons set to zero charge [72].

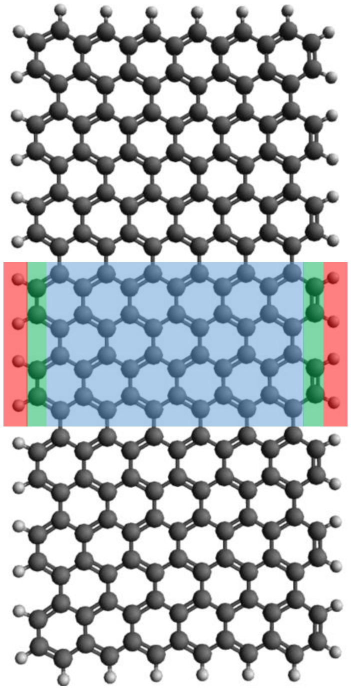

Figure 2.1: The GNR used to compare DFT calculated partial charges with the OPLS-AA parameter set. The colored blocks represent the particular atoms that were used in the analysis. The red blocks, green blocks, and blue blocks cover the hydrogen atoms, edge carbons, and core carbons, respectively.

For a few aspects of our study, having GNRs with the right bending rigidity was important in order to accurately portray the flexing of the GNRs. The bending modulus of graphene had already been calculated using *ab initio* studies [86] to be 34 kcal/mol. In order to calculate the bending modulus, cylinders of diameters from 32 nm to 65 nm were set up that were made of van der Waals spheres [87]. On each of the cylinders, the energy representative of a GNR that was 3.0 nm wide and 10.1 nm long was minimized on each of the cylinders (Figure 2.2). The difference in intramolecular potential energy between the wrapped GNRs and a flat GNR was used to calculate the bending modulus, $D$, with:

$$E_{bend} = \frac{1}{2} D W L \kappa^2 \tag{2.6}$$

where $E_{bend}$ is the energy difference just described, $W$ is the GNR width, $L$ is the GNR length, and $\kappa$ the GNR curvature. It was found that $D$ was most sensitive to altering the second Fourier coefficient, $V_2$, in Equation 2.3. We adjusted this parameter and performed iterative minimizations until the value of $D$ reached 34 kcal/mol. The final value of $V_2$ was determined to be 5.05 kcal/mol (in contrast to the default value provided by OPLS-AA of 7.7 kcal/mol) [72].

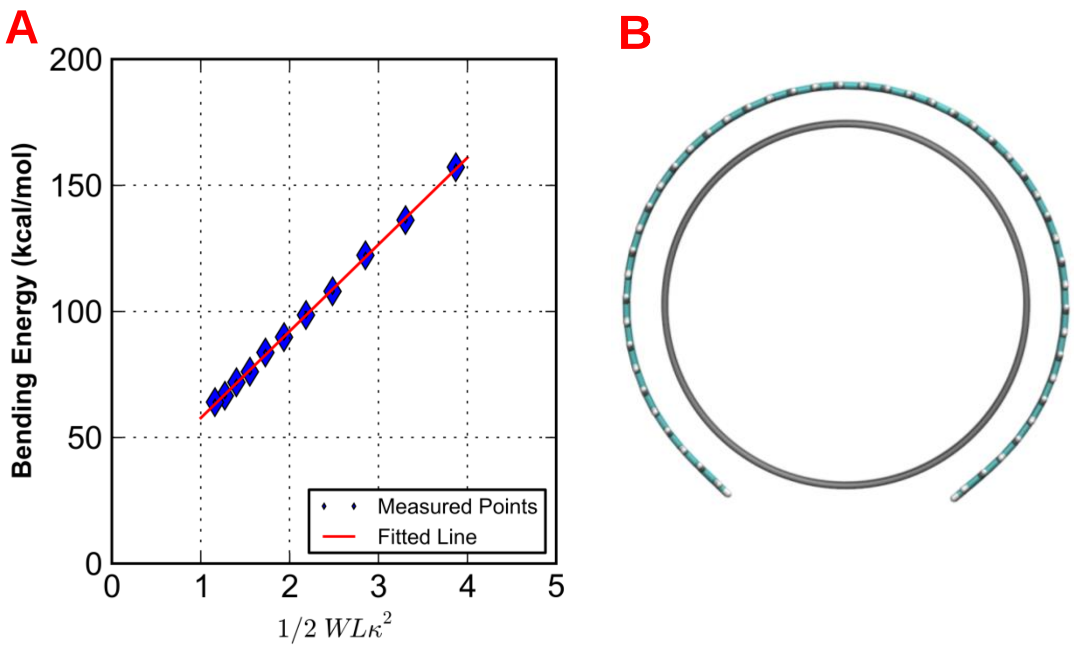

Figure 2.2: Results from simulations used to calculate bending rigidity. (A) provides a plot of the known terms on the right hand side of Equation 2.6 vs. $E_{bend}$. (B) is an example of a GNR in its energy-minimized state on a van der Waals cylinder.

### 2.1.3 Free Energy Methods

Conceptually, the calculation of enthalpies is trivial in MD simulations. The simulation only needs to be run long enough that an adequate level of precision can be gained from the respective ensemble averages. However, this is not the case with free energy values, $F$. In fact, absolute free energies are practically impossible to calculate because its value is directly related to the partition function, $Q$:

$$F = -k_B T ln(Q) \tag{2.7}$$

However, differences in free energies can be calculated [88]. The free energy difference between two states (states A and B, for example) can be related to the probability of the two states:

$$F_A - F_B = \Delta F_{A,B} = -k_B T ln\left(\frac{P_A}{P_B}\right) \tag{2.8}$$

where $P$ is the probability of the system being in either state A or B.

If a MD simulation is run and the system samples both states frequently, the free energy difference between the two should be simple to calculate. However, this case is exceptional. If the relative probability between two states is as high as 100, $\Delta F$ will be just over 2.5 kcal/mol at 300 K. For significantly higher free energy differences between different states, unrestrained MD would be incapable of adequately sampling both states in a reasonable amount of computer time. Therefore, alternative routes are required to enhance the sampling of MD simulations in order to calculate free energies.

In the studies in this dissertation, two methods were used: Thermodynamic Integration (TI) and Adaptive Biasing Force (ABF) calculations. In both cases, the reaction coordinate must be known or assumed. This reaction coordinate can be defined in terms of, say, the progress of a chemical reaction or the identity of atoms on a molecule. In our case, a suitable reaction coordinate was the distance between two aggregating molecules. Progress along the reaction coordinate is often denoted by $\lambda$, which will be adopted here. In both TI and ABF, the following relationship is used:

$$\frac{\partial F}{\partial \lambda} = \left\langle \frac{\partial H}{\partial \lambda} \right\rangle \tag{2.9}$$

where the term on the right is the ensemble average of the derivative of the Hamiltonian with respect to the order parameter, $\lambda$. By integrating this term, the free energy difference from one value of the reaction coordinate to another can be found. When $\lambda$ is the separation distance, the derivative is effectively a force on the system. However, calculating ensemble average derivatives with respect to position is complicated by the fact that some degrees of freedom are removed from the system depending on how the order parameter is defined (Equation 2.10, where $\lambda_i$ is a particular value of the order parameter) [88].

$$\left\langle \frac{\partial H}{\partial \lambda(\mathbf{r^N})} \right\rangle_{\lambda_i} = \frac{\int \frac{\partial H}{\partial \lambda(\mathbf{r})} exp\left(\frac{-E(\mathbf{r^N},\mathbf{p^N})}{k_B T}\right) \delta\left(\lambda(\mathbf{r^N}) - \lambda_i\right) d\mathbf{r^N} d\mathbf{p^N}}{Q} \tag{2.10}$$

When $\lambda$ is simply one of the Cartesian coordinates, this ensemble average can be calculated directly by MD through constraining the coordinates that define $\lambda$. However, if $\lambda$ is some non-linear combination of the Cartesian coordinates, like the radial separation distance between two objects in solution, the coordinate system in Equation 2.10 must be transformed into generalized coordinates where the order parameter coordinates are orthogonal to the rest. In this case, Equation 2.10 can be redefined as:

$$\left\langle \frac{\partial H}{\partial \lambda(\mathbf{r^N})} \right\rangle_{\lambda_i} = \left\langle \frac{\partial U}{\partial \lambda(\mathbf{r^N})} - k_B T \frac{\partial ln|J|}{\partial \lambda(\mathbf{r^N})} \right\rangle_{\lambda_i} \tag{2.11}$$

where $|J|$ is the determinate of the Jacobian for changing the coordinate system from Cartesian to the generalized coordinates [88]. While this term is simple to calculate, it will be neglected because it provides no additional information relevant to our study, and it makes the results more difficult to interpret. Instead, only derivatives of $U$ (the potential energy of the system) will be used. However, in this case, a true free energy is not calculated. Therefore, whenever the Jacobian is neglected, the integral of Equation 2.11 will be called the Potential of Mean Force, or PMF, highlighting that its integrals of forces, or derivatives with respect to the potential energy, in the system.

In TI, also known as the "blue moon ensemble" method, many simulations are set up with $\lambda$ held fixed at different values [89, 88]. Then, the various derivatives are numerically integrated across the reaction coordinate using such methods as the trapezoidal rule. The reason for its name is that this method permits sampling at $\lambda$ values that are typically not accessible using non-restrained MD; as in accessible "once in a blue moon." One difficulty with this method is that, if the PMF changes sharply with respect to the order parameter, the resolution of the different simulations may not be sharp enough to accurately calculate the PMF. In this work, TI was used to examine the PMF representative of the aggregation of GNRs. This method was used because it eliminates the need for the GNR to diffuse back and forth along the reaction coordinate, which would be very slow, and the PMF changes relatively slowly with respect to the reaction coordinate. In addition, this method has already been used many times in the literature to explore the aggregation of graphene sheets, although not for GNRs [53, 52, 80, 90].

In the ABF method, the forces are also integrated over many values of $\lambda$ [91, 88]. In this case, however, the system is permitted to diffuse in an unrestrained manner along the reaction coordinate. Bins at regular intervals are set up along the reaction coordinate where moving averages of the force are calculated for a particular value of the order parameter. The negative of this force is then applied to the system as a biasing force. This biasing force slowly levels both energetic barriers and wells allowing the system to diffuse freely back and forth across the reaction coordinate. When this occurs, an integration over the collected forces will provide a PMF. This method is used here to look at systems where $\lambda$ diffuses rapidly and the energy barriers and wells were both small in magnitude. In this case, the entities if note were the small oligomeric polyethylene glycol (PEG) and $n$-alkane chains adsorbing and desorbing from a graphene sheet.

## 2.2 Density Functional Theory

In Chapter 4, we will investigate the electronic properties of aggregated GNRs. In principle, this implies that we should solve the many-electron wave function:

$$H\Psi(\mathbf{r}_1, ..., \mathbf{r}_N) = E_i\Psi(\mathbf{r}_1, ..., \mathbf{r}_N) \tag{2.12}$$

with $H$ representing the Hamiltonian, $E_i$ an energy eigenvalue, $N$ the total number of electrons, and $\Psi$ being the many-body wave function. Unfortunately, this problem is intractable. Instead, various approximations are used. The most common method used in this work is Density Functional Theory, or DFT [65, 66]. In DFT, it is shown that the total energy of a system is a functional of the electronic density:

$$E[n(\mathbf{r})] = T[n(\mathbf{r})] + \int v(r)n(\mathbf{r})dr + \frac{1}{2}\int \frac{n(\mathbf{r})n(\mathbf{r}')}{|\mathbf{r} - \mathbf{r}'|}dr + E_{xc}[n(\mathbf{r})] \tag{2.13}$$

where $n(\mathbf{r})$ is the electron density, $E[n(\mathbf{r})]$ is the total energy, $T[n(\mathbf{r})]$ is the total electronic kinetic energy, $v(\mathbf{r})$ is the external electric potential (such as atomic nuclei), and $E_{xc}[n(\mathbf{r})]$ is the exchange-correlation functional. The second term on the right is the energetic component due to the interaction of the electronic density with an external electric field (atomic nuclei, for example), and the third is the interaction of the electronic density with itself. While the first three terms can be calculated exactly, there exist only approximate forms of $E_{xc}[n(\mathbf{r})]$, requiring estimations of this energy to be made. Typically, only the first few terms are used in the following series:

$$E_{xc}[n(\mathbf{r})] = \int \epsilon_{xc}(n(\mathbf{r})n(\mathbf{r})dr + \int \epsilon'_{xc}(n(\mathbf{r})\,|\nabla n(\mathbf{r})|^2\,dr + ... \tag{2.14}$$

In DFT, there is a unique electronic density function that minimizes $E[n(\mathbf{r})]$, and this $E[n(\mathbf{r})]$ is the ground state energy of the system. In practice, the ground state energy is found self-consistently by first estimating the electronic density from single electron wave functions, recalculating the single electron wave functions from a differential equation that is a function of the electronic density, and then repeating. The total energy is calculated by summing up all of the eigenvalue energies from the occupied electronic wave functions:

$$n(\mathbf{r}) = \sum_{i=1}^{N} |\psi(\mathbf{r})|^2 \tag{2.15}$$

$$H\psi_i(\mathbf{r}) = \left\{-\frac{1}{2}\nabla^2 + v(\mathbf{r}) + \int \frac{n(\mathbf{r}')}{|\mathbf{r}-\mathbf{r}'|}dr' + \frac{d\,(n(\mathbf{r})\epsilon_{xc}(n(\mathbf{r}))}{dn(\mathbf{r})}\right\}\psi_i(\mathbf{r}) = \epsilon_i\psi_i(\mathbf{r}) \tag{2.16}$$

$$E[n(\mathbf{r})] = \sum_{i=1}^{N} \epsilon_i \tag{2.17}$$

There are multiple functional forms that can be taken by the single electronic wave functions. In one software package used for this study, Gaussian 09 [81], Gaussian distributions centered on the atomic nuclei are used, resembling a linear combination of atomic orbitals. In Quantum Espresso (a DFT code used for modeling extended, periodic systems), plane waves are used instead [92].

There are typically two methods used for estimating $E_{xc}$ in a pure DFT framework. In the Local Density Approximation, LDA, only the first term in the expansion above is used [66]. A second, more advanced, approximation, known as the Generalized Gradient Approximation, GGA, uses the first two terms [93]. Additional terms of the expansion can be used, but hybrid methods are typically used first instead.

$E_{xc}$ can be split into its exchange and correlation components:

$$E_{xc}[n(\mathbf{r})] = E_x[n(\mathbf{r})] + E_c[n(\mathbf{r})] \tag{2.18}$$

While the correlation component must be approximated, the exchange term can be calculated using the Hartree-Fock method (HF). In this method, the many-body wave function is approximated by finding the Slater determinant of the single-electron wave functions of the system:

$$\Psi(\mathbf{r}_1, ..., \mathbf{r}_N) = \frac{1}{\sqrt{N}} \begin{bmatrix} \psi_1(\mathbf{r_1}) & \psi_2(\mathbf{r_1}) & \cdots & \psi_N(\mathbf{r_1}) \\ \psi_1(\mathbf{r_2}) & \psi_2(\mathbf{r_2}) & \ddots & \vdots \\ \vdots & \ddots & \ddots & \vdots \\ \psi_1(\mathbf{r_N}) & \cdots & \cdots & \psi_N(\mathbf{r_N}) \end{bmatrix} \tag{2.19}$$

This form permits the solving an effective single-electron Schr*ö*dinger's equation in a self-consistent approach, much like DFT. Also, the Slater determinate ensures that the many-body wave function is antisymmetric, which is a physical property of fermions such as electrons. Unlike DFT, correlation effects are completely neglected. However, the exchange term is more accurate. In popular and more recent hybrid DFT methods, the full DFT correlation energy is used, and a combination of the HF exchange and DFT exchange is used instead of the pure DFT exchange:

$$E_{xc}[n(\mathbf{r})] = aE_{x,HF}[n(\mathbf{r})] + (a-1)\,E_{x,DFT}[n(\mathbf{r})] + E_c[n(\mathbf{r})] \tag{2.20}$$

where $a$ is an empirically defined scaling term which lies in the range between 0 and 1. An example of this approach, used in the previous section, is B3LYP [82, 83, 84].

Hybrid methods can be used to reap the benefits of different methods, and creative use of the scaling term can be helpful to solve certain problems. One example of this is the Heyd-Scuseria-Ernzerhof functional (HSE) functional [94]. In extended, periodic systems, HF methods by themselves are difficult to use; the pure HF exchange interactions decay very slowly with respect to distance. This can greatly impede performance for many systems and might make calculations impossible for systems with very delocalized electrons (such as metals). The HSE functional overcomes this by separating the $1/r$ term found in the exchange functional into short-ranged and long-ranged components:

$$\frac{1}{r} = \left(\frac{erfc(\omega r)}{r}\right)_{short} + \left(\frac{erf(\omega r)}{r}\right)_{long} \tag{2.21}$$

where $\omega$ is an empirically defined term. By using these rescaled $1/r$ terms, the HSE functional becomes:

$$E_{xc}^{HSE}(\omega) = aE_{x,HF-short}(\omega) + (a-1)\,E_{x,PBE-short}(\omega) + E_{x,PBE-long}(\omega) + E_{c,PBE} \tag{2.22}$$

This permits the use of HF exchange only at short-range, where calculations can be done simply, whereas a DFT exchange is used at long-range.

Since DFT is able to calculate ground-state electronic densities, it has been used extensively to find low-energy molecular geometries. However, van der Waals interactions are due to correlation effects, which are not accurately captured by pure DFT. Therefore, geometries in which non-bonded interactions are important, including the systems of interest in this dissertation, are also unlikely to be accurate. One solution to this is to add empirical terms to the overall energy of the system to describe the van der Waals interactions [95]. This correction is called a dispersion correction, and it is described below:

$$E_{DFT-D} = E_{DFT} + E_{disp} \tag{2.23}$$

$$E_{disp} = -s \sum_{i=1}^{N_{at}-1} \sum_{j=i+1}^{N_{at}} \frac{C_{ij}}{R_{ij}^{6}} \frac{1}{1 + e^{-d(R_{ij}/R_r - 1)}} \tag{2.24}$$

where $E_{DFT-D}$ is the dispersion-corrected DFT energy, $s$ and $d$ are scaling factors, $R_{ij}$ is the distance between neighboring nuclei, $R_r$ is the sum of van der Waals radii between two atoms (determined from previously calculated electron densities), and $C_{ij}$ are dispersion terms estimated from previously calculated ionization potentials and static dipole polarizabilities. While corrections such as these do not modify the electronic properties of a system, they allow the approach to accurately represent non-bonded interaction energies and forces.

## 2.3 Single Particle Excitations: The $G_0W_0$ Method

There are at least two major drawbacks to using DFT: One is that the exchange-correlation functionals are imprecisely modeled approximations and the second is that it only models the ground-state electronic density [96]. Single-particle excitations (quasiparticle holes and electrons) as well as two-particle excitations (excitons) cannot be accurately modeled in this way. To represent these phenomena, Green's function approaches are typically followed [97].

Fundamentally, Green's functions describe the time-evolution of single particles in a time-dependent perturbing Hamiltonian

$$i\hbar \frac{d}{dt} |\phi(t) >= [H_0 + H_{int}(t)] \, |\phi(t) > \tag{2.25}$$

where $H_0$ is the ground state Hamiltonian and $H_{int}$ is the perturbing or interacting Hamiltonian. This is simply the time-dependent Shrhr*ö*dinger equation. For the systems of interest here, $H_{int}$ describes all electron-electron interactions. The Green's function, $G$, is defined as:

$$G(r_2, t_2; r_1, t_1) = -\frac{i}{\hbar} \frac{\left\langle \phi \left| T_t \left\{ \hat{\psi}_H(r_2, t_2) \hat{\psi}_H^{\dagger}(r_1, t_1) \right\} \right| \phi \right\rangle}{\langle \phi | \phi \rangle} \tag{2.26}$$

where $\phi$ is the ground state wave function, $T_t$ is a time-ordering operator, $\hat{\psi}_H$ is a particle annihilation operator, and $\hat{\psi}_H^{\dagger}$ is a particle creation operator [97]. The Green's function itself gives the probability of a particle at position and time 1 to be found at position and time 2 in the presence of an interacting field. Looking from right to left in the term on the right hand side of the equals sign, the equation describes the time evolution of a particle. First, the system starts out with the ground state $|\phi >$. Next, a particle is created at position 1 and time 1 and it evolves according to $H_{int}$ ($\hat{\psi}_H^{\dagger}(r_1, t_1)$). The system evolves until it is destroyed at $\hat{\psi}_H(r_2, t_2)$ and $H_{int}$ is turned off as system is returned to its ground state ($< \phi|$) The time-ordering operator ensures that these transformations occur in chronological order. This permits the expression of electrons if $t_2 > t_1$ and holes if $t_1 > t_2$ (the ordering of the creation and annihilation operators are switched). Due to the complexity of the following calculations, particular position and time coordinates can be switched to a single number.

$$G(r_2, t_2; r_1, t_1) = G(21) \tag{2.27}$$

The above equations are quite abstract, and it takes some effort to make them practically useful. With $H_{int}$ defined as the electron-electron interaction and by taking the time derivative of $G(12)$, the following relationship is found:

$$\left[ i\hbar \frac{\partial}{\partial t} - H_0(1) \right] G(12) = \delta_{1,2} - i\hbar \int V(1-3) G(1323) d3 \tag{2.28}$$

with $V(1-3$ being the Coulombic interaction between points 1 and 3. The $G(1323)$ term is a two-body Green's function that is difficult to work with, in practice, and can be factored back into one-body Green's Functions:

$$\left[i\hbar\frac{\partial}{\partial t} - H_0(1) + i\hbar\int V(1-2)G(22)d2\right]G(12) = \delta_{1,2} + \int \Sigma_{xc}(32)G(13)d3 \qquad (2.29)$$

where the new term on the left of the equals sign is simply the interaction with the ground state electron density. Everything on the left of the equals sign can be solved exactly using DFT and HF methods. The new term on the right, $\Sigma_{xc}$, is a self-interaction energy describing the exchange and correlation effects. An expansion for this was developed by Hedin in 1964 [98]. Hedin's equations are as follows:

$$\Sigma(1,2) = i\int\int G(1,3)W(1,4)\Lambda(3,2,4)d3d4 \qquad (2.30)$$

$$W(1,2) = v(1,2) + \int\int (v(1,3)P(3,4)W(4,2)d3d4 \qquad (2.31)$$

$$P(1,2) = -i\int\int G(1,3)\Lambda(3,4,2)G(4,1)d3d4 \qquad (2.32)$$

$$\Lambda(1,2,3) = \delta_{1,2}\delta_{2,3} + \int\int\int\int \frac{\partial\Sigma(1,2)}{\partial G(4,5}G(4,6)G(7,5)\Lambda(6,7,3)d4d5d6d7 \qquad (2.33)$$

where $W$ is a screened Coulombic interaction, $P$ is a polarizability operator, and $\Lambda$ is a vertex function. For simplicity, infinitesimal positive and negative values along the imaginary axis are neglected here and in the remainder of this chapter. The form of this expansion was developed in the same way as that for the development of the HSE functional, namely, to screen out the long-range HF interaction that makes convergence difficult for systems with delocalized electrons. Unlike HSE, which switches HF for a local functional with respect to distance, Hedin's equations dampens out the exchange energy at long distances with correlation effects. Also, by only including the Kronecker deltas in $\Lambda$, you are left with the GW approximation which must be solved self-consistently [67].

While the previous equations provide a framework for finding the Green's functions for electronic systems, nothing has yet been presented here to show how calculations are actually made and used. To that end, there are two more concepts that need to be described: First, if the system is in equilibrium (and $H_{int}$ is not a function of time), differences in time are the only thing that matters and the $G$ can be Fourier-transformed to the energy domain rather than the time domain [98]:

$$G(r_2, r_1; \epsilon) = \int G(r_2, r_1; \Delta t) exp\left[-\frac{i\epsilon\Delta t}{\hbar}\right] d\Delta t \tag{2.34}$$

Second, $G$ can be related to non-interacting Green's functions, $G_0$, through the Dyson equation [97]:

$$G(1,2) = G_0(1,2) + \int\int G_0(1,3)\Sigma_{xc}(3,4)G(4,2)d3d4 \tag{2.35}$$

$G_0$ is very convenient because it can be estimated with data from DFT simulations [67]:

$$G_0(r_1, r_2; \epsilon) = \sum_n \sum_k \frac{\phi_{nk}(r_1)\phi^*_{nk}(r_2)}{\epsilon - (\epsilon_{nk} - E_{xc,nk})} \tag{2.36}$$

with the subscripts $n$ and $k$ being the band number and k point, respectively, $\phi_{nk}$ a ground state eigenvector, $\epsilon_{nk}$ an energy eigenvalue from the ground state, and $E_{xc,nk}$ the corresponding exchange-correlation energy calculated by DFT. With this information, the Dyson Equation, and Hedin's equations, $G$ can now be found self-consistently. The resulting Green's function will have the form:

$$G(r_1, r_2; \epsilon) = \sum_n \sum_k \frac{\psi_{nk}(r_1)\psi^*_{nk}(r_2)}{\epsilon - \epsilon^{QP}_{nk}} \tag{2.37}$$

where $\psi_{nk}$ are updated eigenvectors, and (much more importantly) $\epsilon^{QP}_{nk}$ are the quasiparticle energies. These quasiparticle energies are the energies for holes and electrons in the system where $G$ was defined. These results can be used to create and update band structure with accurate energies that would be unobtainable using DFT.

With the inclusion of the vertex function, Hedin's equations are effectively an infinite expansion that cannot be solved. While the GW method can be used, in theory, to obtain quasiparticle energies by solving them self-consistently, this is usually too computationally expensive to be of value. Instead, the equations are, instead, used as a perturbation about the DFT results, which is called the $G_0W_0$ method in this dissertation and in common usage [99, 67].

$$P(1,2) = -iG_0(1,2)G_0(2,1) \tag{2.38}$$

$$W(1,2) = v(1,2) + \int\int v(1,3)P(3,4)W(4,2)d3d4 \tag{2.39}$$

$$\Sigma_{xc}(1,2) = iG_0(1,2)W(1,2) \tag{2.40}$$

$$G(1,2) = G_0(1,2) + \int\int G_0(1,3)\Sigma_{xc}(3,4)G(4,2)d3d4 \tag{2.41}$$

These equations are presented in the order that they will be solved. While many approximations were made, this method is significantly more accurate than using DFT methods [100], although it fails for highly correlated systems [99]. To perform these calculations, the ground state electronic structure was first estimated though DFT using the Quantum Espresso code [92]. Using those results, $G_0W_0$ calculations in this dissertation were performed using the Yambo software package [101]. While more accurate than DFT, they are also orders of magnitude more computationally intensive.

## 2.4 Two-Particle Excitations and the Bethe-Salpeter Equation

In the previous section, the $G_0W_0$ approximation was shown to be able to describe quasiparticle energies and electronic band gaps. However, in studying light adsorption and finding optical band gaps, two-particle excitations (or excitons) need to be explored. This can be achieved by using the Bethe-Salpeter

Equation (BSE), as discussed in this section. This method is a great deal more complicated than the $G_0W_0$ approach, but the steps required to solve it are very similar; hence only a few important points will be highlighted here.

Light adsorption is directly related to the magnitude of the imaginary part of the macroscopic dielectric function ($\epsilon_M$),

$$Im\left(\epsilon_M(\epsilon)\right) = Im\left(-\lim_{q\to 0}\left[v_{G=0}(q)P_{G=G'=0}(q,\epsilon)\right]\right) \tag{2.42}$$

where $P$ and $v$ are the polarizability operator and Coulombic interaction that has been Fourier- transformed from real space to reciprocal space [99]. While a polarizability operator was already calculated for the $G_0W_0$ method, the approximations are insufficient for BSE because it was derived from $G_0$ instead of $G$, and it completely neglects additional correlation effects incorporated by the vertex function [99]. Instead of using Hedin's equation for the polarizability operator, a two-body Green's function, $L$, is defined. This is the electron-hole correlation function, and it can be related to the polarizability operator:

$$L(1,1,2,2) = P(1,2) \tag{2.43}$$

$L$ is calculated by the Dyson equation:

$$L(1,2,3,4) = L_0(1,2,3,4) + \int\int\int\int L_0(1,6,3,5)K(5,7,6,8)L(8,2,7,4)d5d6d7d8 \tag{2.44}$$

where $K$ is the Bethe-Salpeter kernel [68]. Equation 2.44 is the Bethe-Salpeter equation, and it is used to model excitonic effects within an electronic system. $L_0$ can be calculated from results given in the previous section:

$$L_0(1,2,3,4) = G_{G_0W_0}(1,2)G_{G_0W_0}(3,4) \tag{2.45}$$

with $G_{G_0W_0}$ being the resultant Green's function from the $G_0W_0$ approximation [99]. Much like $G_0$ and $G$, shown before, $L_0$ and $L$ can be described by:

$$L_0(r_1, r_2, r_1', r_2'; \epsilon) = i \sum_c \sum_v \left[ \frac{\psi_c(r_1)\psi_v^*(r_1')\psi_v(r_2)\psi_c^*(r_2')}{\epsilon - \left(\epsilon_c^{QP} - \epsilon_v^{QP}\right)} - \frac{\psi_v(r_1)\psi_c^*(r_1')\psi_c(r_2)\psi_v^*(r_2')}{\epsilon + \left(\epsilon_c^{QP} - \epsilon_v^{QP}\right)} \right] \tag{2.46}$$

$$L(r_1, r_2, r_1', r_2'; \epsilon) = i \sum_S \left[ \frac{\chi_S(r_1, r_1')\chi_S^*(r_2', r_2)}{\epsilon - \Omega_S} - \frac{\chi_S(r_2, r_2')\chi_S^*(r_1', r_1)}{\epsilon - \Omega_S} \right] \tag{2.47}$$

with $\psi$ and $\epsilon^{QP}$ from the resulting $G$ values calculated by the $G_0W_0$ method [68]. The summations for $L_0$ are over valence and conduction states (symbolized by the subscripts $c$ and $v$). Likewise, $\chi$ and $\Omega_S$ are the resulting exciton wave functions and energies for $L$, and are summed over all possible excitations, $S$. Two important points to note here are that the minimum value for $\epsilon_c^{QP} - \epsilon_v^{QP}$ is the electronic band gap, and that $\Omega_S$ is related to this value.

The electron-hole interaction kernel, $K$, is approximated in a similar way as $G$ was estimated from the $GW$ method. It has the form:

$$K(1, 2, 3, 4) = K_x(3, 5, 4, 6) + K_d(3, 5, 4, 6) \tag{2.48}$$

$$K_x(3, 5, 4, 6) = -i\delta(1, 3)\delta(2, 4)v(1, 4) \tag{2.49}$$

$$K_d(3, 5, 4, 6) = i\delta(1, 4)\delta(3, 2)W(3, 4) \tag{2.50}$$

Here, $K_x$ and $K_d$ are called the exchange and direct terms, respectively [68]. The exchange term naturally describes the effects of electronic exchange in an exciton, while the direct term describes the Coulombic interaction between electron-hole pairs. These terms have a clear effect on $\Omega_S$. Assuming the spin-orbit effect is negligible, a spin-singlet exciton and spin-triplet exciton have energies of

$$\Omega_{S,singlet} = \left(\epsilon_c^{QP} - \epsilon_v^{QP}\right) + E_{K_d} + 2E_{K_x} \tag{2.51}$$

$$\Omega_{S,triplet} = \left(\epsilon_c^{QP} - \epsilon_v^{QP}\right) + E_{K_d} \tag{2.52}$$

with $E_{K_d}$ and $E_{K_x}$ being the energies contributions from the direct term and the exchange term, respectively [68]. While converting $L$ into a polarizability operator and then calculating the macroscopic dielectric constant, it is useful to look at a different derivation of $\epsilon_M$ to see the role of $\Sigma_S$ in an adsorption spectrum. In an electronic system, light can be modeled as a perturbing, time-dependent electromagnetic field on the system:

$$H_{light}(t) = -\frac{1}{c}A(r,t)\cdot v \tag{2.53}$$

with $c$ being the speed of light, $A$ being the electromagnetic vector potential, and $v$ being a velocity operator. Using Fermi's golden rule, the probability of transitioning from an initial to a final state ($P_{i\to f}$) becomes:

$$P_{i\to f} = 2\pi\frac{A_0^2}{c^2}\left|< f|v\cdot\lambda|i >\right|^2\delta(E_f - E_i - \epsilon) \tag{2.54}$$

with $A_0$ being the magnitude of the vector potential, $\lambda$ being a unit vector parallel with $A$, and $E_f$ and $E_i$ being the energies of the final and initial states, respectively [102]. This can then be used to estimate the imaginary part of $\epsilon_M$:

$$Im\left(\epsilon_M(\epsilon)\right) = \frac{4\pi^2}{\epsilon^2}\sum_f\left|< f|v\cdot\lambda|0 >\right|^2\delta(E_f - E_0 - \epsilon) \tag{2.55}$$

with the initial state now being the ground state and the system being summed over all possible final states [102]. In the case of excitons, this function has the form:

$$Im\left(\epsilon_M(\epsilon)\right) = \frac{4\pi^2}{\epsilon^2}\sum_S\left|< S|v\cdot\lambda|0 >\right|^2\delta(\Omega_S - \epsilon) \tag{2.56}$$

Assuming that the coefficients are non-zero, the minimum value of $\Omega_S$ corresponds to the optical band gap. In addition, this provides a simple tool to explain which transition will be more optically active than others [102].

# CHAPTER 3

# GNR SIDE-CHAIN DISPOSITION AND AGGREGATE MORPHOLOGIES

## 3.1 Introduction

As discussed in the introductory chapter, our first task involved screening many possible side-chains for their ability to disperse GNRs in solution. To do so, we considered a number of different grafting densities and solvents by calculating binding enthalpies and examining side-chain dispositions. This permitted us to observe general trends in tendency to aggregate with changes in side-chains and solvent, and hence provide a quick screening method to identify promising side-chains that lead to highly dispersed GNR concentrations.

In this chapter, enthalpies (or equivalently in this case, potential energies) of binding will be used as a metric, rather than free energies, since they are far less computationally expensive and permit a post-simulation deconstruction of the relative contributions from side-chains, GNRs, and solvent. This analysis affords us the opportunity to simulate and compare many different GNR side-chain configurations and side-chain/solvent systems. In the following chapter, a few selected configurations will be analyzed further with more costly free energy calculations.

Here, we will examine the behavior of GNRs with PEG and *n*-alkoxy side-chains of various lengths and grafting densities and their tendency to aggregate in water and NMP. These choices of side-chain were made because of their popularity with experimental groups wishing to reduce aggregational tendencies. This study will be split into two sections. First, we will describe the disposition of various side-chain configurations around the GNRs. Second, we will ascertain the nature of aggregate morphologies from Steered Molecular Dynamics (SMD) calculations and calculate their respective binding energies. This will provide information on the relative ability of the different side-chains to affect binding and link this to the side-chain dispositions from the first task. Both sections will begin by discussing simulations of GNRs in vacuum, as this scenario does not contain the complication of considering interactions with the solvent and helps to demonstrate key characteristics of the aggregates that form.

## 3.2 Simulation Set-Up

Periodic boundary conditions were used here, as is typical in MD. The GNRs spanned the length of the simulation cell, thus connecting across the periodic boundary and creating the appearance of an infinitely long ribbon. This allowed us to calculate per-length energy values without the need to consider the effects of the GNR tips (the ends of the ribbons); see Figure 3.1.A and 3.1.B. The box length was chosen to be 4.2 nm long in order to prevent individual chains from interacting with themselves while simultaneously minimizing artificial tension or compression forces enforced by the box dimensions. The length of the GNR was parallel to the y dimension of the box, which was held frozen, while the x and z dimensions were permitted to deform *via* the NPT barostat. In reality, GNRs dispersed in solution that are longer than their persistence length are expected to bend and coil [103, 104]. However, this would be very cumbersome to calculate, especially in solvent (as discussed in later sections), because these bent or coiled GNRs can be hundreds of nanometers long. Instead, placing GNRs across periodic boundaries, similar to the approach taken in modeling carbon nanotubes [105, 106], allows us to calculate per-length values that can be applied to the overall ribbon.

These energies are calculated using Equation 3.1:

$$\Delta E_{bind} = \frac{(E_2 + E_S) - 2(E_1)}{L} \tag{3.1}$$

where $\Delta E_{bind}$ is the binding energy, $E_2$ is the energy of a solvent box with two aggregated GNRs, $E_S$ is the energy of a solvent box with no GNRs, $E_1$ is the energy of a solvent box with one GNR, and $L$ is the length of the GNR. In each case, the number of solvent molecules in a solvent box was the same. These calculations were only carried out in solution.

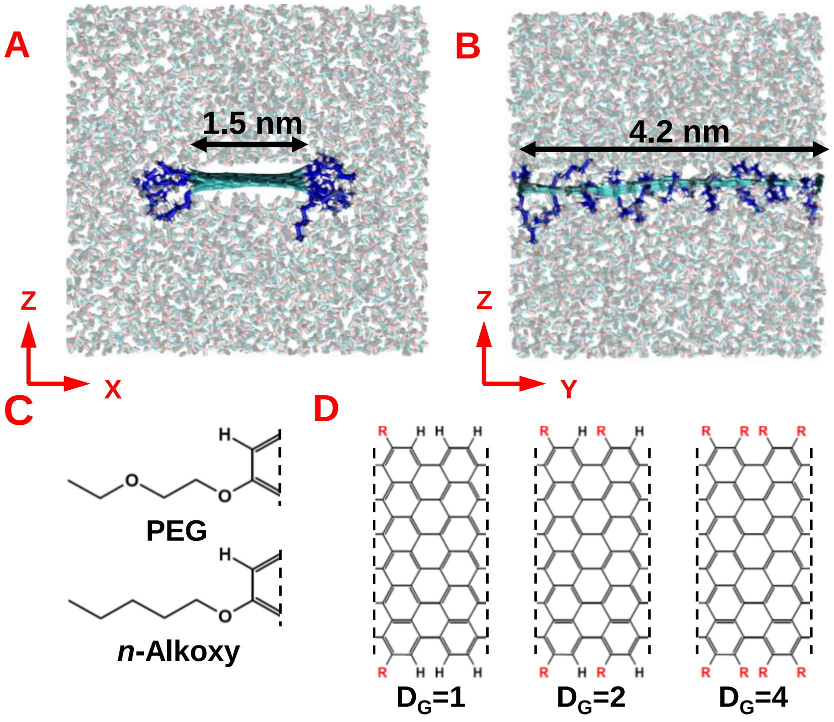

Figure 3.1: Several images representing the details of the simulation setup. (A) and (B) are cross-section and side views, respectively, of a typical simulation box. The GNR is shown in cyan with blue side-chains and surrounded by solvent molecules. (C) shows the two side-chain chemistries used here: PEG chains and *n*-alkoxy chains. (D) shows the three grafting densities used. Substitutional sites for the side-chains are shown in red. Most energies reported in this paper are given as per length quantities. For example, binding energies were calculated, defined as the energy change that occurs when two ribbons come into contact with each other.

## 3.3 MD Simulations of Single Ribbons

Our first study examined single GNRs with various side-chain configurations in vacuum, NMP, and water. This permitted us to understand the dispositions of the side-chains, which is an important aspect of aggregation behavior. There are three variables under consideration here: chain chemistry, chain length, and grafting density. Figure 3.1 shows the typical solvent box used in this study as well as descriptions of the chain-chemistries and grafting densities that were applied to the simulated GNRs. Two different chain chemistries were studied: *n*-alkoxy and PEG chains (shown in Figure 3.1.C). Unless otherwise mentioned, chain lengths containing 6, 12, and 18 chain atoms were used, with a chain atom being either a linked carbon or oxygen atom. Finally, the grafting density ($D_G$) represents how many chains are appended along the edge of a GNR for a given length. The three values of $D_G$ studied here are shown in Figure 3.1.D. $D_G = 1$ represents one ligand substitution for every four hydrogen termination sites, $D_G = 4$ represents total edge substitution with chain ligands, and $D_G = 2$ represents an intermediate amount of substitution. The width of the GNRs simulated in this paper is 1.5 nm. This width combined with the armchair configuration would give the hydrogen-terminated GNR a band-gap similar to silicon (1.0 eV) [107, 35], making it a reasonable GNR for device applications.

### 3.3.1 Single GNRs in Vacuum

In order to examine GNRs and side-chains without the complicating effects of solvent, we studied the behavior of GNRs in vacuum with the lowest grafting density, $D_G = 1$, different chain lengths and both chemistries (*n*-alkoxy and

PEG). A 1 ns simulation was sufficient to allow us to observe the conformational disposition of the side-chains in vacuum. Figure 3.2 shows representative images of both cross-sectional and top-down views of different GNRs. Both PEG chains and *n*-alkoxy chains performed similarly. The side-chains prefer to adsorb on either face of the GNR, but this requires the side-chains to be able to bend. Side-chains that are six atoms long (or less) are unable to bend enough to make significant contact with the GNR. Longer chains are able to wrap around the GNR. GNRs with side-chains nine atoms long were included to highlight this change. Chains that were wrapped around the GNR desorbed very infrequently.

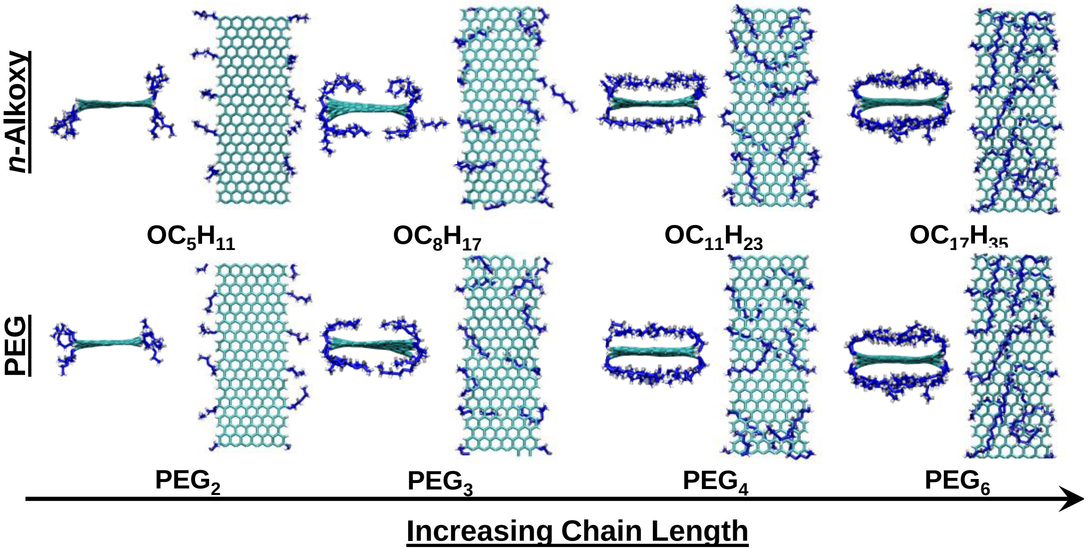

Figure 3.2: Cross-sectional (left) and top (right) views of GNRs with side-chain lengths varying from 6 to 18 atoms (bottom axis) for both *n*-alkoxy (top) and PEG (bottom) side-chains for $D_G = 1$.

### 3.3.2 Single GNRs in Solvent

Next, individual GNRs were simulated in both water and NMP solvents. These solvents were chosen because they are both used frequently for graphene and CNTs; but they are expected to interact very differently with the graphene material. NMP is known to be effective at dispersing large polyaromatic compounds, like graphene [13, 108], while water is very poor at dispersing graphene, requiring surfactants or charged functionalities [60, 56, 54]. With both solvents being polar, but the side-chains being either non-polar, for alkane-tipped *n*-alkoxy chains, or polar, PEG chains, it was expected that the *n*-alkoxy chains should interact less favorably in both solvents than the PEG chains. This means we have different levels of solvent quality for different combinations of side-chains and solvents. For example, using water and *n*-alkoxy chains would represent a poor solvent for both the GNRs and side-chains. This provides a greater diversity of outcomes than in the vacuum case.

All simulations were equilibrated for 2 ns and data were collected over an additional 12 ns. This length of time for data collection was sufficient to reduce sampling error to approximately 2.0 kcal/(molnm) based on the system energy's time correlation [109]. Unlike the vacuum case, there were many situations in solvent where the tips of the side-chains moved freely around the GNRs. Therefore, a rendering of single frames from the simulation (a snapshot in time) is not sufficient to describe the average locations of the side-chains during the simulation. Instead, we generated heat maps representing the relative probability of finding a chain atom at a particular point in space in the x and z dimensions. These heat maps are shown in Figures 3.3 and 3.4, which represent the behavior of the *n*-alkoxy and PEG chains, respectively. We only recorded the locations of carbon or oxygen chain atoms, excluding the oxygen atom directly bonded to the GNR, which shows little motion. Since the behaviors of the different chain lengths were comparable, results are only shown for one representative chain length, here 12-atom chains. The remaining heat maps are included in Appendix A.

As expected, GNRs with *n*-alkoxy chains in water show very similar behavior to those in vacuum calculations, as shown in Figure 3.3. Here, the chains are tightly adsorbed to the surface of the GNR in preference to extending into the poor solvent. However, their behavior is very different in NMP. In this case, most of the side-chains point away from the GNR.

The grafting density also affects the behavior of the side-chains. At $D_G$ = 1, the chains sample a large section of space around the edge of the GNR, and some side-chains periodically adsorb onto the GNR surface. At $D_G$ = 2, the side-chains are roughly parallel with the GNR faces. At $D_G$ = 4, because of steric congestion, the side-chains are oriented in many directions, including several adsorbed on the GNR. To understand the subtle change in disposition between $D_G$ = 1, $D_G$ = 2, and $D_G$ = 4, the component of potential energy for each simulation due to the $OC_{11}H_{23}$ and $PEG_4$ side-chains are shown in Figure 3.5. For ease of comparison, the $D_G$ = 1 results were set as the baseline value of 0 kcal/mol. In either case, the energy decreases from $D_G$ = 1 to $D_G$ = 2, showing that the side-chains adopt a more energetically favorable environment when they are close together, while the steric crowding that occurs at $D_G$ = 4 causes the energy to increase dramatically.

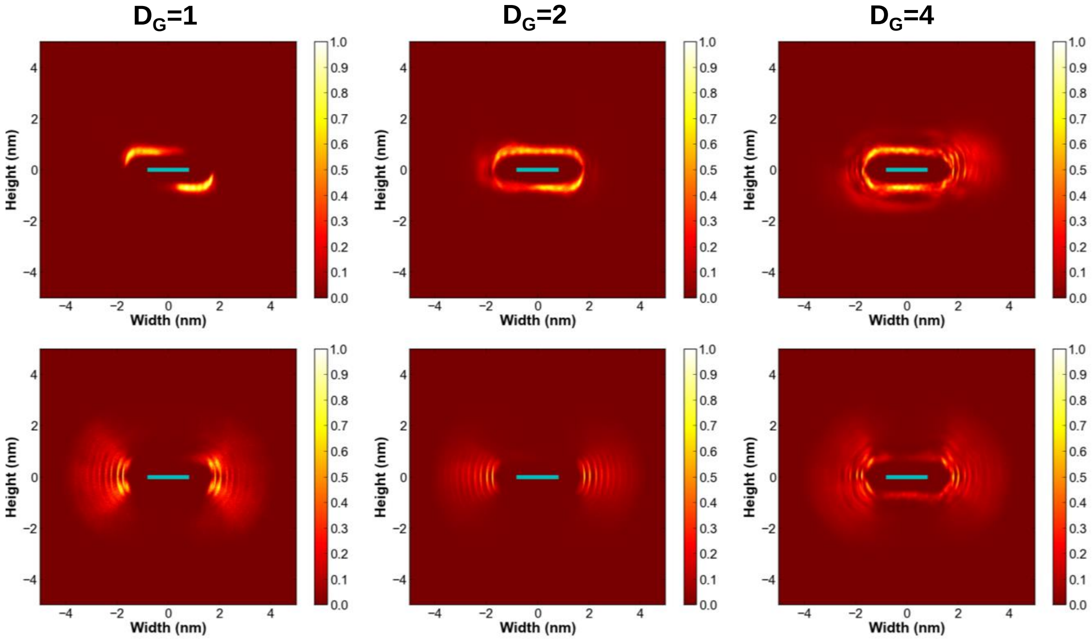

Figure 3.3: Heat maps of the cross-sections of $OC_{11}H_{23}$ (*n*-alkoxy) in water (top) and NMP (bottom) at all three grafting densities (increasing from $D_G$ = 1 on the left to $D_G$ = 4 on the right). The color represents the relative probability of finding a backbone atom at a point on the map, with white corresponding to the site most visited by a chain atom and dark red the least visited.

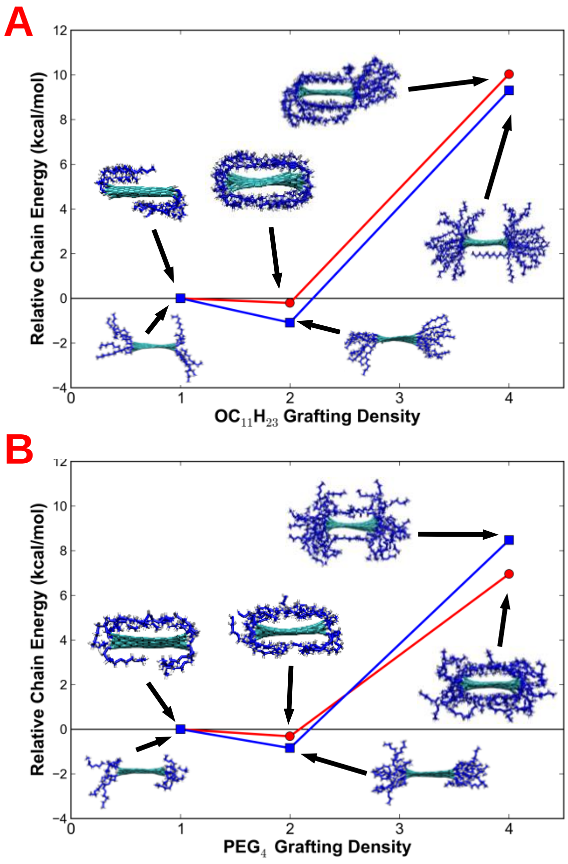

Figure 3.4: Relative chain potential energies for $OC_{11}H_{23}$ side-chains (A) and $PEG_4$ side-chains (B). Lines representing GNRs in water and NMP are shown in red and blue, respectively. All three grafting densities are represented relative to the energy of $D_G = 1$ which was set to zero. Snapshots from the simulation show the morphologies of the GNR and side-chains at key points.

While the PEG chains appended to GNRs in water appear to be similar to the vacuum case in Figure 3.4, details of the adsorption are somewhat different. Although PEG is known to be soluble in water, the chains were observed to adsorb onto the GNR. This behavior has been seen in other work [110]. Like the *n*-alkoxy case, the configuration resulting from $D_G = 4$ is slightly more expanded due to crowding. The distribution of the PEG chains is much more diffuse when NMP is the solvent. Here, the side-chains prefer to remain along the edges, with a few chains adsorbing onto the GNR. More chains are forced to be within close proximity to the GNR due to steric congestion, and are subsequently more likely to be adsorbed on either face of the GNR.

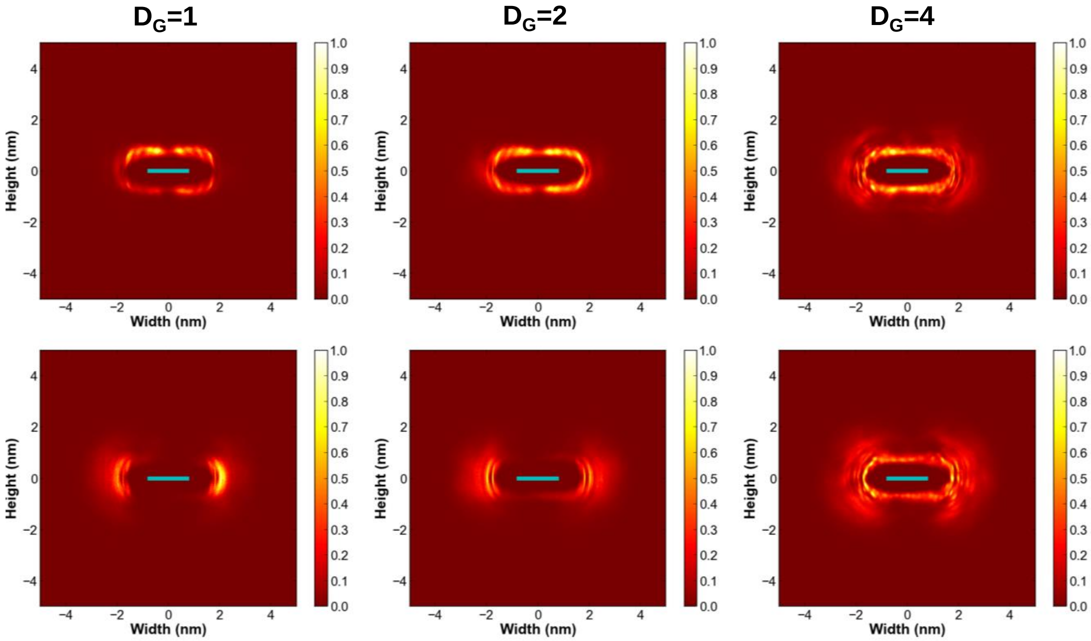

Figure 3.5: Heat maps of the cross-sections of $PEG_4$ in water (top) and NMP (bottom) for all three grafting densities (key as in Figure 3.3).

## 3.4 MD Simulations of Two-Ribbon Aggregates

Having observed how side-chains behave on single, isolated GNRs, we investigated how side-chains affected aggregate binding energies and aggregate morphologies. Again, results for vacuum calculations are shown first to describe the system without the presence of solvent. Next, we describe SMD calculations that were used to generate different aggregate morphologies of each GNR variant. We calculated binding energies of these different variants and determined the contributions of side-chains and GNRs to these binding energies. This provided a means to detect where changes in binding energy originated within the system: the GNRs or the side-chains.

### 3.4.1 MD Studies in Vacuum

In a previous section, we showed that side-chains in vacuum and in water tended to wrap around the GNRs. These side-chains can have a significant impact on the final aggregate morphology by preventing the GNRs from coming into direct contact with each other and hence mediate aggregation. Examples of aggregates with 0, 1, and 2 layers of side-chains separating the two GNRs are shown in Figure 3.6 in vacuum. The number of layers of side-chains that separate two GNRs in a given aggregate will be called its "layer number" in the rest of this chapter.

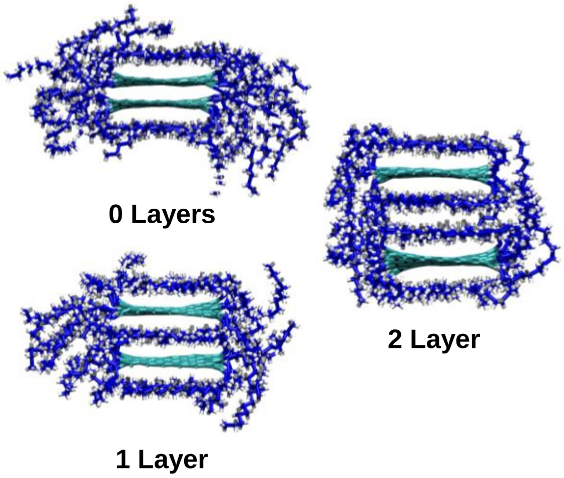

Figure 3.6: Cross-sectional views of aggregates formed by GNRs with $OC_{17}H_{35}$ side-chains for $D_G = 2$. The three images show example morphologies of aggregates with varying numbers of side-chains sandwiched between the ribbons.

Wrapped side-chains rarely desorbed from either face of the GNR. Side-chains between the GNRs are highly kinetically trapped because they are effectively adsorbed onto two GNRs, which constrict the side-chains between them. This meant that many simulations had to be run for each side-chain configuration in order to calculate the likelihood of layered structures forming. Such simulations were initialized by first simulating isolated single GNRs in vacuum for 20 ps, then quickly drawing them together by a retracting harmonic spring. The final aggregates were then allowed to equilibrate for 6 ns to permit the side-chains to relax. For each side-chain configuration, 0 to 20 side-chains were constrained to remain in-between the GNRs, while the rest were constrained to remain on the outside. These constraints were released after the GNRs aggregated. A diagram of this procedure is shown in Figure 3.7.

The results of these simulations are tallied in Table 1. The *n*-alkoxy and PEG chains behaved almost identically. In vacuum, their particular chemistry does not play a big role in their dynamics. However, the smallest chain lengths for the PEG-substituted GNRs can form layered structures, while the *n*-alkoxy substituted GNRs cannot. The PEG chains can more easily bend back towards the GNRs and allow more material to separate the two ribbons. Thus, with longer side-chains and higher grafting densities, layered structures are more likely to form. Longer side-chains can more easily fill the space between the GNRs, while side-chains at higher grafting densities have a greater chance of remaining between the GNRs due to the greater number of side-chains and the steric congestion along the edges.

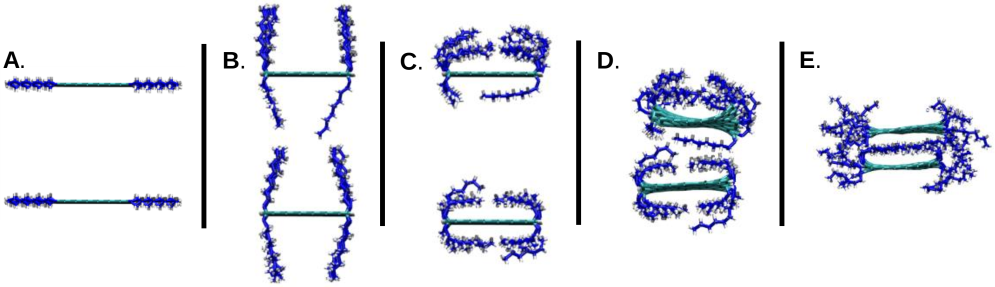

Figure 3.7: An outline for creating GNR aggregates in vacuum. (A) is the initial GNR placement with the faces being 26 Å away from each other. (B) shows the GNRs with the initial constraints forcing some side-chains between the GNRs. (C) shows the individual GNRs being permitted to relax for 10 ps at 50 K. (D) shows the GNRs being brought together in 5.5 ps. Finally, all constraints are released and the GNRs are heated to 300 K and permitted to relax over 6 ns in (E).

Table 3.1: Population of layered structures with different side-chain configurations. 21 simulations were ran in total for each side-chain configuration. Aggregate structures that did not clearly fit into one of the three categories were not included in the tally.

| $D_G$ | number of layered structures (0-layered #/1-layered #/2-layered #) | | | | | |
|---|---|---|---|---|---|---|
| | *n*-alkoxy chain length (chain-atom #) | | | PEG chain length (chain-atom #) | | |
| | 6 | 12 | 18 | 6 | 12 | 18 |
| 1 | (21/0/0) | (7/14/0) | (5/9/6) | (19/2/0) | (7/13/0) | (4/11/4) |
| 2 | (21/0/0) | (7/14/0) | (3/9/7) | (16/5/0) | (7/14/0) | (3/10/4) |
| 4 | (8/13/0) | (4/12/4) | (2/8/10) | (5/16/0) | (2/14/2) | (2/8/9) |

### Solution Studies *via* the Steered MD Method

In order to observe layered aggregates in solution, we used an Steered Molecular Dynamics (SMD) simulation approach. Single ribbons in solvent, discussed in the previous section, were replicated and placed 40 Å away from each other in a face-to-face orientation in the solvent. The two GNRs were then drawn together at a pulling rate of 2 Å/ns and were constrained to come together in a face-to-face manner so that multiple layered structures could be observed in a single run.

Different aggregated structures were found by locating local energy minima in the interactions of the two ribbons (including interactions of the GNRs and the side-chains) and correlated to visualizations of the aggregates that formed (Figure 3.8). The peaks between minima indicated distances where the side-chains were being forced out from between the GNRs. In some cases, due to sluggish kinetics, the chains between the GNRs were not pushed out by the SMD procedure by the end of the simulation. Therefore, a force was temporarily added to the separating chains to "evict" them from the surrounding GNRs before the energies were collected. In order to obtain aggregates in which the GNRs were in full contact, these remaining side-chains were removed by adding additional restraint forces. The binding energies of these zero-layered aggregates (without any intervening solvent layers) will be discussed first because they can be generated regardless of side-chain configuration and are thus more important. Then we will discuss "single-layered" structures (with one intervening layer of solvent).

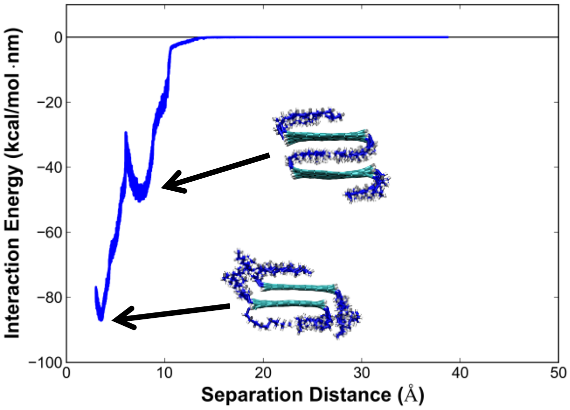

Figure 3.8: Ribbon-ribbon interactions in an SMD simulation. The two minima correspond to aggregates where the GNRs are either in contact with each other (at a separation of 3.6 Å) or where they are separated by a single layer of side-chains (at a separation of 7.5 Å).

### Binding Energies for zero-layered structures

Using Equation 3.1, we calculated the total binding energies for GNRs with the side-chains in direct contact with each other in NMP and water solvents; see Figures 3.9 and 3.10. These figures also show how the total energies can be broken down into components arising from the GNR and the side-chains. The more negative the energy value, the stronger the binding (and the greater the tendency for aggregation). The conformations of the side-chains corresponding to key points in these graphs are also presented. It is apparent that the side-chains can adopt a wide variety of morphologies and that they have a direct bearing on the binding energy.

We can draw a few conclusions about the binding energies by looking at these figures. For example, the binding energy for GNRs in NMP was generally less negative (less tendency for aggregation) than in water. This is expected since NMP is a much better dispersal medium than water for polyaromatic systems. Second, at $D_G$=1, the binding energy is very similar to the case without side-chains, regardless of chain length. For low grafting densities, $D_G$=1, only entropic or kinetic effects from these side-chains should affect aggregation.

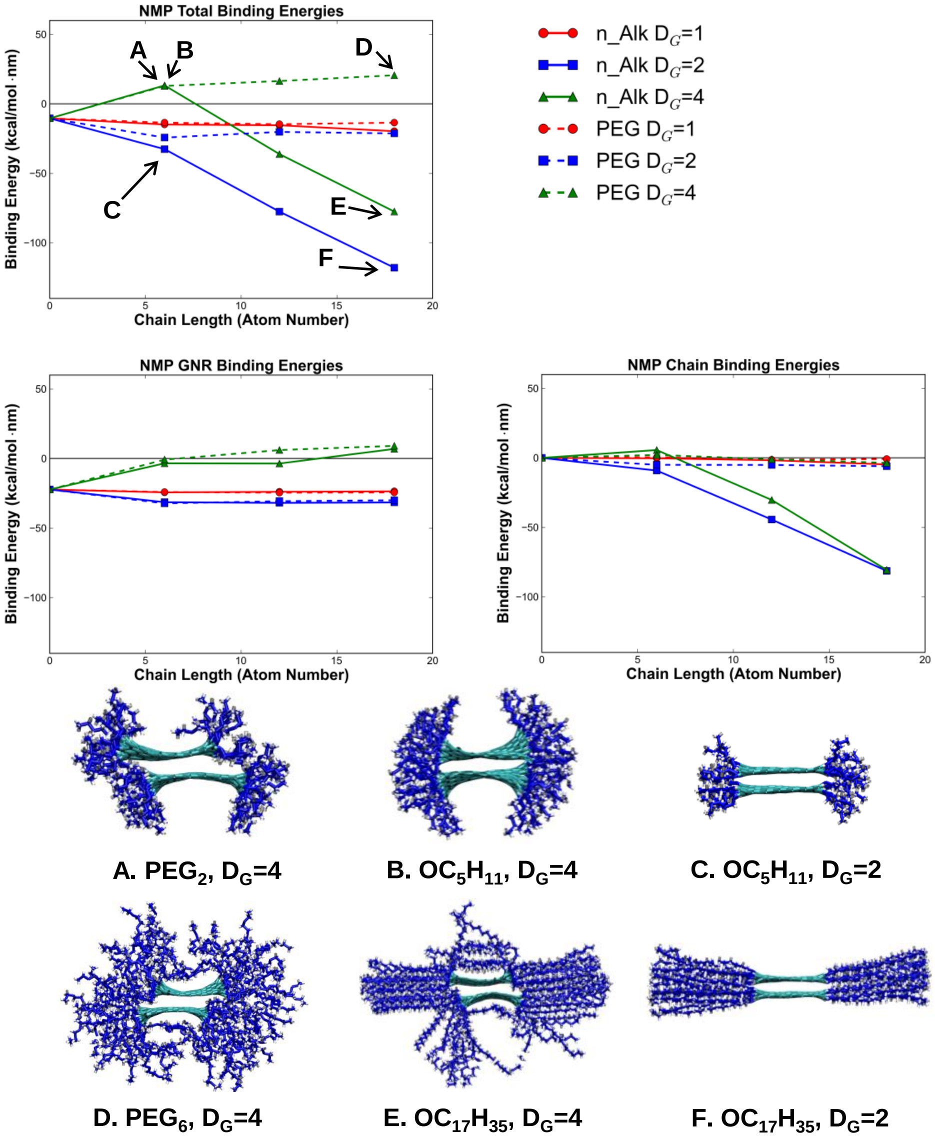

A. $PEG_2$, $D_G$=4 B. $OC_5H_{11}$, $D_G$=4 C. $OC_5H_{11}$, $D_G$=2

D. $PEG_6$, $D_G$=4 E. $OC_{17}H_{35}$, $D_G$=4 F. $OC_{17}H_{35}$, $D_G$=2

Figure 3.9: Potential energy per unit length for a variety of side-chain configurations as a function of chain length in an NMP solvent. Colored lines show the effect of different side-chain chemistries and grafting densities (solid lines for *n*-alkoxy and dashed lines for PEG, while the colors red, blue, and green represent $D_G$s of 1, 2, and 4, respectively). The total binding energies are shown in the top left figure; the contributions to this total energy from the GNRs and the side-chains are shown in the middle left and middle right plots, respectively. In addition, several points of interest are labeled in the total binding energy plot, and the respective morphologies of the aggregates are shown on the bottom.

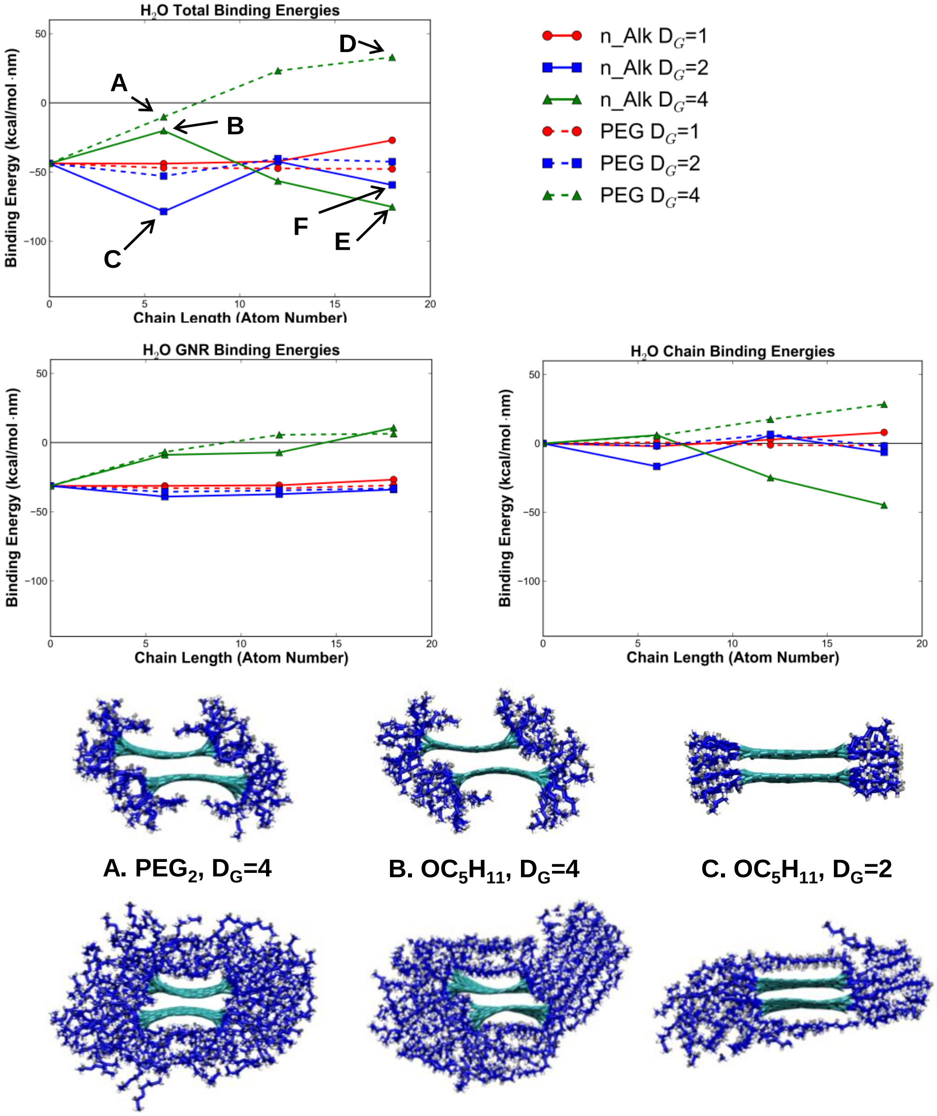

**A. PEG$_2$, D$_G$=4** **B. OC$_5$H$_{11}$, D$_G$=4** **C. OC$_5$H$_{11}$, D$_G$=2**

**D. PEG$_6$, D$_G$=4** **E. OC$_{17}$H$_{35}$, D$_G$=4** **F. OC$_{17}$H$_{35}$, D$_G$=2**

Figure 3.10: Potential energy per unit length for a variety of edge chain configurations as a function of chain length in a water solvent (key as in Figure 3.9). Analogously to Figure 3.9, this plot encapsulates the effect of all the variables studied in this paper for the behavior of GNRs in water.

In the case of NMP, shown in Figure 3.9, the most significant contributors to the overall trends are the relative solubilities of the *n*-alkoxy chains and PEG chains, as well as their tendency not to adsorb strongly onto the GNR. The binding energy component due to the PEG chains remains virtually unchanged with differing chain lengths and grafting densities. On the other hand, there is a linear, downward trend in binding energy (unfavorable for disaggregation) for GNRs with *n*-alkoxy chains at higher grafting densities, $D_G$ values of 2 or 4. Here, the increasing length of the side-chains creates an increase in the GNR/side-chain surface area upon aggregation. The GNRs were major contributors to these trends in the overall binding energy. For example, GNRs with $D_G$ = 4 are sterically crowded along the edges, forcing the shape of the ribbon to contort or shift with respect to the other GNR in order for the ribbons to come in direct contact. This greatly increases the contribution from the GNRs to the binding energy.

Despite the fact that the *n*-alkoxy side-chains increase the level of binding, the $D_G$ = 4 case with the $OC_5H_{11}$ side-chains actually has a positive binding energy (making aggregation unfavorable). The insolubility of the *n*-alkoxy chains as well as the tendency of side-chains to wrap around the GNRs makes the binding energies more difficult to interpret in water (Figure 3.10). In part, this is due to kinetic trapping of the side-chains wrapped around the GNRs, which causes a significant amount of noise in the data. Some of this is evident in Figures 3.10.E and 3.10.F, where, within the same aggregate, there are side-chains that are wrapped and disordered and others that are ordered much like the case of NMP in Figure 3.9. For the *n*-alkoxy case, chains with $D_G$ = 4 perform very similarly to those in the NMP solvent. However, this is not the case with $D_G$ = 2, where the binding energy minimum occurs at a length of six chain atoms.

Subsequently, as the length of the side-chain increases, the binding energy rises and then forms a plateau. This is due to the side-chains wrapping around the GNR before aggregating. At a chain length of 6 atoms, the chains cannot wrap around the GNR. Instead, they bind very strongly with the side-chains on the other ribbon. At longer chain lengths, the chains are initially wrapped around the GNRs. As a result, only some of the chains can interact favorably along the edges. This is the cause of the rise in energy and subsequent leveling out for the case when $D_G = 2$. At shorter chain lengths of six chain atoms, neither the wrapping nor the interactions of the side-chains play a significant role on the binding energy, and the grafting density plays the most important role in determining the binding energy.

### Binding Energies for single-layered structures

Aggregates separated by one layer of side-chains can be important in cases where kinetic trapping makes it difficult to achieve the zero-layered aggregate or when the binding energy of the single-layered aggregate is lower than the zero-layered case, making it more stable. We observed aggregates to form with multiple separated side-chains, as in the vacuum; but only single-layered structures could be consistently resolved with SMD.

The energies were calculated as in the previous section: equilibrating for 1 ns and collecting data for 12 ns. But, unlike the vacuum case, only one simulation was performed for each side-chain configuration. GNRs with long side-chains (12- to 18- atoms long) formed layered structures in water. However, in NMP, only $OC_{17}H_{35}$ side-chains with $D_G = 4$ produced a layered structure. Steric congestion along the edges, combined with the length of the side-chains, caused a significant number of side-chains to adsorb onto the GNR, making it possible for a layered structure to occur (Figure 3.3). Figure 3.11 gives the binding energy for each of the layered structures as well as binding energies of their non-layered counterparts. For *n*-alkoxy side-chains in water (Figure 3.11.A), the binding energies are either very similar to each other or the single-layered structure has a higher energy than the zero-layered structure.

The *n*-alkoxy case in NMP is very different; here, the layered aggregate has a lower energy than the zero-layered structure. The zero-layered structure is made up of two, highly bent GNRs, and the side-chains are very sterically congested, forcing them away from the well-ordered domains shown previously with *n*-alkoxy chains in NMP. The single-layer structure has a lower energy because this configuration allows the GNRs to be unbent and the side-chains can again form well-ordered domains. Renderings of these structures, and an energy component breakdown, can be found in Figure 3.12. Figure 3.11.B shows binding energies for the single-layer and single-layer aggregates for the PEG chains. Here, the side-layered structures have a much higher energy than the non-layered case for $D_G$ values under 4. On the other hand, the energy difference is smaller and reversed for the case where $D_G = 4$, with the layered case having a lower energy. The difference in energy profiles can be attributed again to the bending of the GNRs and steric congestion of the side-chains of non-layered structures at high grafting densities. Further details and renderings of these structures can be found in Figure 3.13.

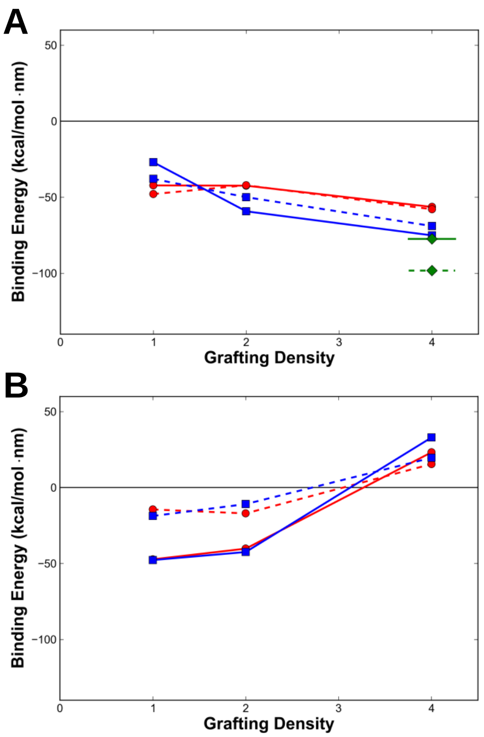

Figure 3.11: Comparison of binding energies between GNRs with, and without, intervening layers of side-chains in good and poor solvents. (A) shows results for *n*-alkoxy chains; (B) shows results for PEG chains. Binding energies of GNRs with side-chains that are 12 atoms long in $H_2O$ are shown in red, those with side-chains that are 18 atoms long in $H_2O$ are shown in blue, and those with side-chains that are 18 atoms long in NMP are shown in green. Single-layered and zero-layered structures are represented by dashed and continuous lines, respectively.

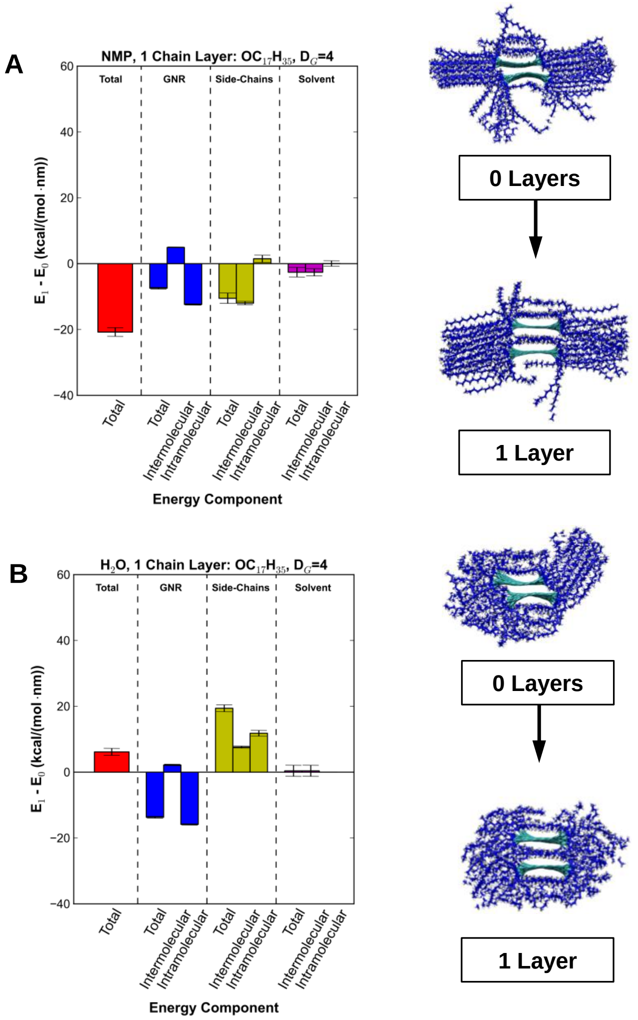

Figure 3.12: Decomposition of the various components that lead to the total energy of $OC_{17}H_{35}$ at $D_G = 4$ in NMP (A) and water (B).

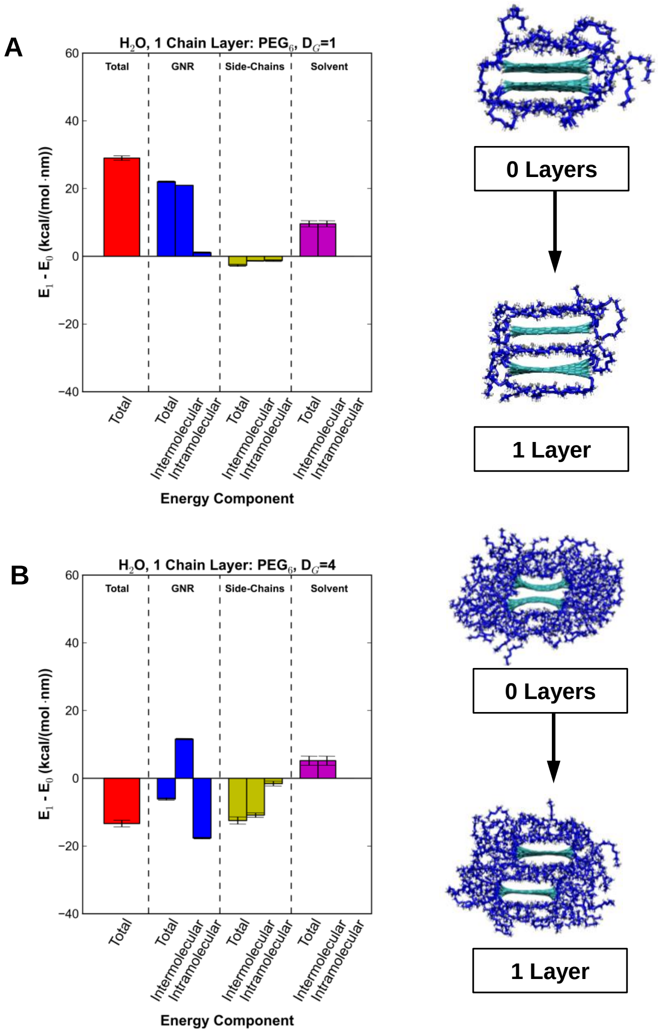

Figure 3.13: Decomposition of the various components that lead to the total energy of $PEG_6$ in water with $D_G = 1$ (A) and $D_G = 4$ (B).

### 3.4.2 Discussion

We found that there were many nuanced ways in which side-chain conformations are affected by their intrinsic characteristics of length, chemistry and density and their interaction with their environment, especially the choice of solvent. We observed a rich variety of side-chain conformations (Figures 3.3 and 3.4 make this apparent) and were able to relate them back to their effect on the binding energy of the nanoribbons. While this complexity of ribbon, side-chain, solvent interactions makes generalizations difficult, we were able to determine which side-chain characteristics are more effective than others at decreasing the binding energy of 2D ribbons like GNRs.

With the "light and shade" that this has provided for side-chain selection, we can apply it to screen quickly for side-chain choices that can be synthesized in a lab. This is explained in more detail in the discussion below. Although these enthalpic calculations clearly say nothing about the entropic effects, we believe that they have a key role to play as a "triage," first step, to identify more promising side-chain choices. More promising choices can then be subjected to greater scrutiny by detailed and expensive free energy calculations that will account for entropic effects, and ultimately tested experimentally.

Overall, we summarize our observations as follows, answering a series of relevant questions:

*What is the importance of each of the variables studied here?* Our results show that the overall net effect of all the variables studied on the binding energy is a delicate balance of multiple factors, making the outcome too difficult to have predicted *a priori*, but uncovered by the comprehensive study here. These results will allow future studies to focus first on more important variables, especially grafting density. For example, with side-chains in a good solvent (PEG chains in water or NMP), the binding energies are only slightly affected by chain-length. However, for side-chains in a poor solvent (*n*-alkoxy chains), the binding energies increase (favoring disaggregation). This latter behavior is only seen if $D_G > 1$, and longer chain lengths increase this characteristic. Layered aggregates are more likely to form with longer chains and higher grafting density.

*What is the effect of the grafting density?* Despite the intricate relationship between the tested variables to affect the binding energy of the system, the grafting density had the single most significant impact on the binding energy. This was first apparent for single ribbons; Figure 3.4 showed the strong influence of grafting density on side-chain interactions. The heat maps in Figures 3.3 and 3.4 showed that steric congestion along the edges forces side-chains into more spread-out conformations. But more importantly, the summative plots in Figures 3.9 and 3.10 show that it is only the highest grafting density with a suitable chemistry (PEG chains) that leads to the positive binding energy that encourages dispersibility. This is a large enough effect that it can even overcome the presence of a poor solvent. The steric crowding at such densities made it necessary for the GNRs to deform significantly if aggregated, making binding significantly less favorable. GNRs with highly branched side-chains, which have been shown experimentally to be dispersible, could behave analogously to these GNRs with high grafting density [46].

*How does the ability of side-chains to wrap around the GNRs impact aggregation?* In vacuum and poor solvents (like water), side-chains prefer to wrap around the GNRs. In some cases, this leads to aggregates where the side-chains formed multiple layers between the GNRs. However, these aggregates invariably possessed a higher energy than systems without intervening side-chain layers in either solvent, indicating they were only metastable states (see Figure 3.11). There are, however, cases in which side-chain wrapping can be helpful. An interesting case in point occurred only for shorter PEG chains in a water solvent at low to intermediate densities, *i.e.*, $D_G < 4$. Here, the layered structures had a much higher (more positive) binding energy than the non-layered case. This indicates that, in this particular case, the PEG chains behaved as a protective layer around the GNRs, preventing them from strongly binding together.

However, using this general strategy to alleviate aggregation is problematic for several reasons. First, the binding energy of the layered structure is still significantly low, indicating that the binding is still strong. Second, the aggregate with the PEG side-chain layer is metastable. If the barrier between the layered and non-layered cases is small, the existence of this metastable structure should have little impact on aggregation. If the barrier is large, the zero-layer aggregate might not be easily obtainable and the single-layer case would make a large impact on the nature of aggregation. Metastable protective layers have been cited in the literature for dispersing graphene. For example, Shih *et al.* indicated that some of the most successful solvents at dispersing graphene form metastable solvent layers that slow down the rate of aggregation [52]. While further investigation of these layered structures is outside the scope of this study, it would be interesting to study them further to see what effects they have on aggregation despite their failure in reducing the binding strength sufficiently to prevent aggregation in this study.

In this study, it appears that GNRs with PEG chains in NMP with $D_G = 4$ are the most viable for preventing aggregation. The PEG chains interact favorably with the solvent and do not form highly ordered low-energy domains along the sides. The NMP solvent interacts more favorably with the GNRs than water, making the strength of binding less strong. In addition, the high grafting density forces the GNRs to contort greatly when they come into contact with each other, again greatly decreasing the binding energy.

## CHAPTER 4

## FREE ENERGIES OF GNR AGGREGATION

### 4.1 Introduction

As discussed in the first chapter, pristine graphene in solvent is typically dispersed, rather than soluble. After dispersion, it typically aggregates over a period of hours, days, or months. Dispersing graphene in a variety of solvents has been studied quantitatively. For example, Hernandez and co-workers found Hansen solubility parameters for graphene by comparing the maximum dispersibility of sonicated graphene in many different solvents [51]. While this and similar studies were helpful for finding effective solvents for dispersing graphene, it does not explain why different solvents perform better than others. In order to understand the mechanism of aggregation, molecular simulations are a highly suitable tool.

Shih *et al.* were the first to investigate why certain solvents performed better than others using MD [52]. In their study, they calculated the PMF with respect to separation distance of two *rigid* graphene sheets approaching each other in a face-to-face manner. They showed that solvents such as NMP interact more favorably with graphene sheets than it does with itself. As the two graphene sheets approach each other, a single layer of solvent molecules form between the two graphene sheets. Since the solvent interacts more strongly with the two graphene sheets than itself, this state is metastable, and there is a significant free energy barrier to breaking it. Once broken, the graphene sheets come together in a highly energetically favorable aggregated state. Using the MD results in combination with a macroscopic kinetic theory of aggregation, they were able to accurately represent the evolution of a dispersion over the course of 150 days. Their use of the Thermodynamic Integration (TI) method to calculate the PMF between two parallel graphene sheets has been adopted by other researchers to look at the dispersive properties of other solvents [80, 90, 53].

In the kinetic theory used by Shih *et al.*, the total flux for the graphene moving through a solvent, $J_{Total}$, is the summation of the flux due to diffusion, $J_{Diff}$, and the flux drift $J_{Drift}$ flux due to the PMF between neighboring graphene sheets:

$$J_{Total} = J_{Diff} + J_{Drift} \tag{4.1}$$

$$J_{Total} = -D\frac{dC}{dr} - DC\frac{d\,(V/k_BT)}{dr} \tag{4.2}$$

where $D$ is the diffusivity of graphene, $C$ is the concentration of graphene, and $V$ is the PMF between the sheets of graphene. From here, the rate of aggregation, $k$, can be estimated (Equation 4.3, where $r_0$ is the distance between the two sheets at aggregation).

$$k = \frac{8\pi D}{\int_{r_0}^{\infty} \frac{exp(V/k_BT)}{r^2} dr} \tag{4.3}$$

Functionalized GNRs are a bit more complicated to model. Graphene is a homogenous 2D material. While there are many paths that two sheets can take towards aggregation, they will almost always involve two patches on either sheet making the first contact with each other. The kinetic model from Shih *et al.* took advantage of this in its derivation. First, Equation 4.3 was derived assuming the objects aggregating were spheres of some surface area. Second, $V$ was calculated in a per-area basis:

$$V = \Phi A \tag{4.4}$$

with MD being used to calculate $\Phi$ and $A$ being a fitting term that is determined from experiment. Functionalized GNRs have side-chains that might make the

PMF qualitatively different depending on how the GNRs come together. Therefore, a kinetic model derived from face-to-face aggregation may not be appropriate for GNRs. In addition, the dynamics of the side-chains are sluggish as compared to the solvent – it takes much more time to equilibrate the side-chains – making the calculations for the PMF much more expensive.

While estimating the rate of aggregation for functional GNRs is impossible without knowledge of the most common reaction path to aggregation, multiple trajectories can still be followed using TI rather than the face-to-face mechanism studied by Shih *et al.* In graphene systems, Fu *et al.* suggested examining the path in which graphene sheets slide past each other as an alternate path towards dispersion (and, alternatively, aggregation) [53]. The rationale behind this choice was that, while the true interaction pathway was unknown, it probably fell between one of two extremes: (1) where the graphene sheets slide past each other and (2) where they come together in a face-to-face trajectory. While data from simulations such as these may not be useful in a kinetic model like the one described above, it would provide a tool to rank different solvent/side-chain systems in terms of dispersibility by comparing the largest peaks along the different trajectories between the different systems.

In this study, we will examine the effects of different edge terminations (hydrogen, *n*-alkoxy chains, and PEG chains) on aggregation in NMP to build upon the results from the previous Chapter. First, the adsorption of lone *n*-alkane and PEG chains with a flexible graphene sheet will be simulated to build intuition regarding how they might interact with flexible graphene sheets. Next, we will describe the set-up of the TI runs in detail. We will discuss the results of TI runs in both face-to-face and sliding trajectories and rank the effectiveness of the different edge configurations. Finally, Steered Molecular Dynamics (SMD) simulations will be undertaken to show how the various free energy barriers caused by separating or coalescing the GNRs might affect aggregation. The goal of this study is not only to understand the aggregation of GNRs with different edge functionalizations, but also suggest a tool to use to predict the effectiveness of different side-chains before synthesizing them. This would be an effective time- and resource- saving strategy, if successful.

## 4.2 Results

### 4.2.1 Adsorption of *N*-Alkane and PEG Chains on Graphene

Before calculating the PMFs of aggregating GNRs, we calculated the free energy of adsorption for PEG and *n*-alkane chains on a rigid graphene sheet. We set up the simulation as shown in Figure 4.1. A single, periodic graphene sheet sat parallel to the xy plane and was located at z = 0 Å. A single PEG, or *n*-alkane, chain that was disconnected from the GNR sat above the graphene sheet. Both the PEG and *n*-alkane chain involve a chain that is 17 non-hydrogen atoms long, in total. In order to calculate the free energy of adsorption, we used the ABF algorithm with bins separated by 0.05 Å. Here, the order parameter was z, therefore:

$$\Delta F = \int \left\langle \frac{\partial H}{\partial z} \right\rangle dz \tag{4.5}$$

where this equation is identical to Equation 2.9 except the order parameter, $\lambda$, is z, the separation distance between the graphene sheet and the center of mass of the chain.

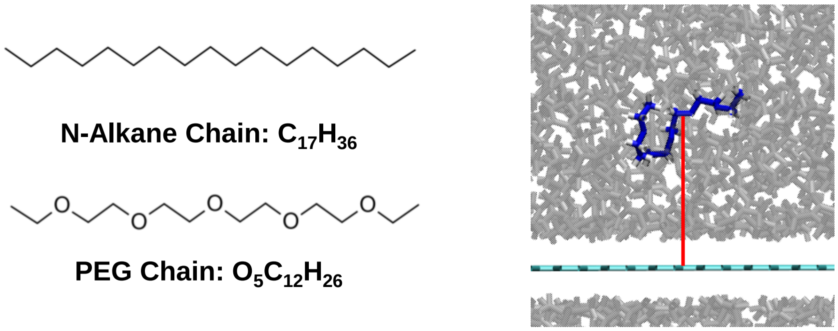

Figure 4.1: The chain types used in the ABF calculation are shown on the left. A representative image of the simulation (right) shows the GNR in cyan and the disconnected dark blue atoms representing the chain. The light grey atoms make up the solvent. The red line represents the distance between the centers of mass of the GNR and the chain.

As described in Chapter 2, ABF calculates free energies by integrating ensemble averages of the Hamiltonian derivatives across an order parameter, $z$. However, unlike TI, the system is not restrained to any one point along the reaction coordinate and is permitted to diffuse freely back and forth once the biasing force converged. To sample the system well enough for the biasing force to converge, the system must diffuse many times over all permitted values of the order parameter (which is between $z = 3$ Å and $z = 15$ Å). In order to speed convergence, we set up nine simulations with smaller, overlapping ranges of the order parameter (Table 4.1). From each of the simulations, we collected the relevant forces. Combined gradients were calculated from overlapping simulations by performing a weighted average between the two runs based on the number of times the simulation reached a particular point in space. Finally, the combined gradients were reintegrated using the trapezoidal method to produce the graphs shown in Figure 4.2.

Table 4.1: Order parameter ranges for the ABF calculations run

| Simulation Number | $z_{min}$ (Å) | $z_{max}$ (Å) |
|---|---|---|
| 1 | 3.0 | 6.0 |
| 2 | 6.0 | 9.0 |
| 3 | 9.0 | 12.0 |
| 4 | 12.0 | 15.0 |
| 5 | 3.0 | 4.5 |
| 6 | 4.5 | 7.5 |
| 7 | 7.5 | 10.5 |
| 8 | 10.5 | 13.5 |
| 9 | 13.5 | 15.0 |

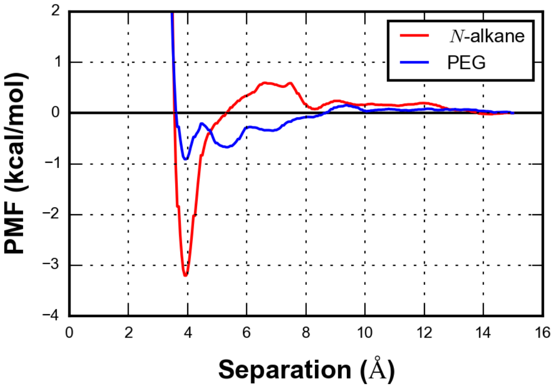

Figure 4.2: PMFs calculated for both the *n*-alkane chain (shown in red) and the PEG chain (shown in blue) above the graphene sheet.

In both cases, the chains are fully adsorbed on the sheet at 3.9 Å. However, the adsorption free energy is very different in the two cases. The $\Delta F$ of adsorption is -3.2 kcal/mol and -0.9 kcal/mol for the *n*-alkane chain and PEG chain, respectively. The tendency for the *n*-alkane to adsorb more strongly than the PEG in NMP is not surprising given the stronger binding energies of many of the GNRs with *n*-alkoxy side chains over GNRs with PEG chains of similar lengths and grafting densities. From these results, it is expected that the adsorption of the *n*-alkoxy side chains on the GNRs should play a more significant role in the aggregation process than those with PEG chains.

### 4.2.2 TI Simulation Set-Up

The three GNRs under investigation in this study are presented in Figure 4.3. The PEG- and *n*-alkoxy- terminated GNRs correspond to the $PEG_6$- and $OC_{17}H_{35}$- terminated GNRs with a $D_G$ of 1 in Chapter 3. All three of these systems had similar binding enthalpies, so this study emphasizes the additional information that free energy calculations can provide. In addition, the PEG-terminated GNR is very similar to one used in experimental work [1], providing a direct connection to GNRs that have already been synthesized. Unlike in Chapter 3, the GNRs are finite. This was done to allow the GNRs to rotate freely when necessary as well as to accelerate the equilibration of the solvent leaving and entering the space between the GNRs.

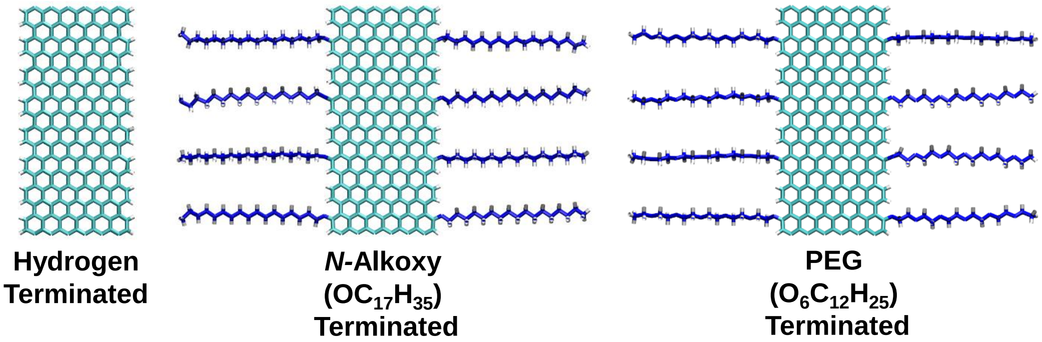

Figure 4.3: Images of the three GNR terminations used in this study. The graphene carbon atoms are shown in cyan, the hydrogen atoms in white, and carbon and oxygen atoms in the side-chains are shown in dark blue.

Following the procedure for TI calculations that was described in Chapter 2, we set up many simulations where the system is constrained to a certain value of the order parameter. In this instance, the order parameter is the separation distance between the GNRs. A benefit to using this method is that the system can be sampled very well for values of the order parameter that the system is unlikely to explore very often if it were left unconstrained. However, problems still arise with implementing it for the GNR system. Ideally, the only parameter that should be constrained in each simulation is the distance between the center of masses of the two GNRs. Unfortunately, the solvent, side-chains, and especially the GNRs explore parameter space very slowly, so it would take an infeasibly long time to fully sample all relative orientations of the GNRs, positions of the side-chains, and locations of the solvent molecules. In addition to this kinetic limitation, there are also thermodynamic limitations: There are multiple paths that GNRs can take to aggregate (*e.g.*, the face-to-face *vs.* sliding examples discussed in the introduction). Each reaction path intersects with all values of the order parameter between the reactants and products. However, a simulation set up to sample the system at a particular order parameter may not be able to sample all of the paths because of large energy barriers between them. When a set of simulations are set up for TI, each of them representing a different value of the order parameter, there is no guarantee that they will all find themselves on the same path. The resulting calculated PMF could contain elements from different reaction paths inconsistently, ultimately rendering the PMF inaccurate and useless. A diagram of this problem is presented in Figure 4.4.

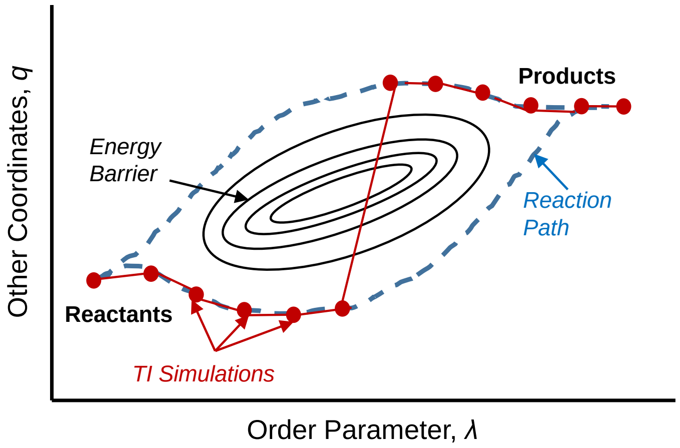

Figure 4.4: A diagram representing a system with multiple reaction paths that are separated by an energetic barrier. Each red dot represents a single TI simulation. If these simulations are set-up independently from each other, they might sample from different reaction paths. This will result in an inaccurately calculated PMF.

In order to circumvent these problems, two strategies were used. First, the degrees of freedom of the two GNRs were severely limited. Since the GNRs are the largest and most massive objects in the simulations, their sluggish kinetics will cause significant sampling problems in the simulations. In addition, the large energies involved with them approaching each other, and their highly asymmetric structure, makes it likely that the system will contain multiple paths to aggregation, with large free energy barriers separating them. Restricting the number of degrees of freedom of the GNRs resolves many of these problems. One constraint is the movement of individual carbon atoms within the GNR. With the exception of the atoms in the side-chains, the hydrogen atoms, the carbon atoms bonded to those hydrogen atoms, and their nearest neighbors, the GNR atoms were held fixed and the GNRs themselves behaved as rigid objects. In addition, the GNRs were not permitted to rotate with respect to each other. This constraint necessitates artificially choosing the path to aggregation (face-to-face and sliding, as pictured in Figure 4.6).

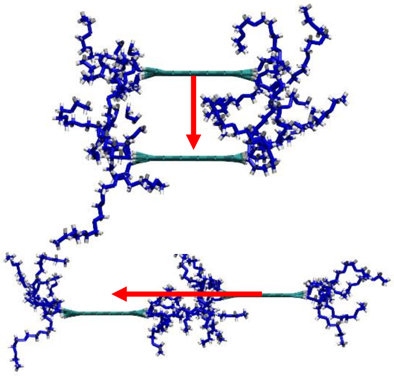

Figure 4.5: Images of GNR cross-sections undergoing face-to-face (top) and sliding (bottom) paths. Following the definition for x, y, and z in the text, the face-to-face path follows along the z direction and the sliding path follows along the *x* direction.

Since there were many constraints on the system, and because it was important that one TI simulation in each set had the GNRs in a fully aggregated state, the relative position of the aggregated GNRs had to be defined in terms of $x$ (along the width of the GNR), $y$ (along the length of the GNR) and $z$ (perpendicular to the face of the GNR) coordinates. This was done by first initializing a simulation box with two aggregated, hydrogen-terminated GNRs for 1.2 ns. One of the GNRs was held fixed in the center of the box, and the other was free to move as a rigid body, as described above. After the initialization was complete, the relative positioning of the centers of mass between the two GNRs was collected during a 10 ns run. Histograms were generated representing the relative frequency of finding the GNRs separated by different values of $x$, $y$, and $z$ coordinates (Figure 4.6). The peaks of the histogram correspond to positions where the fully aggregated state is located. For these hydrogen-terminated GNRs (as well as the *n*-alkoxy-terminated and PEG-terminated GNRs) was found to be $x = 1.3$Å, $y = 0.7$Å, and $z = 3.4$Å (Figure 4.7).

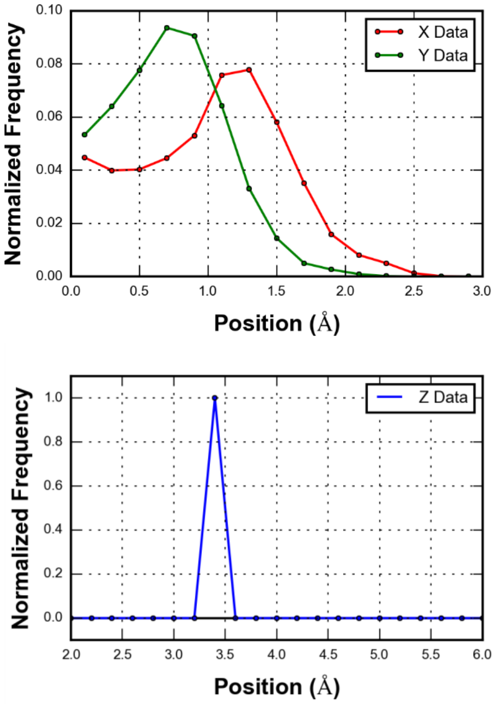

Figure 4.6: Histograms of the relative $x$ and $y$ positions (top) and $z$ positions (bottom). The center of each of the bins is represented by dark circles in the graphs.

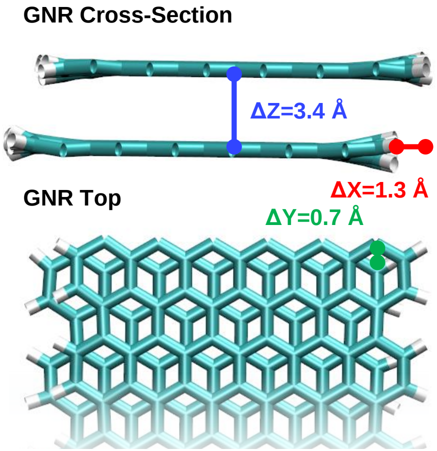

Figure 4.7: Relative positioning of the GNRs in the fully aggregated state.

While constraining the GNR atoms is likely to solve the majority of the sampling problems discussed above, the solvent molecules and the side-chains might still sample parameter space too slowly and follow inconsistent paths to aggregation. We solved this problem by running two separate sets of TI simulations for each GNR type and aggregation path. The first set involved initializing a simulation box in which the GNRs adopted an aggregated state for 400 ps. Next, the GNRs were moved away from each other at a constant velocity of 2.0 Å/ns until the GNRs were in the fully separated state. This speed was chosen because it was the fastest the GNRs could be brought together without the system crashing due to unrealistically large overlap between atoms. As the GNRs separated from each other, the state of the system was saved at regular distance intervals. These saved states provided the initial coordinates and velocities for each of the TI simulations representing different values of the order parameter.

The procedure for the second set was almost identical except that, in this case, the GNRs were followed as they came together, rather than pulled apart. In addition, some chains were restrained with a harmonic potential while they were being moved together to prevent them from being pinched between the two GNRs (These restraints were turned off for the duration of the TI simulations). The two sets of TI simulations were continued until the calculated PMFs were nearly identical (See Figure 4.8 for an example). The PMFs themselves were calculated from the final 4 ns of the two TI simulations, and then they were averaged together (effectively making the total sampling time 8 ns). The total time for which each simulations was run is shown in Table 4.2.

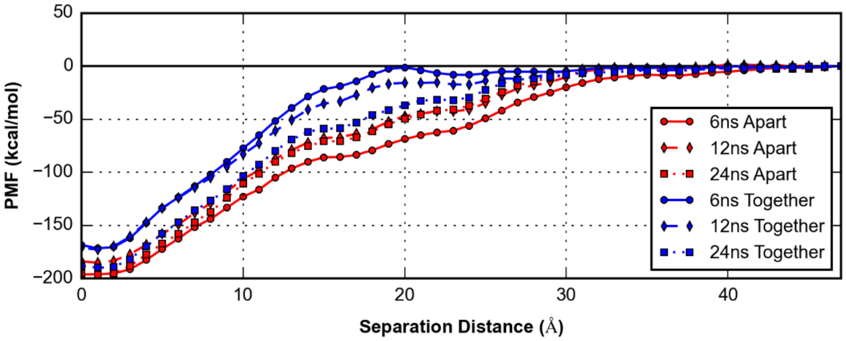

Figure 4.8: PMFs calculated for sliding GNRs with *n*-alkoxy-terminated edges. Each curve represents a set of TI simulations initialized either with the GNRs moving together or apart and run for different total lengths of time.

Table 4.2: Total Simulation Time

| Edge Configuration | Aggregation Path | Simulation Time (ns) |
|---|---|---|
| Hydrogen | Face-to-face | 12.0 |
| *N*-alkoxy | Face-to-face | 18.0 |
| PEG | Face-to-face | 18.0 |
| Hydrogen | Sliding | 12.0 |
| *N*-alkoxy | Sliding | 24.0 |
| PEG | Sliding | 12.0 |

In addition to finding the appropriate equilibration time for these systems, it was also important to quantify the precision of the results. We calculated the standard error for each simulation in the same manner as in Chapter 3:

$$\sigma_{err}^2 = \frac{2t_c}{t}\sigma^2 \tag{4.6}$$

where $\sigma_{err}$ is the standard error, $t_c$ is the correlation time for the property being calculated in a simulation, $t$ is the total length of time in a simulation, and $\sigma^2$ is the variance of the measured property of the simulation. This method of calculating the error is described by Frenkel and Smith, and further details as well as the procedure to calculate $t_c$ can be found in their book [109]. This calculation only provides an estimate and is accurate only to an order of magnitude due to the approximations made as well as statistical error in the calculation itself. However, this is usually sufficient to determine the significance of a result.

In the case of this system, the property being calculated from each simulation is the PMF between neighboring values of the order parameter that are within the set of TI simulations ($\Delta r$):

$$\sigma^2 = \frac{1}{N-1}\sum_{i=1}^{N}\left[\left(\frac{\partial U}{\partial r}\right)_i \Delta r - \left\langle\frac{\partial U}{\partial r}\right\rangle \Delta r\right]^2 \tag{4.7}$$

For each value of the order parameter that was simulated, $\sigma$ was calculated from the combined data of the last 4 ns from both TI simulations. The value of $t_c$ was then estimated by averaging values of $t_c$ calculated from those same two simulations, and $t$ was set to 8 ns.

For the PMFs presented in the next section, it was desirable to construct error bars that represent the error in the PMF with respect to the fully separated GNRs. Therefore, the standard error of each point along the PMF ($\sigma_{err,total}$) was defined as:

$$\sigma_{err,total} = \sqrt{\sum_{i=1}^{n} \frac{\sigma^2_{err,i} + \sigma^2_{err,i-1}}{2}} \tag{4.8}$$

where $n$ is the total number of points simulated along the order parameter away from the largest separation distance, and $\sigma_{err,i}$ is the standard error of the simulated points. The average between two neighboring standard errors squared was necessary for the error bars to be consistent with the trapezoidal method used in the integration. The results of these error estimates are provided in the following sections.

## 4.3 Face-to-Face GNR Aggregation Results

Figure 4.9 shows the final PMFs for each of the GNRs aggregating in a face-to-face manner. Each of the curves are qualitatively similar, with relatively minor (but still significant) differences in energy. The form of these curves are also consistent with others discussed in the literature [80, 90, 53, 52]. Also note that the error bars are typically very small with respect to changes in the PMF.

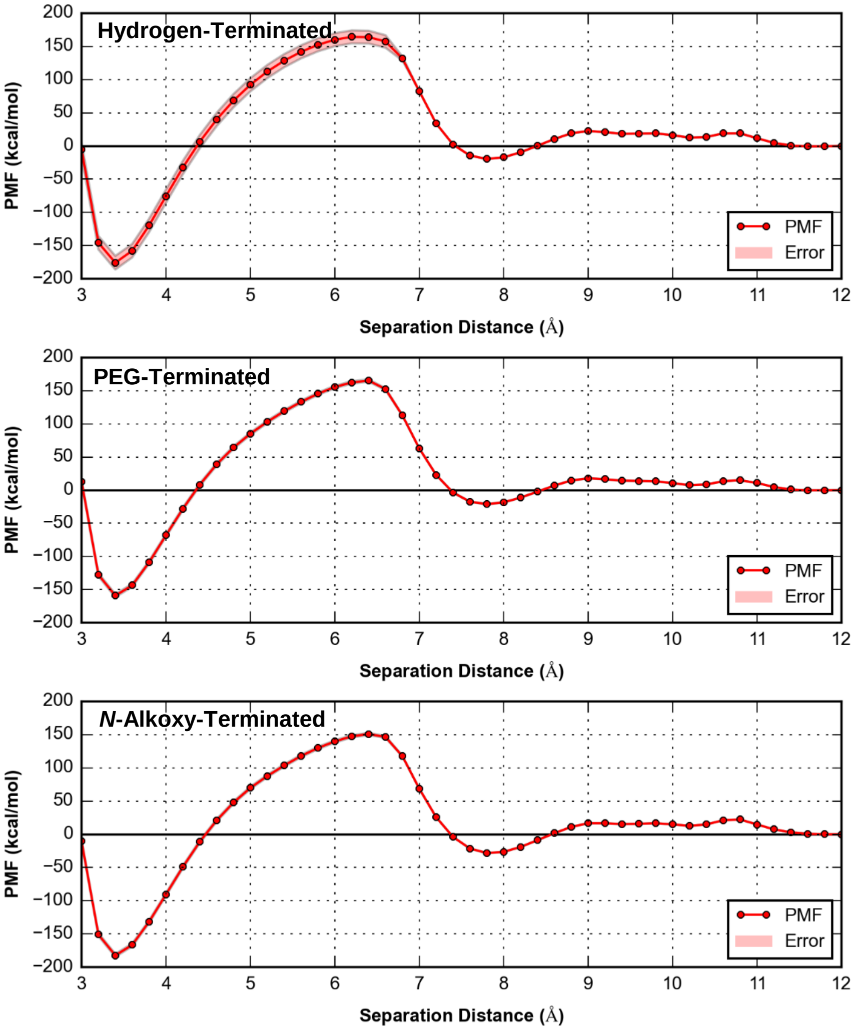

Figure 4.9: Face-to-face PMFs with the separation distance along the $z$ direction. Error estimates are shown as light red shading around the darker red points that denote the average values of the PMF at a given separation. It can be observed that the errors are very small and barely visible in the curves except for the H-terminated case.

There are very significant changes in the PMF of each of the GNRs as they come together. Figure 4.12 shows rendering of the hydrogen-terminated GNRs at important points along the generated PMFs. At 12.0 Å, there are clearly two layers of solvent lying parallel to the GNRs' faces. As the GNRs approach each other, the two solvent layers begin to compress at 10.8 Å. This compression also causes the PMF to begin to rise. At 10.2 Å, the solvent becomes a single layer again, with some solvent molecules lying perpendicular to the two GNRs. This also accounts for the small local minimum in the PMF at this point. Through 9.0 Å to 7.8 Å, these perpendicular solvent molecules rotate to become parallel, resulting in a local minimum in the PMF. Finally, there is a large spike in the PMF at 6.2 Å as all of the solvent is compressed and then forced out from between the two GNRs. Since this vacuum is energetically unfavorable, the PMF quickly decreases until the GNRs come fully together at 3.4 Å.

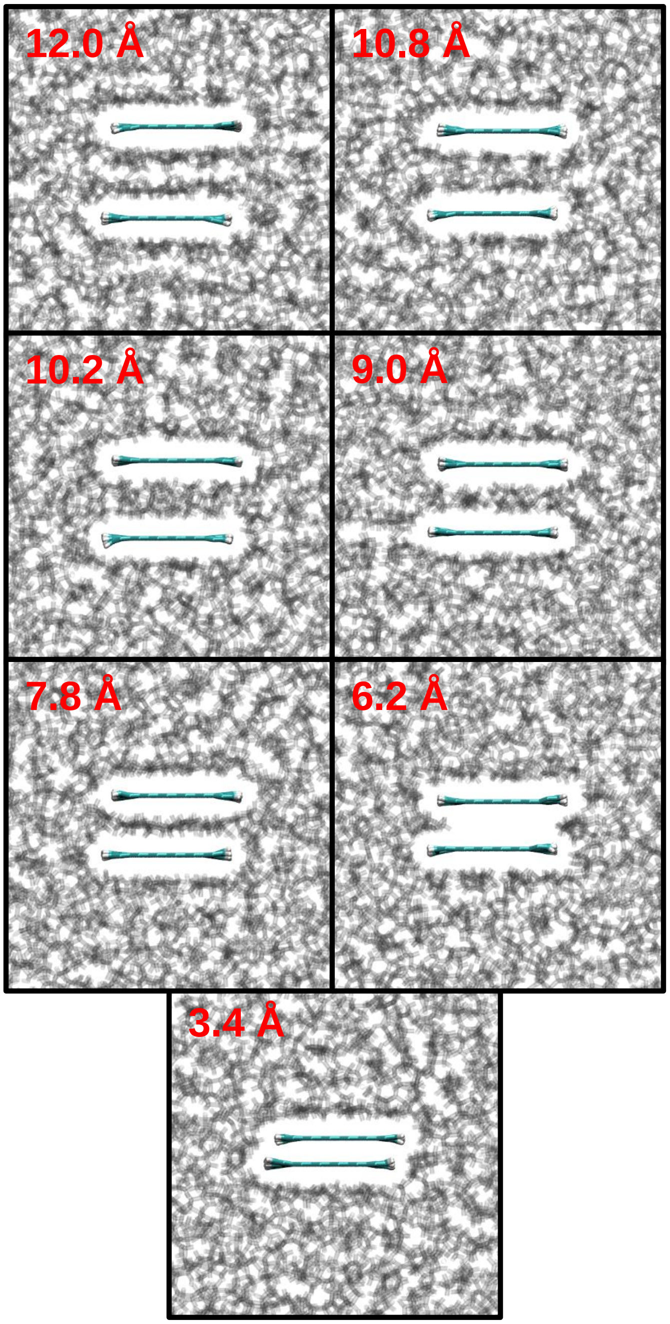

Figure 4.10: Representative cross-sectional images of the aggregation process of hydrogen-terminated GNRs.

Table 4.3 contains both the maximum peak height (at 6.2 Å) and the maximum well depth (at 3.4 Å) in the data presented in Figure 4.9. Regardless of edge configuration, both well depths and peak heights are extremely large. The GNRs have a strong preference to aggregate, but the large peak height indicates that the rate of aggregation along this path would be almost non-existent. However, the barriers and well depths have slightly different values depending on edge configuration. From greatest to smallest values for both the barriers and depths, the edge configurations can be ranked as PEG-terminated, hydrogen-terminated, and *n*-alkoxy-terminated (although the barrier heights of the PEG-terminated and hydrogen terminated GNRs are within their error). In Chapter 3, it was clear that the PEG chains were soluble in NMP, while the *n*-alkoxy chains tended to stick to each other. There was further evidence for this given by the previous ABF calculations that showed that the *n*-alkoxy chains bind to graphene much more strongly than the PEG chains. Since the PEG chains are fully soluble in NMP, they provide some (albeit small) steric repulsion to the approach of the GNRs. However, the *n*-alkoxy chains interact strongly with each other, greatly decreasing the barrier height and the well depth.

Table 4.3: Relevant PMF Values for Face-to-Face Aggregation

| Edge Termination | Max Peak Height (kcal/mol) | Max Well depth (kcal/mol) |
|---|---|---|
| Hydrogen | 164.2 ± 4.4 | 175.7 ± 4.6 |
| PEG | 162.4 ± 0.8 | 159.0 ± 1.1 |
| *N*-alkoxy | 147.4 ± 0.8 | 182.2 ± 1.0 |

## 4.4 Sliding GNR Aggregation Results

Figure 4.11 shows the resulting PMFs of the three GNR types that were brought together in a sliding trajectory. Unlike the face-to-face trajectories, there are very significant qualitative differences in the PMFs themselves. Figures 4.12 through 4.14 show renderings of GNRs with hydrogen-, PEG-, and *n*-alkoxy- terminated edges, respectively. For the hydrogen-terminated aggregation, features in the PMF begin at 26.0 Å. The first peak here corresponds to the breaking of a small solvent barrier between the two GNRs, much like the face-to-face case at 9.0 Å. At 23 Å, a single layer of solvent forms, and then there is a small peak at 19 Å where there is vacuum between the two GNRs. The difference in magnitude of the peaks for the sliding case compared the face-to-face case demonstrate the sensitivity of the PMFs to changes in surface area and different relative orientations of the GNRs. At 16.0 Å, the GNRs are in direct contact with each other. At 19.0 Å, the flexible and charged edge groups pass each other, and the slope of the PMF increases in magnitude. Finally, an aggregated state occurs at a 1.0 Å separation distance.

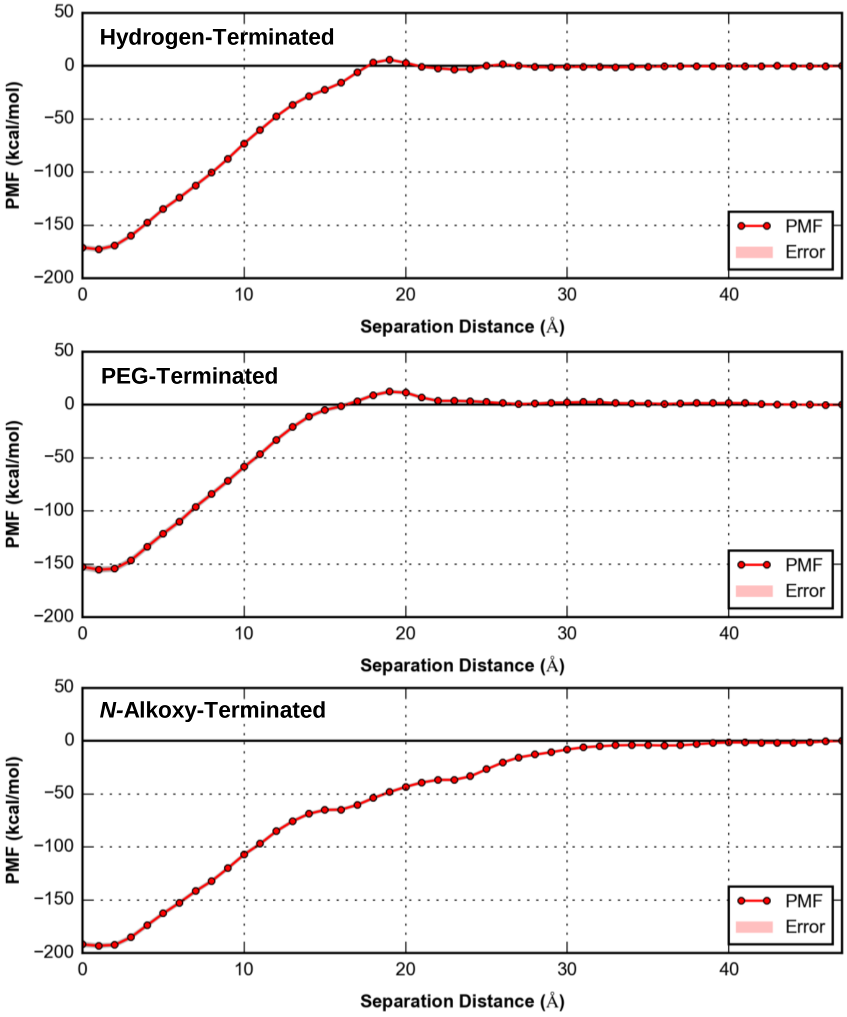

Figure 4.11: Sliding PMFs with the separation distance along the *x* direction. Again, very small errors are present in the calculations.

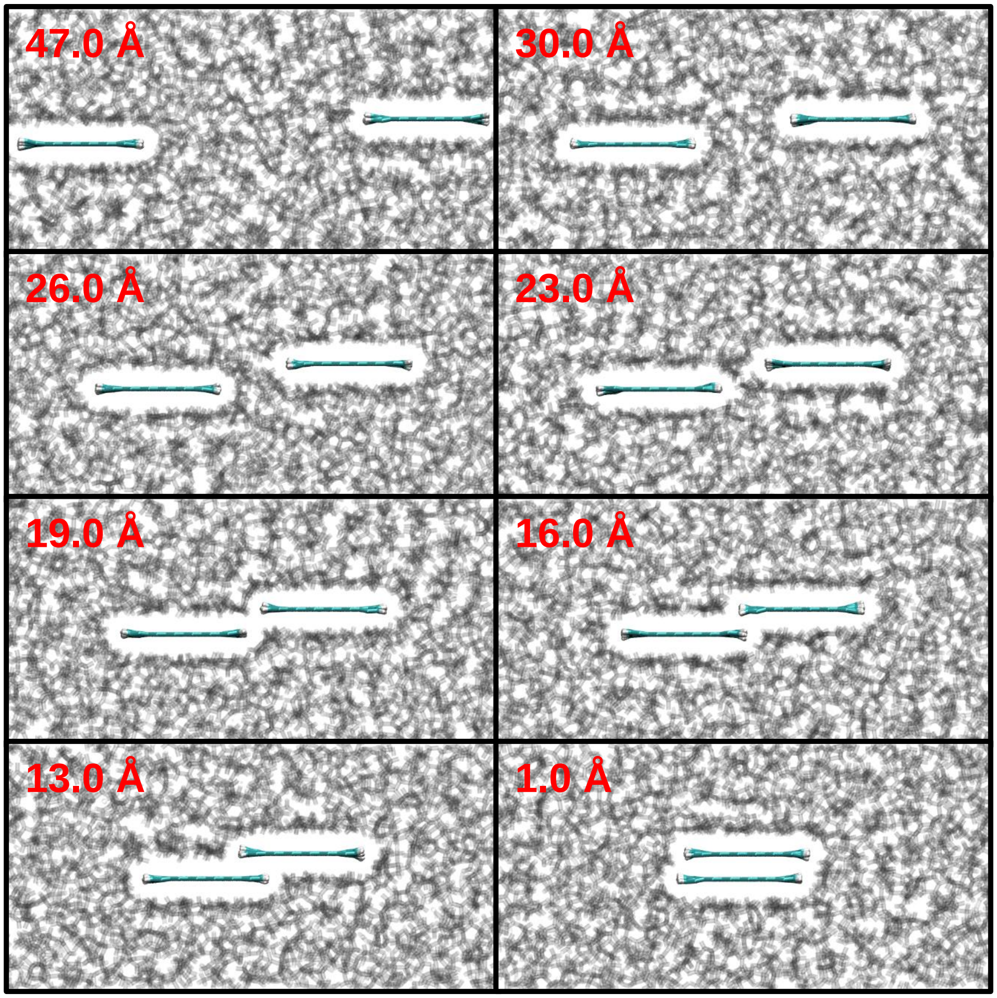

Figure 4.12: Representative cross-sectional images of hydrogen-terminated GNRs following a sliding path. Distances between the GNRs in each pane are shown in red. Key as in the preceding figure.

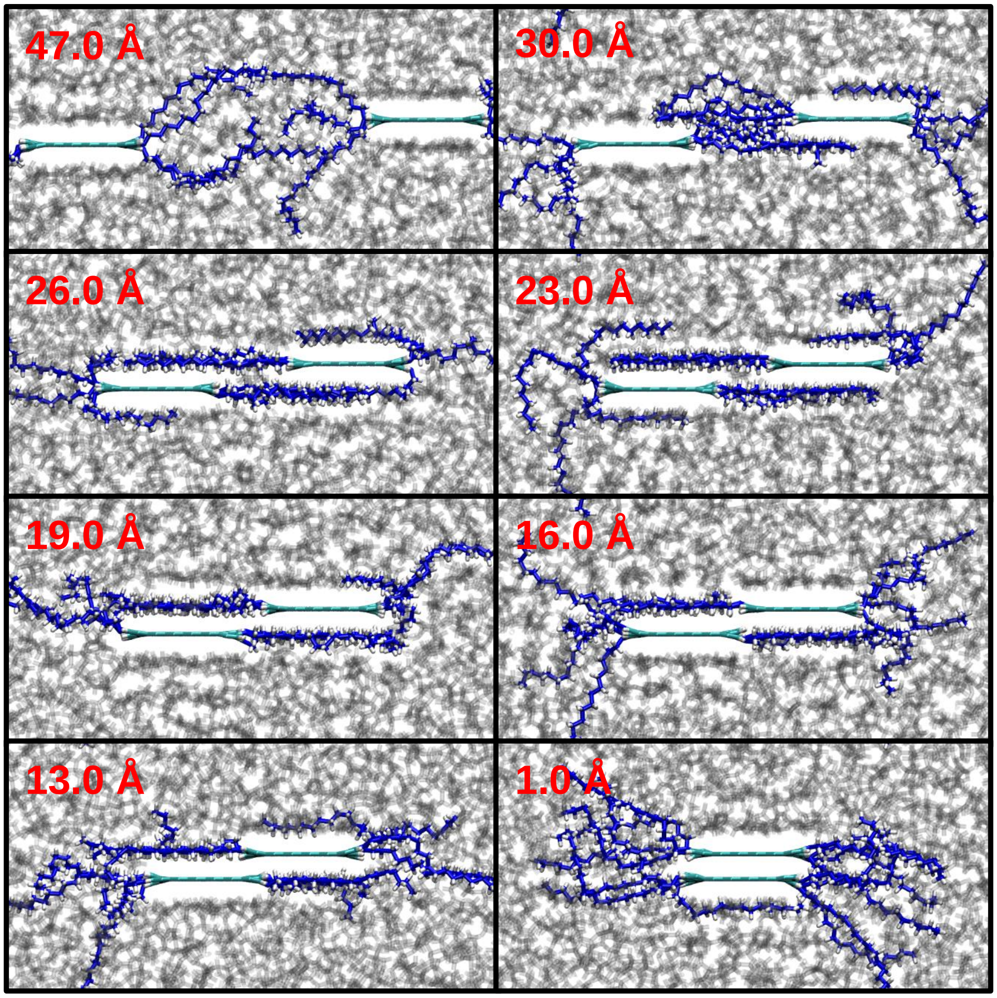

Figure 4.13: Representative cross-sectional images of *n*-alkoxy-terminated GNRs following a sliding path. Key as in the preceding figure.

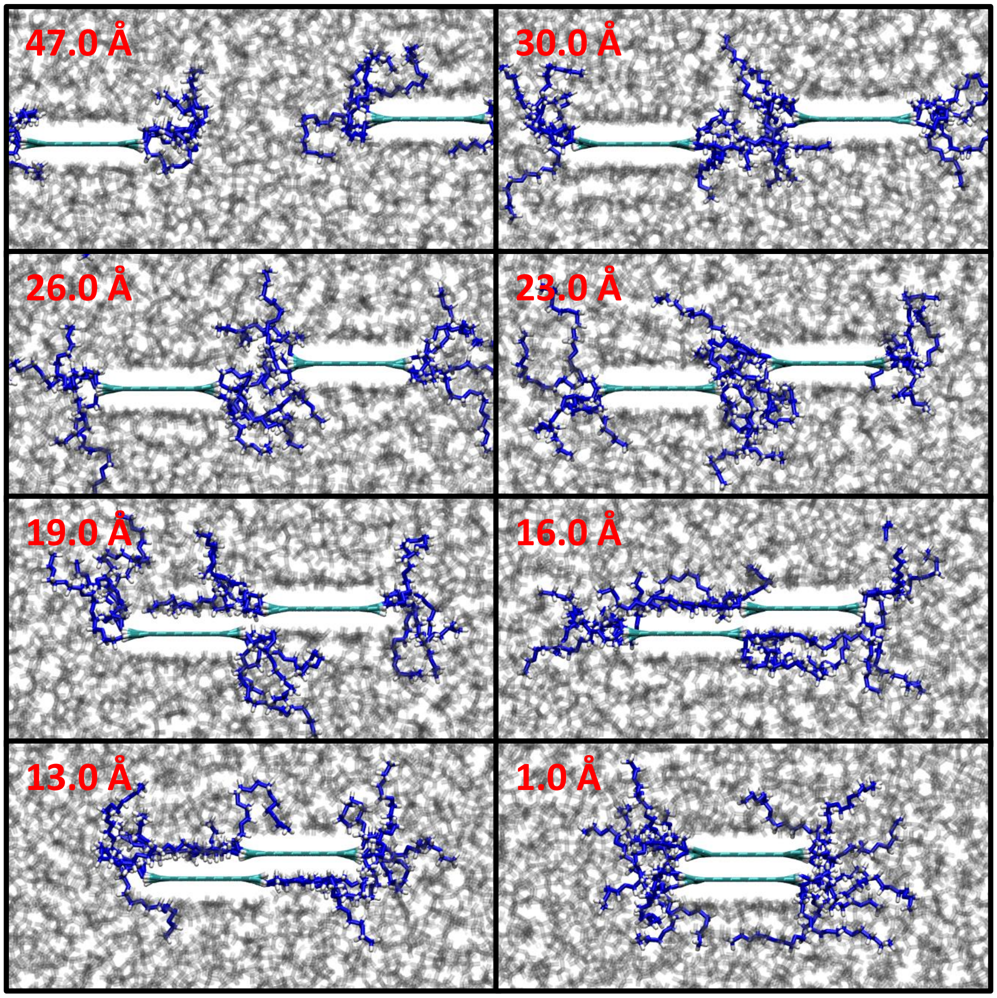

Figure 4.14: Representative cross-sectional images of PEG-terminated GNRs following a sliding path. Key as in the preceding figure.

The side-chains serve to perturb the PMF generated by hydrogen-terminated GNRs. Major changes in the PMF for PEG-terminated GNRs begin at 26 Å. The PEG chains interfere with the solvent layers described for the hydrogen-terminated case. The increased barrier at 19 Å is due to steric congestion from the PEG chains. The effects of the *n*-alkoxy chains are much more severe. There is no barrier present and, at 30.0 Å, the *n*-alkoxy chains adsorb onto the neighboring GNR and pull them together. This is another manifestation of the fact that *n*-alkoxy chains adsorb more strongly onto the GNR.

Table 4.4 shows the maximum barrier heights and well depths for the different GNR types. The well depths display similar values to the face-to-face cases. The PEG-terminated GNR involves a barrier along the sliding trajectory that is more than twice that of the hydrogen-terminated GNR. The case for the *n*-alkoxy-terminated GNR exhibits no barrier, showing that the *n*-alkoxy chain catalyzes aggregation in this case.

Table 4.4: Relevant PMF Values for Sliding Aggregation

| Edge Termination | Max Barrier Height (kcal/mol) | Max Well depth (kcal/mol) |
|---|---|---|
| Hydrogen | 5.9 ± 0.5 | 172.6 ± 1.2 |
| PEG | 12.3 ± 0.9 | 155.2 ± 2.0 |
| *N*-alkoxy | N/A | 193.0 ± 1.4 |

## 4.5 Aggregating GNRs with no additional restraints

While the previous calculations clearly ranked the different side-chains in terms of the barriers to aggregation, the constraints put on the GNRs clearly had a significant effect on the values of those barriers as well as the qualitative form of the PMFs. While calculating a PMF where the system is fully unrestrained is not feasible, it would be interesting to see how unrestrained GNRs might approach each other. To investigate this, we first initialized a simulation box with hydrogen-terminated GNRs separated by 18.0 Å. Here, instead of the TI method used for the free energy calculations described above, we employed Steered Molecular Dynamics (SMD) in which a slowly retracting harmonic potential was added to the center of mass of the two GNRs. The retraction speed was set at a constant 1.0 Å/ns. Renderings of different times in the simulation are shown in Figure 4.15. From the start of the SMD simulation to a separation distance of 12.6 Å, the GNRs approach each other in a face-to-face fashion. To continue along the face-to-face path at this point, the GNRs must compress the solvent and cause some of it to evacuate from between the GNRs creating large energy barriers as shown in Figure 4.9. In order to minimize the barrier present, the GNRs were always observed to rotate with respect to each other such that they form a cross. When there is only a single layer of solvent left, the GNRs respond by bending outwards rather than push through the final large energy barrier that would be present in face-to-face aggregation at 5.9 Å separation. The bending continues to increase until the edges of the two GNRs come into contact with each other, seen in the foreground at 3.9 Å separation. Contact between the two GNRs catalyzes the aggregation and the GNRs quickly come together much like a zipper, forcing all the solvent to evacuate from in-between them (

3.7 Å separation). Finally, the GNRs rotate such that they virtually eclipse each other in a fully aggregated state (2.7 Å separation). The separation distances are smaller than expected from the face-to-face results. However the GNRs curve around each-other towards the end of the simulation, causing the centers of mass to be closer than the shortest separation distance between the two GNR faces.

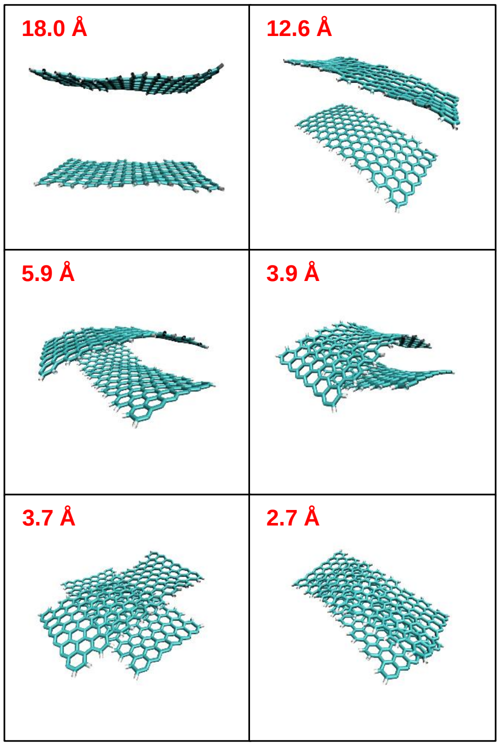

Figure 4.15: Representative images of GNRs being pulled together *via* SMD. The distance between centers of mass of GNRs corresponding to the image is shown in red. Solvent is not shown for clarity.

We repeated the simulation for four different initial orientations of the hydrogen-terminated GNRs, as well as for the PEG- and *n*-alkoxy- terminated GNRs. In each case, while the initial path was dependent on the initial orientation, the trajectory taken from a trajectory of 12.6 Å and onward was qualitatively identical. While there is no evidence that this is the most common aggregation path, two conclusions can be drawn from the simulations. First, the GNRs avoid the full face-to-face aggregation path, even if this means that the GNRs must come together crosswise with respect to each other. This is not surprising given that there is such a large barrier for this mechanism (Figure 4.3). Second, as soon as any contact is made between the GNRs, the solvent is quickly evacuated between the GNRs, allowing the GNRs to become fully aggregated.

## 4.6 Discussion

It is clear that the PMF of GNRs is very different depending on the path to aggregation that was taken in each of the sets of TI simulations. Since the highly constrained simulations required an large amount of time to run (each TI simulation ran for 24 ns at a 2.0 fs time step for the *n*-alkoxy following the sliding trajectory, for example), it is unlikely that a fully unrestrained simulation would be feasible. Therefore, it is also unlikely that the true path towards aggregation can easily be found. Despite this fact, it is clear that these TI calculations provided helpful and consistent data. The face-to-face and sliding aggregation paths highlighted two extreme cases that illustrate how GNRs might approach each other. In both cases, the edge configurations were consistently ranked in terms of their barrier height and their aggregation well depth in the calculated PMFs.

The SMD simulations provided a different, and importantly less biased, path by which the GNRs could come together, which could be understood qualitatively through insight gained from the face-to-face and sliding paths calculated through TI. As the GNRs approached each other, they strenuously avoided coming into contact with each other in a face-to-face fashion due to the enormous energy barrier that this configuration would require passing through. This involved rotating crosswise and bowing outwards to circumvent this large barrier. The GNRs finally came into contact with each other along the edges, for which, through the preceding TI calculations for the sliding path, it is known that the barriers are very small. Once the edges of the GNRs touch, all of the solvent can easily be evacuated between them, allowing the GNRs to became fully aggregated. The SMD simulation also demonstrated that only a small portion of the edge needed to come into contact with the other GNR in order for aggregation to occur. In the sliding aggregation path, a full GNR edge came into contact with another GNR edge. Even though the barriers were relatively small for the sliding aggregation path, it is likely that the true barriers are even smaller.

Regardless of the aggregation path chosen, the ranking among the three edge configurations, from lowest to greatest maximum barrier height and aggregation well depth, were the *n*-alkoxy-terminated edges, the hydrogen-terminated edges, and the PEG-terminated edges. The reason for this is highlighted in the ABF calculations performed on single chains adsorbing on graphene and the binding enthalpy studies discussed in Chapter 3. The *n*-alkoxy chains prefer to adsorb onto other *n*-alkoxy chains or onto the GNRs themselves rather than move freely through the solvent. This adsorption effect appears to catalyze the aggregation reaction, making the system less dispersible than if there were no side-chains added at all. In fact, it is likely the *n*-alkoxy chains completely remove the barrier to aggregation, as demonstrated by the sliding aggregation path TI calculations. However, the same is not true for the PEG chains. Chapter 2 showed they were readily soluble in the NMP solvent. In addition, the free energy of adsorption on graphene was less than a third of that for the *n*-alkane chain. Where the *n*-alkoxy chain catalyzed the aggregation process through adsorbing onto the neighboring GNR, the PEG chains provided an additional energetic barrier through steric repulsion. Despite the benefits that the PEG chains provide, their effect is miniscule compared to the overall aggregation well depth ( $>$ 150 kcal/mol ). The PEG chains decreased this well depth by 17 kcal/mol. Therefore, all of these systems will have a strong tendency to aggregate out of dispersion.

Ideally, free energy calculations, as presented here, could be used to test different edge configurations before they are synthesized in the lab. First, a quick enthalpy analysis, similar to that presented in Chapter 3, will provide insight into the disposition of the side-chains and the favorability of the GNRs binding to each other. Next, TI calculations should be made, sampling along different paths, to rank the dispersibility of candidate edge configurations. Unfortunately, the TI calculations here were computationally expensive. The PMF calculated for *n*-alkoxy terminated GNRs following a sliding path is Figure 4.11 had a total simulated time of 2.256 $\mu$s. With a 2.0 fs time step, this constituted a simulation involving well over $1 \cdot 10^9$ MD integration steps.

There are several ways this could be sped up. First, the features in the PMF that differentiated the edge-configurations occurred over small ranges of the order parameter (the points around 19.0 Å for the sliding path, for example). Rankings could be accomplished by just examining these regions. This would significantly decrease the computational costs of the TI calculations. Also, while full GNRs were used in this study, there is no reason why smaller GNR segments should not be used to provide qualitatively similar results. Finally, if intuition is built on how long the simulations need to be run in order for the side-chains to fully equilibrate, running two sets of TI simulations for each aggregation path becomes unnecessary. This would reduce, by half, the computational cost for running these simulations.

## CHAPTER 5

# ELECTRONIC PROPERTIES OF AGGREGATED GNRS

In Gao *et al.*, experimental evidence was provided by our collaborators at Princeton and Cornell for the "bottom-up" synthesis of GNRs (Dichtel and students) and deposited on a substrate to fabricate field-effect devices (Gao and Loo) [1]. The synthesis of the GNRs was carried out in solution by benzannulating and subsequently cyclodehydrogenating poly(*p*-phenylene ethylene). Figure 5.1 shows the final product. The synthesized GNRs also featured dispersing hexa(ethylene oxide) side-chains. After being synthesized, the GNRs were deposited on either Cu foil or a $SiO_2$ dielectric by aerosol-assisted chemical vapor deposition. The GNRs on Cu were coated with PMMA and the copper was etched away. The GNRs on PMMA were then also transferred to a $SiO_2$ dielectric. Gao *et al.* defined contacts and as well as source and drain electrodes through a combination of photo- and E-beam lithography. Finally, the source and drain electrodes that were connected by deposited aggregates of GNRs were formed into field effect devices that were tested for their electronic properties.[1]

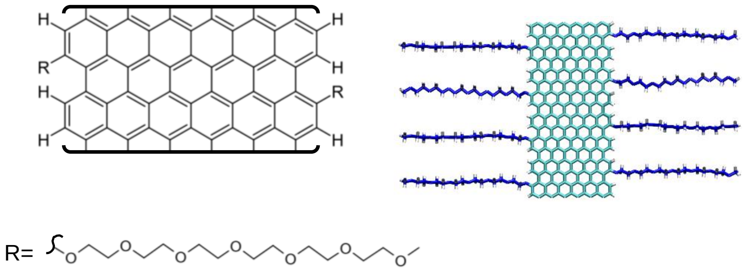

Figure 5.1: Structure (left) and rendered image (right) of a GNR with hexa(ethylene oxide) side-chains

The hexa(ethylene oxide)-terminated GNR used in this study is very similar to the PEG chains and grafting density used in Chapter 4. The only differences are, first, there are two additional atoms making up the chain and, secondly, the chains are offset on one side of the GNR with respect to the other. In addition, the GNRs were dispersed in chloroform, dimethlyformamide (DMF), and NMP. The GNRs dispersed to concentrations of 0.5 mg/mL in DMF and NMP, and of 50 $\mu$g/L in chloroform. While the GNRs are somewhat dispersible in these solvents, it is likely that they will aggregate prior to aerosolization and perhaps during aerosolization and deposition. The field-effect devices were fabricated on top of the GNRs whether they were in an aggregated state or not. In addition, the side-chains might affect the electronic properties of the GNRs either through being bonded with the rest of the GNR or by wrapping around them. In collaboration with Gao *et al.*, we investigated this issue using computational techniques.

In this chapter, we discuss the electronic and optical band gaps of single and bilayer (two, stacked) hydrogen-terminated GNRs (H-GNRs) and single methoxy- terminated GNRs (MeO-GNRs) using very accurate GW and BSE methods. These results are correlated with DFT-generated band structures with the HSE functional. These DFT calculations are used to investigate irregular stacking and side-chain wrapping. Finally, these results are used to interpret some of the properties of the GNRs just discussed. Appendix B provides example input scripts to Quantum Espresso and Yambo to show how the calculations described in this section were executed.

## 5.1 Electronic band gaps calculated using the GW method

In this section, we will discuss calculating the electronic band gaps of GNRs using the $G_0W_0$ approach. Here, electronic band gaps are defined as the energy difference between the highest energy quasiparticle hole and the lowest energy quasiparticle electron. $G_0W_0$ and BSE calculations are extremely computationally expensive. Therefore, only a subset of the systems of interest to us could be directly investigated (Figure 5.2). In addition, smaller numbers of $k$-points and energy cut-offs had to be used than are desirable. We will discuss the effects of these approximations on the results.

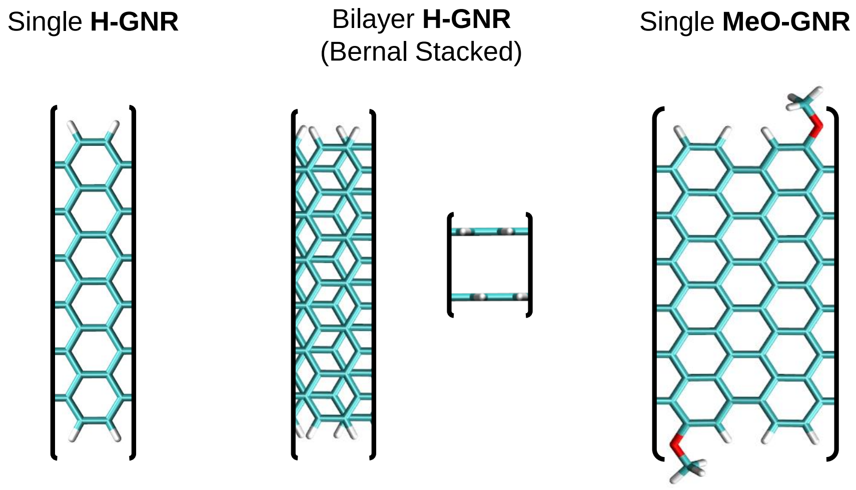

Figure 5.2: Representative images of the three systems under study in this chapter: the unit cell of a single hydrogen-terminated GNR, or H-GNR (left), the unit cell of a bilayer H-GNR (center), and the unit cell of a methoxy-terminated GNR, MeO-GNR (right).

Before calculating the energies of the single particle excitation energies, the ground state energies were calculated by DFT using Quantum Espresso [92]. We used Martins-Troullier norm-conserving pseudopotentials to model the core electrons in the system with a 30.0 Ry kinetic energy cut-off and 10 *k*-points along the periodic direction in the irreducible Brillouin zone. While the separation distance between neighboring GNRs between the unit cell was maintained at 21.2 Å (40.0 bohr), the unit cell length and geometry were optimized using the PBE functional with the force convergence threshold set at 0.4 eV/Å. The DFT optimization found the unit cell lengths for both the single and bilayer H-GNRs to be 4.13 Å. Without a suitable dispersion correction for the bilayer GNRs, the GNRs were stacked in a Bernal pattern with a 3.35 Å separation. Finally, we used the Perdew-Wang LDA functional to perform a final SCF run to make the output data compatible for use in the Yambo code, and make the results consistent with similar past studies [101, 33, 111].

### 5.1.1 Random Integration Calculations

An additional complication with simulating single particle excitations in 0D, 1D, and 2D materials using periodic boundary conditions makes it necessary to make an additional modification to the ground state calculations before doing the full $G_0W_0$ calculations. The effects of a single particle excitation can be felt, and responded to, by very long distances due to the 1/r rate of decay from the Coulombic interaction [112]. This is especially true for the electrons in GNRs from neighboring unit cells. The GNRs running parallel to each other constitute an effective dielectric medium that effects the quasiparticle energy levels (Figure 5.3). Separation distances used in the DFT calculations (40.0 bohr) were sufficient for ground state calculations because the system is charge-neutral, and any Coulombic effect decays much faster than 1/r. This is not the case for single particle excitations. We calculated the electronic band gap on small GNRs (7.3 Å across, shown in Figure 5.3) with different separation distances. The electronic band gap grows almost linearly from a 40.0 bohr separation to a 60.0 bohr separation. It is clear that the separation distance would have to be very large for there to be no effect from nearest neighbors, which would make the calculations infeasible. Instead, the Coulombic interactions were screened between nearest neighbors to prevent these interactions from occurring.

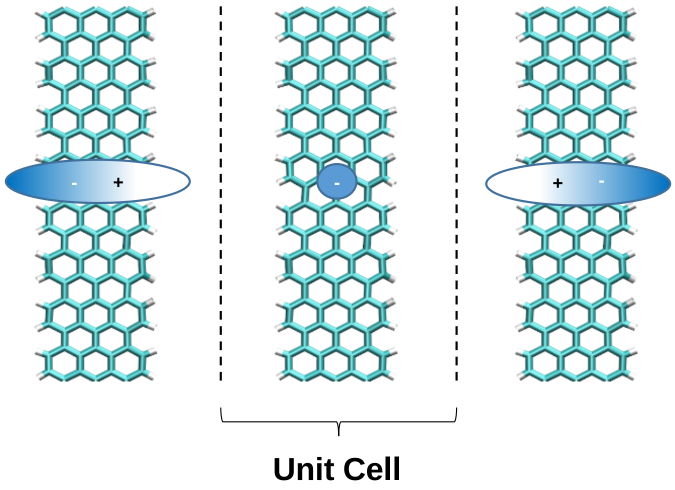

Figure 5.3: Electrons in neighboring (image) GNRs responding to the quasiparticle electron in the central GNR unit cell.

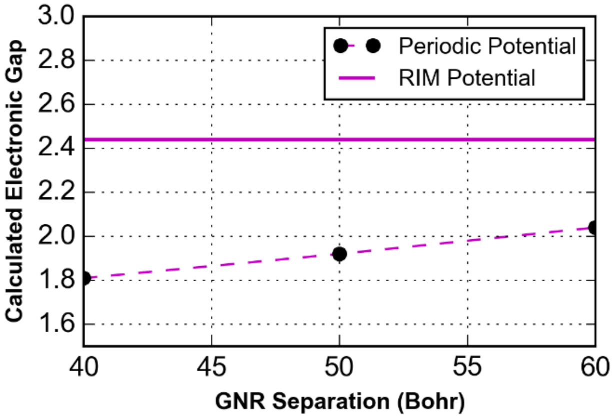

Figure 5.4: Electronic band gaps calculated with the default periodic potential (shown as black dots connected by a purple dashed line to guide the eye) and the screened potential using the Random Integration Method (RIM), shown as a solid purple line.

The Coulombic potential, $V$, due to the electronic density can be written in terms of real space and reciprocal space (the latter being relevant for periodic calculations) as shown in Equations 5.1 and 5.2 [112].

$$V(\mathbf{r}) = \int n(\mathbf{r}')v(|\mathbf{r} - \mathbf{r}'|)d^3\mathbf{r} \tag{5.1}$$

$$V(\mathbf{G}) = v(\mathbf{G})n(\mathbf{G}) \tag{5.2}$$

Here, $v$ is the Coulombic interaction and $n$ is the electronic density [112]. $\mathbf{G}$ is a reciprocal lattice vector $(2\pi/L)N$, where $L$ is a lattice parameter and $N$ is an integer. To screen the Coulombic interaction, Equation 5.2 is reformulated as shown in Equation 5.3.

$$\widetilde{V}(\mathbf{G}) = \widetilde{v}(\mathbf{G})\widetilde{n}(\mathbf{G}) \tag{5.3}$$

$$\widetilde{v}(\mathbf{r}) = \begin{cases} 1/r & \mathbf{r} <= \mathbf{r_B} \\ 0 & \mathbf{r} > \mathbf{r_B} \end{cases} \tag{5.4}$$

The effect of the redefined Coulombic potential is to eliminate interactions outside of a certain boundary (here $\mathbf{r_B}$). $\widetilde{n}$ is identical to $n$ except that care must be taken to ensure that the electron densities are not interacting with each other across unit cells [112]. Assuming the GNR is periodic in the $y$ direction and not in the $x$ and $z$ directions, the equation for $\widetilde{v}$ in reciprocal space comes out to be:

$$\widetilde{v}(\mathbf{G}) = \int_{-x_B}^{x_B}\int_{-\infty}^{\infty}\int_{-z_B}^{z_B} \frac{exp\left(-i\left(G_x x + G_y y + G_z z\right)\right)}{\sqrt{x^2 + y^2 + z^2}} dxdydz \tag{5.5}$$

In practice, this is solved by using a Monte Carlo integration scheme using Yambo [101]. The cut-off was selected at a 40.0 bohr separation between GNRs in neighboring unit cells for the H-GNRs described above. This method was also tested on the smaller GNRs shown in Figure 5.3. The corrected band gap is shown as the RIM (Random Integration Method) potential line in Figure 5.4.

### 5.1.2 $G_0W_0$ Calculations and the Electronic Band Gap

Figure 5.5 shows the quasiparticle energies for the single and bilayer H-GNRs, with electronic band gaps of 2.14 eV and 1.51 eV, respectively. We calculated the $G_0W_0$ energies by using a polarization response block size of 2 Ry and 50 empty bands for calculating the polarization and $W$. These cut-offs are typically considered too low for calculating accurate $G_0W_0$ energies. However, tests were made with H-GNRs that had only 6 $k$-points in the irreducible Brillouin zone. It was found that the quasiparticle energies were largely unaffected by changes in response block size from 2 Ry to 8 Ry (The latter being used by Denk *et al.* in their study of GNRs) [113]. From 50 to 300 empty bands used, the absolute quasiparticle energies can vary greatly, by up to 0.1 eV. However, the variation in the relative differences in quasiparticle energies, specifically the electronic band gap, was almost completely insensitive to changes in cut-off. With the response block increased from 2 Ry to 8 Ry, there was only a 0.0001 eV change in the band gap. Changing the number of empty bands from 50 to 300, only produced a difference of 0.00022 eV. In addition, the plasmon-pole approximation was used to calculate $W$ [114].

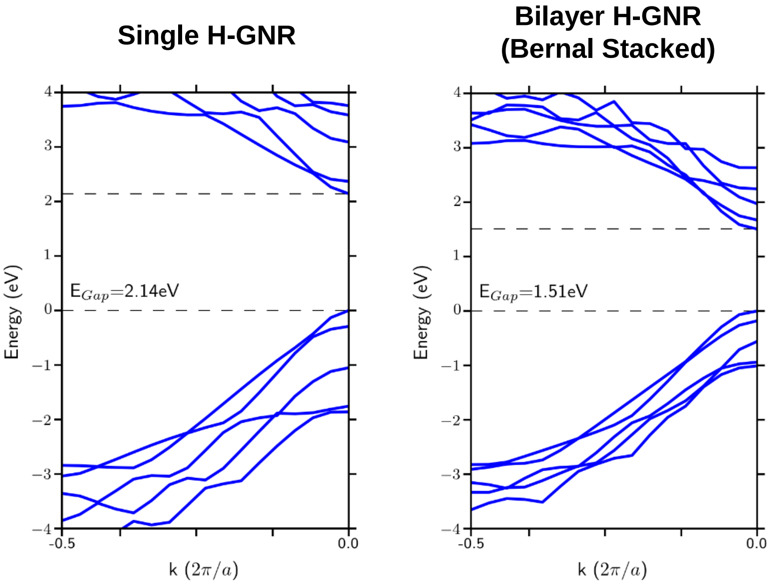

Figure 5.5: Bands calculated with the $G_0W_0$ approximation. $a$ is the lattice parameter, and the energy is set to 0 at the maximum value of the valence band.

Experimental measurements of the electronic band gap for single H-GNRs of the same width as those used in this study found the gap to be 1.4 eV, much smaller than the 2.1 eV calculated in this study [115]. However, the magnitude of the calculated band gaps are consistent with those calculated for other GNRs [33]. The discussion about screening the Coulombic potential demonstrates why this difference might be occurring. It is clear than the electronic band gap in GNRs changes substantially if it is near another polarizable medium. Studies comparing $G_0W_0$ results to those from experiment show that an image charge correction, corresponding to the substrate on which the GNRs are placed, must be included in order for the results to match [116, 113]. This, in combination with the significant decrease in band gap due to making the GNR bilayer, makes it clear that, in an electronic device, the properties of the GNRs are going to be very sensitive to their environment.

In addition, $G_0W_0$ calculations were made on a single MeO-GNR. The methoxy-terminated edges were used instead of the full-length side-chains to save on computational resources as they are not expected to affect the electronic properties of the material significantly. In order for the calculations to be feasible, the number of empty bands used for calculating the polarization and $W$ was reduced to 40. However, a total of 17 k-points were used. The band structure shown in Figure 5.6 shows that the calculated electronic band gap is 2.22 eV, slightly higher than the single hydrogen-terminated GNR. This is due to a combination of the steric congestion along the edges, and the electronegative character of the oxygen atoms bonded along the edges.

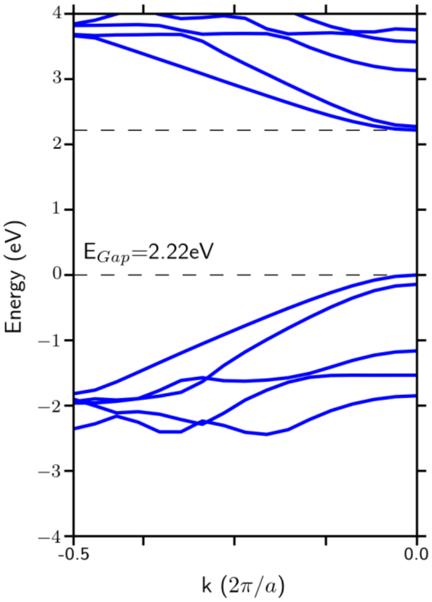

Figure 5.6: Bands calculated with the $G_0W_0$ approximation for the MeO-GNR. *a* is the lattice parameter, and the energy is set to 0 at the maximum value of the valence band.

### 5.1.3 BSE Calculations and the Optical Band Gap

Gao *et al.* measured the fluorescence spectrum of the GNRs in dispersion.[1] A large peak was located at 0.88 eV and a smaller one at 1.03 eV. In a previous study, it was shown that BSE calculations could calculate the peaks in the experimental fluorescence spectrum for GNRs to within 0.2 eV [113]. Therefore, it made sense to do the same with the GNRs in the current study. The cut-offs used in the previous section were also used in these calculations. We only used excitations between the 10 highest energy bands below the Fermi level and the 10 lowest energy bands above the Fermi level because they were sufficient to model the fluorescence spectra within the range provided by Gao *et al*.[1] In addition, we only used the resonant part of the Bethe-Salpeter kernel. We made separate calculations for singlet and triplet excitations (although the latter is not expected to make a significant impact on the experimental results). The triplet excitations were calculated in an identical fashion to the singlet calculations, except that the exchange term in the Bethe-Salpeter Kernel was neglected in the triplet case.

The resulting calculated spectra for both the single and bilayer H-GNRs are shown in Figure 5.7 (A Lorentzian broadening with a full width at half maximum of 0.02 eV was used to facilitate comparison with the experiment). Immediately, it is clear that there is a significant difference between the electronic and optical band gaps of the system. The 1.0 eV difference is due to the Coulombic interaction between the excited hole and electron, which is consistent for calculations of other GNRs and makes sense for materials in small dimensions [113, 111]. While the calculated optical band-gap is close to the experimental value (0.88 eV), the features present do not match the experimental spectrum.

One reasonable possibility is that the experimental spectrum is a combination of both single layer and bilayer H-GNRs. However, the calculated value for that case is too low (0.72 eV). The optical spectrum for MeO-GNRs was calculated to investigate this further.

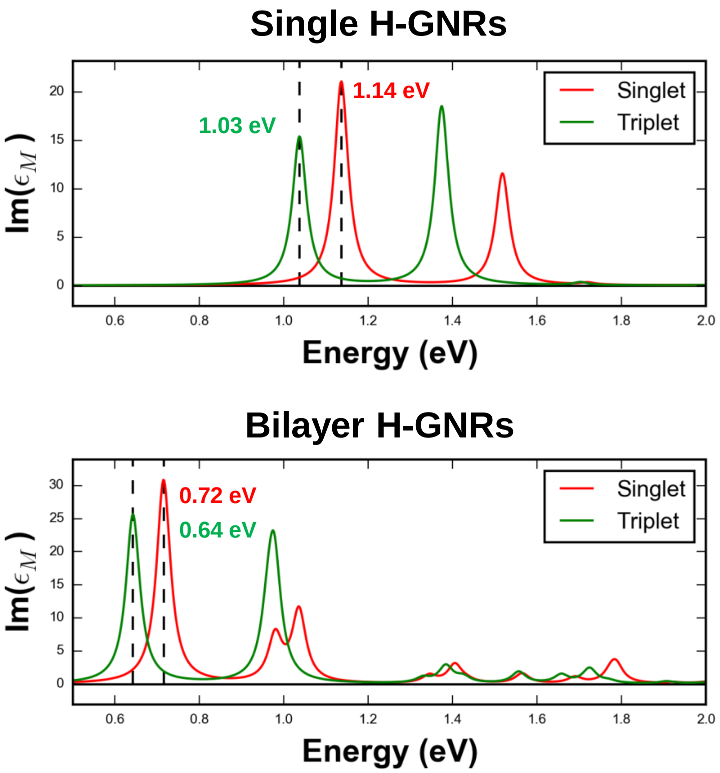

Figure 5.7: Simulated Spectra for Single (top) and Bilayer H-GNRs (bottom).

The optical spectrum for MeO-GNRs was calculated as shown in Figure 5.8 using both resonant and anti-resonant parts of the Bethe-Salpeter kernel. Unlike the single H-GNR case, there are more features with the lowest energy excitation at 1.15 eV. The differences are again due to the combination of adding an oxygen atom on the sides, and causing the GNR to warp. Figure 5.9 shows a zoomed-in image of the features in the spectrum in comparison to the experimental spectrum. The calculated peaks are shifted to higher energies and do not quite match up with the experimental results. However, there are several reasons that might explain these differences. As mentioned before, the energy thresholds are too low, and the use of more *k*-points might change the features in the spectrum [117]. In addition, the experimental spectrum was taken in dimethylformamide, and that difference in solvent might well affect the shifting of the results [118]. Also, the fluorescence spectrum and the calculated spectrum do not represent identical processes. Nevertheless, the calculated spectrum is promising; it suggests that it is reasonable that the detailed features in the experimental spectrum are due to the incorporation of side-chains, rather than defects or aggregation in solution. Figure 5.10 shows a rendered representation of the calculated exciton at 1.15 eV. The proximity of the electron around the hole is an indication of the significant coulombic attraction between them This attraction is also the cause of the significant difference between the electronic and optical band gaps.

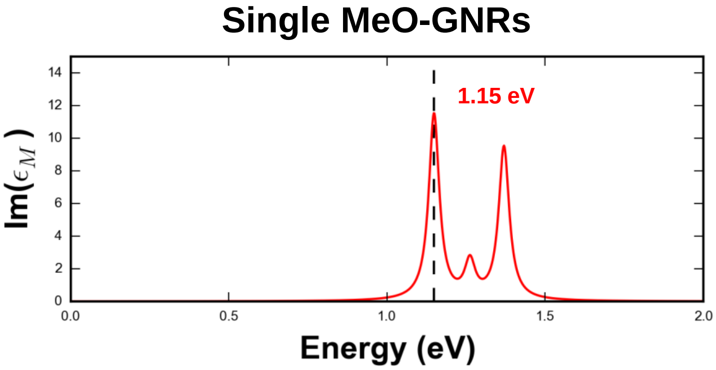

Figure 5.8: Simulated Spectrum for MeO-GNRs.

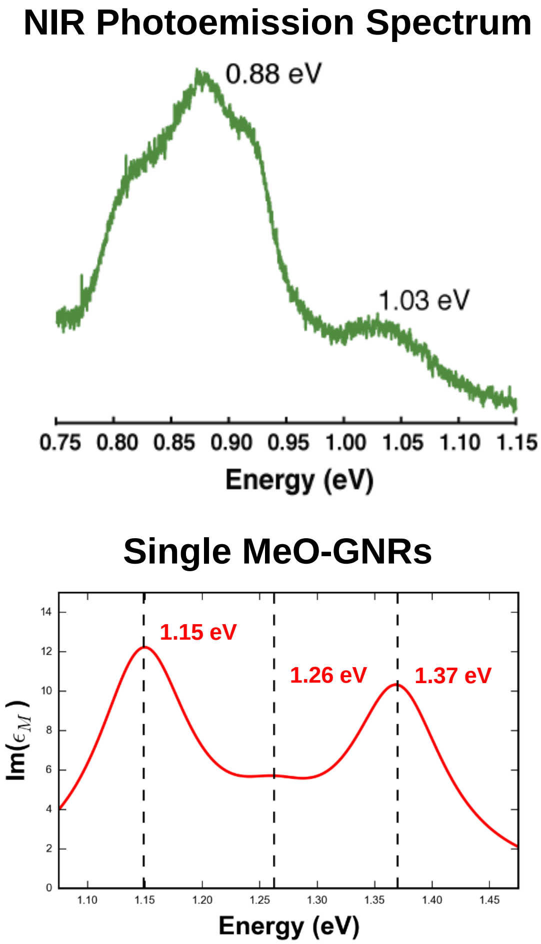

Figure 5.9: Experimental fluorescence spectrum (top) and calculated spectrum for MeO-GNRs (bottom).

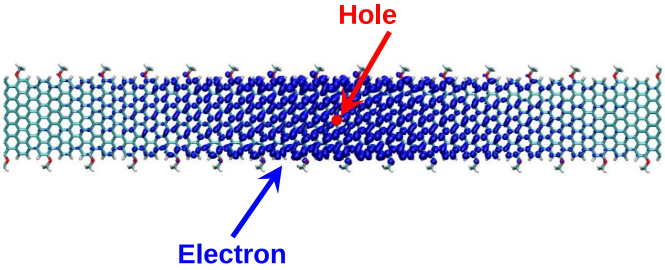

Figure 5.10: A GW results-rendered image of the 1.15 eV exciton on MeO-GNR, with the red dot representing a particular position of a hole and the blue dots representing the places where the likelihood of finding the electron is highest, given the location of the hole. Cyan shows locations with a lower probability of finding the electron.

## 5.2 DFT Calculations using the HSE functional

$G_0W_0$ and BSE calculations are prohibitively computationally expensive. Instead, it would be desirable to calculate band gaps in a less computationally expensive manner using DFT. While DFT is a method for calculating ground state energies only, the HSE functional serendipitously calculates accurate optical band gaps for GNRs [119]. In order to verify this, GNRs were simulated using Gaussian 09 [81]. Unlike Quantum Espresso, Gaussian uses Gaussian basis sets, and the periodic boundary conditions have to be treated differently such as using the fast multipole method for long-range interactions [120]. All calculations were made using the HSE functional, and the basis sets used were the 6-31G(d) for geometry optimization and 6-311G(d,p) for the final energy calculations. 80 *k*-points along the periodic direction in the irreducible Brillouin zone were used (a feat made possible using a Gaussian basis set). The resulting bands are shown in Figure 5.11. The shape of the bands are qualitatively similar to those in Figure 5.5. However, the most important fact is the similarity between the optical band gaps as calculated by BSE, and the DFT HSE band gaps, with differences of 0.02 eV and 0.00 eV for single and bilayer H-GNRs respectively. In order to study the sensitivity of the optical band gap to shifting their relative positions and the effects of wrapping the GNRs, we used the HSE functional in what follows, and, unless otherwise specified, the band gaps are calculated by DFT using the HSE functional.

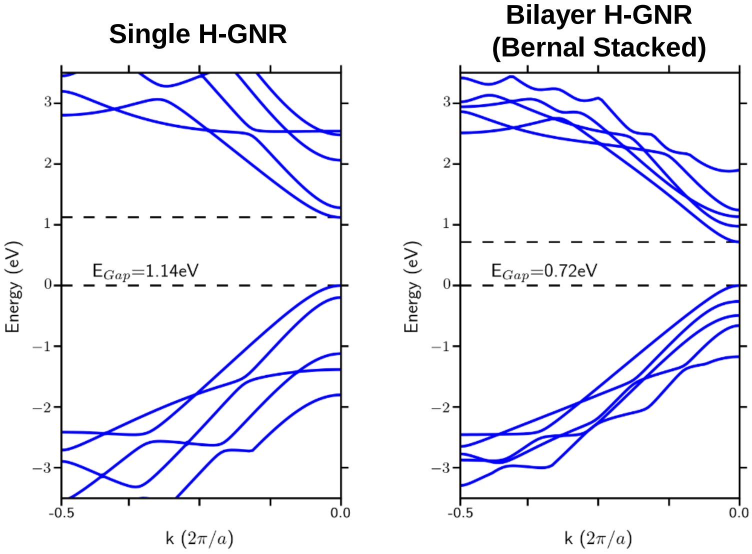

Figure 5.11: DFT HSE band diagrams of single and bilayer H-GNRs. $a$ is the lattice parameter, and the energy is set to 0 at the maximum value of the valence band.

It is already clear that the band gap is greatly affected by aggregation. In fact, stacking additional H-GNRs decreases the band-gap further, to 0.58 eV for trilayer GNRs. In addition, the band gap changed substantially with respect to how the GNRs are oriented with respect to each other. Figure 5.12 shows how laterally shifting H-GNRs, as well as changing their separation distance, can greatly alter the band gap. Shifting the GNRs in the x- direction alone causes the band gap to cover a range of values over 0.5 eV wide. Bernal stacking for bilayer GNRs was an assumption, and since the band gap is very sensitive with respect to the relative positioning of the GNRs, it is likely that the actual band gap of the bilayer GNRs is quite different from that previously calculated. Also, if aggregation occurred imperfectly, it can reasonably be expected that there was some ensemble of band gaps present in the bulk material.

One thing the hexa(ethylene oxide) side-chains can do that the methoxy side-chains cannot is wrap around the GNR. In Chapters 3 and 4, it was shown that the PEG chains rarely adsorb on the GNR to which it is attached in solution. However, this is not true in air or vacuum. For comparison to an unwrapped structure, the band structure of the MeO-GNRs was calculated with the HSE functional. 40 *k*-points were used, and the HSE band gap was calculated to be 1.06 eV. This is close to the calculated optical band-gap (1.15 eV), but it shows that the HSE functional band gap does not perfectly match BSE results.

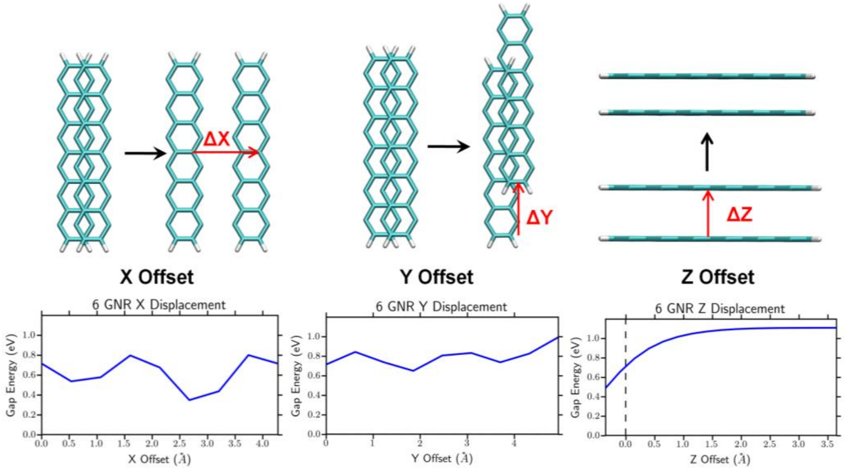

Figure 5.12: Band gaps calculated by shifting H-GNRs relative to each other in each of the x-, y- and z- directions shown schematically on the top row and the band gaps as a function of offset shown in the bottom row. An offset of 0.0 indicates the Bernal stacking used in the main text.

Simulating the full side-chain would be computationally expensive, so a small PEG oligomer was used instead. To calculate the separation distance between MeO-GNR and a PEG chain, we first optimized the geometry of the PEG chain adsorbed on MeOH using Avogadro with the MMFF94 force field [121, 122]. The average distance between the centers of mass of the PEG and GNR carbon atoms was used to determine the separation distance (3.67 Å). We then optimized the structure of the PEG chain without periodic boundary conditions, and finally placed the optimized structure 3.67 Å above the optimized MeO-GNR structure used for Figure 5.13. This final structure was used as input to calculate the electronic structure *via* DFT, and this structure and the resulting bands are shown in Figure 5.14. The band gap is identical to the MeO-GNR that did not have a PEG chain adsorbed. The bands are almost identical as well, with the exception of the lowest energy valence bands. The HOMO of the PEG chain is 2.58 eV below that of the maximum energy of the valence band in MeO-GNR, and the LUMO is 5.14 eV above the minimum energy of the conduction band in MeO-GNR. Therefore, wrapping is not expected to significantly alter the band gap of the material.

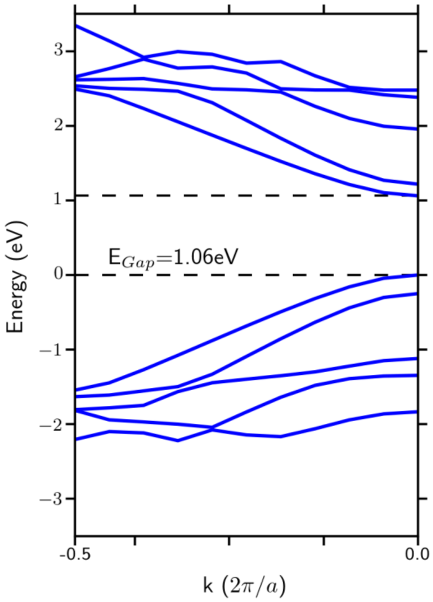

Figure 5.13: DFT HSE band diagrams of a single MeO-GNR. *a* is the lattice parameter, and the energy is set to 0 at the maximum value of the valence band.

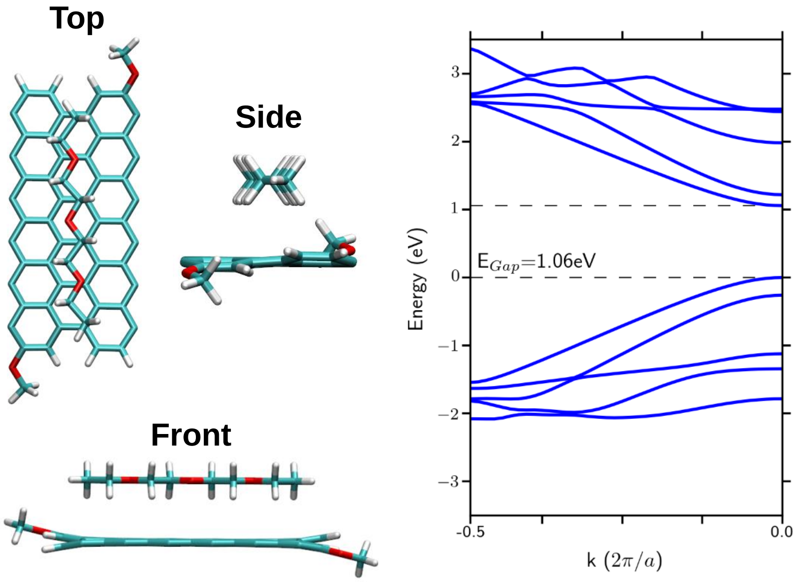

Figure 5.14: DFT HSE band diagram of a single MeO-GNR with an adsorbed PEG chain. *a* is the lattice parameter, and the energy is set to 0 at the maximum value of the valence band.

## 5.3 Discussion

A major conclusion in the studies in this Chapter is that stacking the GNRs causes significant changes in the band gap. In contrast, the effect on the band gap due to the side-chains is small. In addition, if the GNRs are irregularly stacked, the band gap itself might also be irregular along the channel between source and drain contacts. This, and the possibility that no single GNR connects the source and drain electrodes, explains the Arrhenius behavior of the electronic mobility in the work by Gao *et al.* [1]. While other studies have performed DFT calculations to a more limited extent with different functionals [123, 124], the correlation of the HSE functional results to the BSE results provides a indirect method to estimate quantitative differences in the optical band gap.

Previous studies comparing BSE results with experimental results involving GNRs have shown that BSE calculations can provide very accurate optical band gaps. While the results produced here for MeO-GNRs are close to those calculated by experiment, there are some significant differences. This could be due to the fact that there are differences in the process of fluorescence and the spectrum that the calculations describe or that the solvent is expected to shift the peaks. In addition, the calculations had to be made at a lower precision than ideal due to limitations in the computational power available. In the future, more precise calculations could be made if considerably more expansive computational resources were made available to ensure that the later problem is not the source of the difference between the experimental and calculated spectra.

# CHAPTER 6

# CONCLUSIONS AND FUTURE WORK

With the interest in producing GNRs and other large polyaromatic molecules, the goal of the work within this dissertation was to build a atomic-level picture describing how various edge-configurations act to disperse these molecules. Ideally, molecular modeling methods could be used to test various edge configurations prior to synthesis to speed the fabrication process along. To achieve these goals, this dissertation has offered a multistage process that studied a large number of possible edge-configurations in a first (fast) triage of candidate configurations, and then examined more promising configurations in greater detail with costlier free-energy calculations.

First, many edge configurations were quickly simulated in order to calculate binding enthalpies as well as the disposition of the side-chains. This provided qualitative information that describes how different side-chains and grafting densities would affect aggregation. It was found that bulky side-groups caused the GNRs to contort when they aggregate, making binding enthalpically unfavorable. In addition, not all side-chains were effective. Linear *n*-alkoxy side-chains with grafting density values of $D_G$ of 2 or greater effectively increased the surface area of the GNRs. This greatly increased the binding enthalpy as the chains increased in length.

Second, more computationally expensive free energy calculations were conducted on three GNR variants: hydrogen-terminated GNRs, PEG-terminated GNRs, and *n*-alkoxy-terminated GNRs (both side-chain terminated GNRs had a $D_G$ value of 1). While finding the correct aggregation path was determined to be infeasible, choosing two completely different, but plausible, paths (face-to-face and sliding) showed that similar trends existed for both side-chain types for both paths. It was determined that the PEG chains performed the best in terms of increasing the energy barrier to aggregation, while the *n*-alkoxy chains were the worst. In fact, the *n*-alkoxy chains completely removed the barrier to aggregation in the sliding aggregation path.

Finally, following the work of experimental collaborators, we investigated the effects of aggregation and side-chains on the electronic properties of GNRs. While the chains play little role in changing the band gap, aggregation can have large and unpredictable effects, further supporting the fact that more work needs to be done to disperse the GNRs.

The free energy calculations were prohibitively expensive, and improvements need to be made to use them as a screening method. One possibility is to examine only the range of separation distances where the maximum barrier is likely to be found, greatly reducing the number of simulations that are required to be made. Second, if there is some intuition about how long a system needs to be run in order for it to fully equilibrate, this can be used in order to avoid having to do TI calculations with simulations initialized both from GNR being brought together and pulled apart. As an alternative to more quickly screening the GNRs, better aggregation paths can be found by slowly increasing the number of degrees of freedom of the GNRs. In addition, rare event sampling such as forward flux sampling could be attempted to provide a better estimate of the rates. However, it is expected that using a method like this would be very computationally expensive because all degrees of freedom for the GNR would have to be allowed to be free to manipulate.

The greatest improvement that can be made with the electronic structure calculations would be to obtain additional computational resources to make expensive $G_0W_0$ and BSE calculations more feasible. If the features of the fluorescence spectrum can be matched to results from the BSE calculations, a "fingerprint" for different levels of aggregation could be devised to determine the relative population of the different aggregate structures could be determined from experimentally produced fluorescence spectra.

# APPENDIX A

## ALL SINGLE GNR HEAT MAPS

The following figures show all the single-ribbon heat maps that were generated for each GNR configuration in the same way that those in Figures 3.3 and 3.4 in the main text.

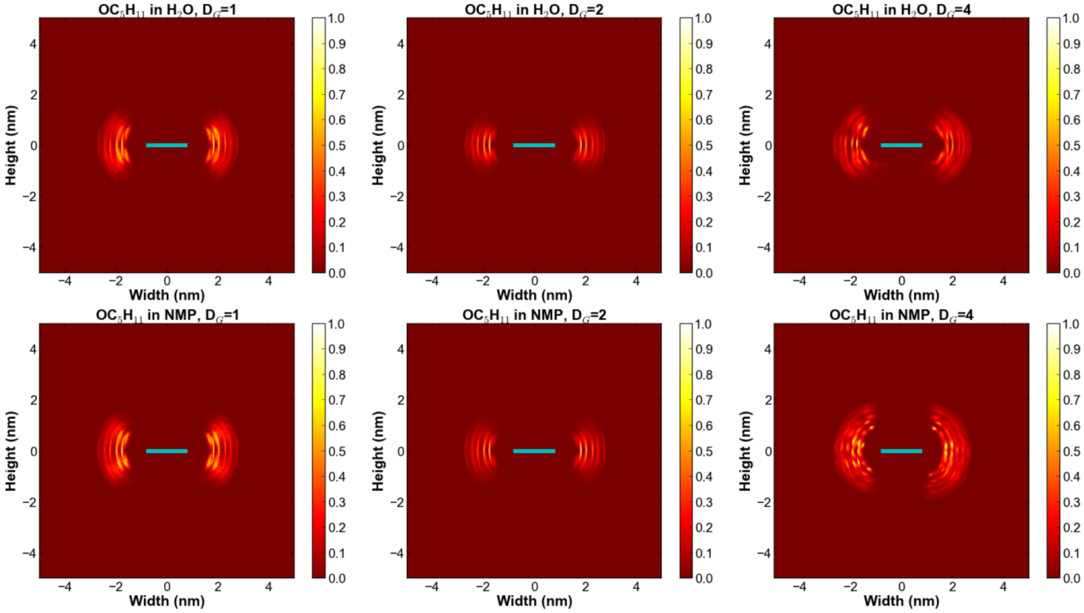

Figure A.1: Heat maps for single GNRs with OC$_5$H$_{11}$ side-chains.

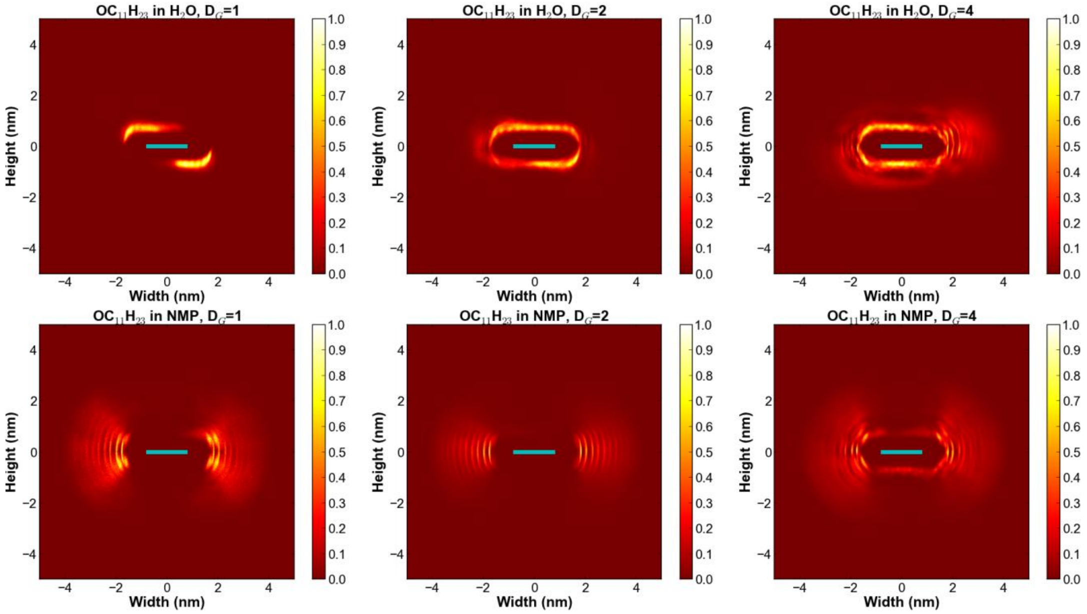

Figure A.2: Heat maps for single GNRs with $OC_{11}H_{23}$ side-chains.

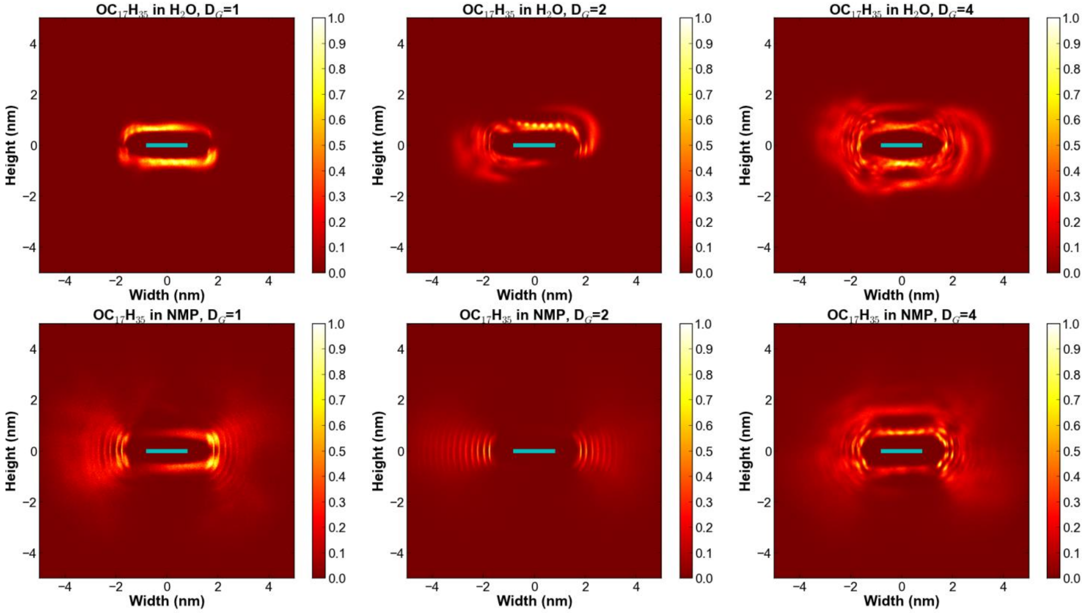

Figure A.3: Heat maps for single GNRs with OC$_{17}$H$_{35}$ side-chains.

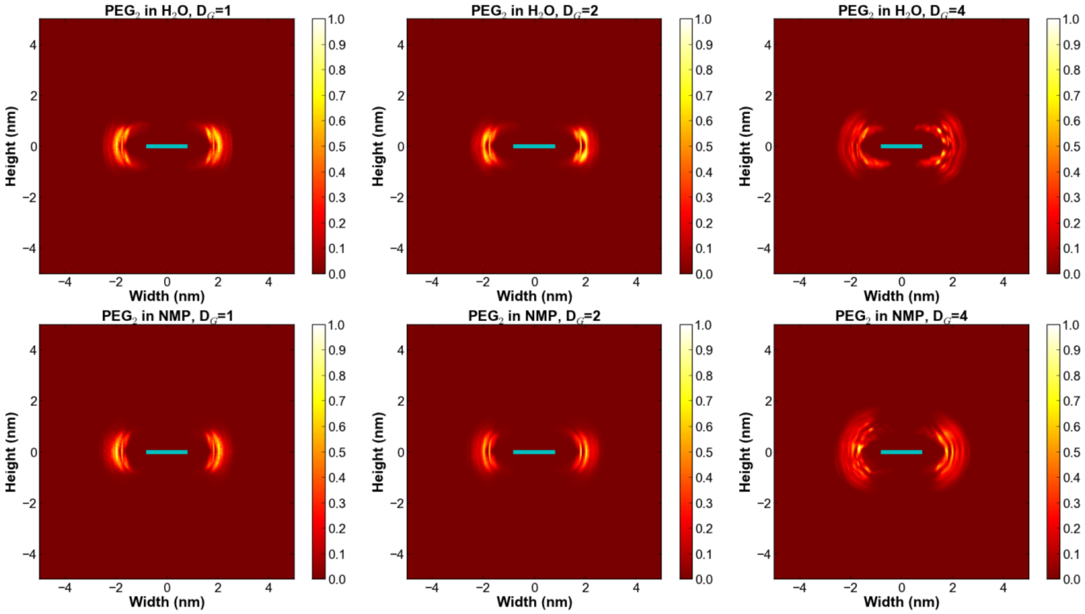

Figure A.4: Heat maps for single GNRs with PEG$_2$ side-chains.

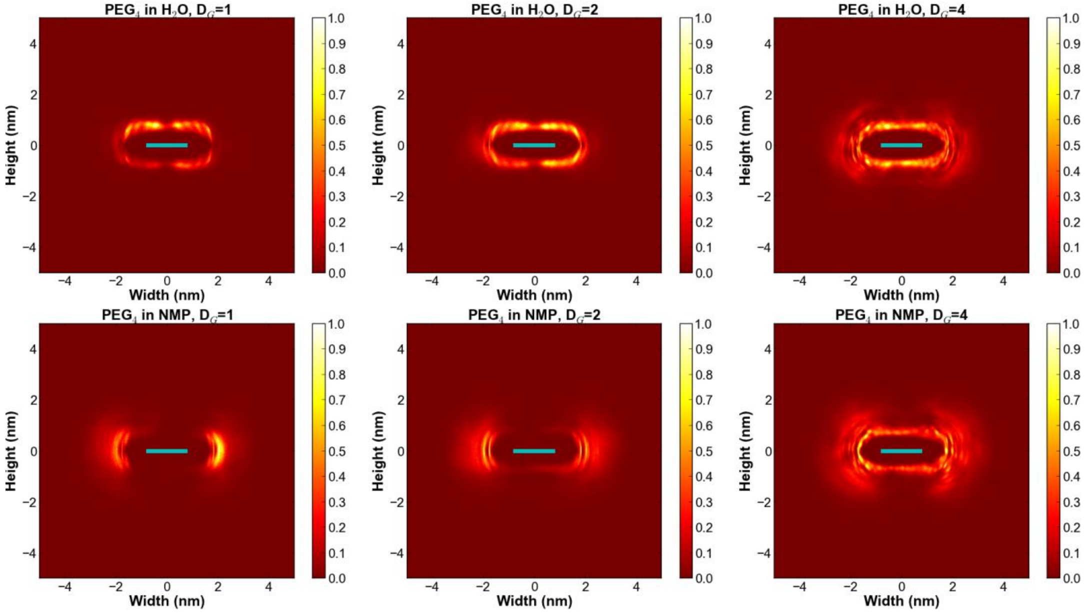

Figure A.5: Heat maps for single GNRs with $PEG_4$ side-chains.

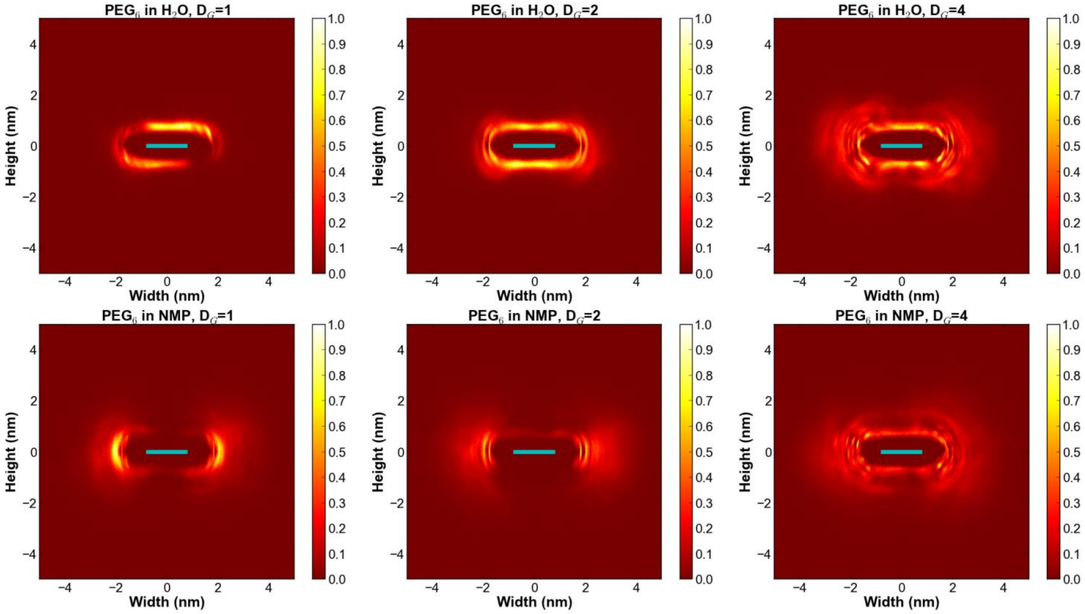

Figure A.6: Heat maps for single GNRs with PEG$_6$ side-chains.

# APPENDIX B

# $G_0W_0$/BSE CALCULATIONS

Here, the input scripts for the various steps in calculating $G_0W_0$ quasiparticle energies and BSE derived spectra are given for the H-GNR system.

## B.1 Geometry Optimization

This is the first step, and Quantum Espresso is used to optimize the the geometry of the GNR:

```
&control
   calculation = 'vc-relax'
   verbosity = 'high'
   restart_mode='from_scratch',
   prefix='6GNR',
   pseudo_dir = '../Pseudo',
   outdir='./Backup',
   forc_conv_thr=7.8d-3
/
&system
   ibrav=  14, a=37.81, b=4.26, c=21.16, cosAB=0.0, cosAC=0.0, cosBC=0.0, nat=  30, ntyp= 2,
   ecutwfc=30.0, ecutrho=150.0
/
&electrons
   electron_maxstep=200
   diagonalization='cg'
   mixing_mode = 'plain'
   mixing_beta = 0.7
   conv_thr =  7.4d-7
/
/
&ions
   ion_dynamics= 'bfgs'
```

```
 /
 &cell
    cell_dofree= 'y'
 /
 ATOMIC_SPECIES
  H 1.008 H.pbe-mt_fhi.UPF
  C 12.011 C.pbe-mt_fhi.UPF
 ATOMIC_POSITIONS ANGSTROM
C 0.94396769 0.71 0
C 3.403479837 0.71 0
C 5.862991984 0.71 0
C 8.32250413 0.71 0
C 10.78201628 0.71 0
C 13.24152842 0.71 0
C 15.70104057 0.71 0
C 0.94396769 2.13 0
C 3.403479837 2.13 0
C 5.862991984 2.13 0
C 8.32250413 2.13 0
C 10.78201628 2.13 0
C 13.24152842 2.13 0
C 15.70104057 2.13 0
C 2.173723763 0 0
C 4.63323591 0 0
C 7.092748057 0 0
C 9.552260204 0 0
C 12.01177235 0 0
C 14.4712845 0 0
C 2.173723763 2.84 0
C 4.63323591 2.84 0
C 7.092748057 2.84 0
C 9.552260204 2.84 0
C 12.01177235 2.84 0
C 14.4712845 2.84 0
H 0 0.165 0
H 0 2.675 0
H 16.64500826 0.165 0
H 16.64500826 2.675 0
 K_POINTS AUTOMATIC
```

```
 1 32 1 0 0 0
END
```

## B.2 SCF Calculation

On this step, and SCF calculation is done on the output geometry from the previous one to obtain LDA energies using Quantum Espresso:

```
&control
    calculation = 'scf'
    verbosity = 'high'
    restart_mode='from_scratch',
    prefix='6GNR',
    pseudo_dir = '../Pseudo',
    outdir='./Backup',
    wf_collect=.true.
 /
 &system
    ibrav=  14, a=37.81, b=4.134, c=21.16, cosAB=0.0, cosAC=0.0, cosBC=0.0, nat=  30, ntyp= 2,
    ecutwfc=30.0, ecutrho=120.0
 /
 &electrons
    electron_maxstep=200
    diagonalization='cg'
    mixing_mode = 'plain'
    mixing_beta = 0.7
    conv_thr =  7.4d-7
 /
 ATOMIC_SPECIES
  H 1.008 H.pw-mt_fhi.UPF
  C 12.011 C.pw-mt_fhi.UPF
 ATOMIC_POSITIONS ANGSTROM
C        0.944447741   0.701569002   0.000000000
C        3.388068927   0.680912078   0.000000000
C        5.857542625   0.681556381   0.000000000
```

```
C        8.322621995   0.683833112   0.000000000
C       10.787381025   0.681730800   0.000000000
C       13.256957258   0.681404844   0.000000000
C       15.700359904   0.702110203   0.000000000
C        0.944349585   2.047233485   0.000000000
C        3.388158285   2.068123136   0.000000000
C        5.857566519   2.068312188   0.000000000
C        8.322585604   2.066398259   0.000000000
C       10.787262283   2.068438617   0.000000000
C       13.257151929   2.068521010   0.000000000
C       15.700673988   2.047699947   0.000000000
C        2.158912476   0.009388503   0.000000000
C        4.625088479   0.002454055   0.000000000
C        7.087837124   0.005931319   0.000000000
C        9.557227816   0.005932661   0.000000000
C       12.019942472   0.002842846   0.000000000
C       14.486041418   0.009818706   0.000000000
C        2.159032158   2.739489172   0.000000000
C        4.625200687   2.746904450   0.000000000
C        7.087859459   2.744229783   0.000000000
C        9.557206123   2.744242683   0.000000000
C       12.019824630   2.747216972   0.000000000
C       14.485988460   2.739997462   0.000000000
H       -0.007309611   0.178560438   0.000000000
H       -0.007369633   2.570517522   0.000000000
H       16.652129115   0.179090464   0.000000000
H       16.652385070   2.570864716   0.000000000
 K_POINTS AUTOMATIC
 1 32 1 0 0 0
END
```

## B.3 NSCF Calculations

Non-SCF calculations are made based on the SCF electronic density to format the data in an appropriate way for Yambo and to create empty bands:

```
&control
    calculation = ’nscf’
    verbosity = ’high’
    restart_mode=’restart’,
    prefix=’6GNR’,
    pseudo_dir = ’../Pseudo’,
    outdir=’./Backup’,
    wf_collect=.true.
 /
 &system
    ibrav=  14, a=37.81, b=4.134, c=21.16, cosAB=0.0, cosAC=0.0, cosBC=0.0, nat=  30, ntyp= 2, nbnd= 154
    ecutwfc=30.0, ecutrho=120.0, force_symmorphic=.true.
 /
 &electrons
    electron_maxstep=200
    diagonalization=’cg’
    mixing_mode = ’plain’
    mixing_beta = 0.7
    conv_thr =  7.4d-7
 /
 ATOMIC_SPECIES
  H 1.008 H.pw-mt_fhi.UPF
  C 12.011 C.pw-mt_fhi.UPF
 ATOMIC_POSITIONS ANGSTROM
C        0.944447741   0.701569002   0.000000000
C        3.388068927   0.680912078   0.000000000
C        5.857542625   0.681556381   0.000000000
C        8.322621995   0.683833112   0.000000000
C       10.787381025   0.681730800   0.000000000
C       13.256957258   0.681404844   0.000000000
C       15.700359904   0.702110203   0.000000000
C        0.944349585   2.047233485   0.000000000
C        3.388158285   2.068123136   0.000000000
C        5.857566519   2.068312188   0.000000000
C        8.322585604   2.066398259   0.000000000
C       10.787262283   2.068438617   0.000000000
C       13.257151929   2.068521010   0.000000000
C       15.700673988   2.047699947   0.000000000
C        2.158912476   0.009388503   0.000000000
```

```
C        4.625088479   0.002454055   0.000000000
C        7.087837124   0.005931319   0.000000000
C        9.557227816   0.005932661   0.000000000
C       12.019942472   0.002842846   0.000000000
C       14.486041418   0.009818706   0.000000000
C        2.159032158   2.739489172   0.000000000
C        4.625200687   2.746904450   0.000000000
C        7.087859459   2.744229783   0.000000000
C        9.557206123   2.744242683   0.000000000
C       12.019824630   2.747216972   0.000000000
C       14.485988460   2.739997462   0.000000000
H       -0.007309611   0.178560438   0.000000000
H       -0.007369633   2.570517522   0.000000000
H       16.652129115   0.179090464   0.000000000
H       16.652385070   2.570864716   0.000000000
 K_POINTS AUTOMATIC
 1 32 1 0 0 0
END
```

## B.4 $G_0W_0$ Calculations with RIM for Coulombic Cut-Off

Two steps for initializing the Quantum Espresso data were skipped because they were trivial (two single commands, “p2y” and “yambo”, used in the terminal). In this step, the RIM method is used and the $G_0W_0$ calculations are executed:

```
#             GPL Version 3.4.1 Revision 3187
#                http://www.yambo-code.org
#
rim_cut                       # [R RIM CUT] Coulomb interaction
ppa                           # [R Xp] Plasmon Pole Approximation
gw0                           # [R GW] GoWo Quasiparticle energy levels
HF_and_locXC                  # [R XX] Hartree-Fock Self-energy and Vxc
em1d                          # [R Xd] Dynamical Inverse Dielectric Matrix
RandQpts= 10000000            # [RIM] Number of random q-points in the BZ
```

```
RandGvec= 203          RL    # [RIM] Coulomb interaction RS components
CUTGeo= "box xz"             # [CUT] Coulomb Cutoff geometry: box/cylinder/sphere
% CUTBox
 71.47600 |  0.00000 | 40.00000 |        # [CUT] [au] Box sides
%
CUTRadius= 0.000000          # [CUT] [au] Sphere/Cylinder radius
CUTCylLen= 0.000000          # [CUT] [au] Cylinder length
EXXRLvcs=  30      Ry    # [XX] Exchange RL components
Chimod= "Hartree"                   # [X] IP/Hartree/ALDA/LRC/BSfxc
% BndsRnXp
   1 | 104 |                 # [Xp] Polarization function bands
%
NGsBlkXp= 2            Ry    # [Xp] Response block size
% LongDrXp
 0.000000 | 1.000000 | 0.000000 |        # [Xp] [cc] Electric Field
%
PPAPntXp= 27.21138     eV    # [Xp] PPA imaginary energy
% GbndRnge
   1 | 104 |                 # [GW] G[W] bands range
%
GDamping= 0.100000     eV    # [GW] G[W] damping
dScStep= 0.100000      eV    # [GW] Energy step to evalute Z factors
DysSolver= "n"               # [GW] Dyson Equation solver (`n`,`s`,`g`)
%QPkrange                    # [GW] QP generalized Kpoint/Band indices
  1| 17| 45| 64|
%
%QPerange                    # [GW] QP generalized Kpoint/Energy indices
  1| 17| 0.0|-1.0|
%
```

## B.5 Static Inverse Dielectric Matrix Calculation

This uses the NSCF results to produce the Static Inverse Dielectric Matrix used as input for the BSE calculations in Yambo:

```
#             GPL Version 3.4.1 Revision 3187
```

```
#                http://www.yambo-code.org
#
rim_cut                      # [R RIM CUT] Coulomb interaction
em1s                         # [R Xs] Static Inverse Dielectric Matrix
RandQpts= 10000000           # [RIM] Number of random q-points in the BZ
RandGvec= 203          RL    # [RIM] Coulomb interaction RS components
CUTGeo= "box xz"             # [CUT] Coulomb Cutoff geometry: box/cylinder/sphere
% CUTBox
 71.47600 |  0.00000 | 40.00000 |        # [CUT] [au] Box sides
%
Chimod= "hartree"            # [X] IP/Hartree/ALDA/LRC/BSfxc
% BndsRnXs
   1 | 104 |                 # [Xs] Polarization function bands
%
NGsBlkXs= 2            Ry    # [Xs] Response block size
% LongDrXs
 0.000000 | 1.000000 | 0.000000 |        # [Xs] [cc] Electric Field
%
```

## B.6 BSE Calculations

This uses the $G_0W_0$ and the Static Inverse Dielectric Matrix as input to the BSE to produce absorption/fluoresence spectra. This script is for singlet excitations:

```
#             GPL Version 3.4.1 Revision 3187
#                http://www.yambo-code.org
#
rim_cut                      # [R RIM CUT] Coulomb interaction
optics                       # [R OPT] Optics
bse                          # [R BSE] Bethe Salpeter Equation.
bsk                          # [R BSK] Bethe Salpeter Equation kernel
em1s                         # [R Xs] Static Inverse Dielectric Matrix
bss                          # [R BSS] Bethe Salpeter Equation solver
RandQpts= 10000000           # [RIM] Number of random q-points in the BZ
RandGvec= 203          RL    # [RIM] Coulomb interaction RS components
CUTGeo= "box xz"             # [CUT] Coulomb Cutoff geometry: box/cylinder/sphere
% CUTBox
```

```
 71.47600 |  0.00000 | 40.00000 |        # [CUT] [au] Box sides
%
Chimod= "hartree"            # [X] IP/Hartree/ALDA/LRC/BSfxc
BSEmod= "resonant"             # [BSE] resonant/causal/coupling
BSKmod= "SEX"                # [BSE] IP/Hartree/HF/ALDA/SEX
BSSmod= "d"                  # [BSS] (h)aydock/(d)iagonalization/(i)nversion/(t)ddft`
BSENGexx= 30      Ry    # [BSK] Exchange components
BSENGBlk= 2         Ry    # [BSK] Screened interaction block size
#WehCpl                      # [BSK] eh interaction included also in coupling
KfnQPdb= "E < ./SAVE/db.QP"              # [EXTQP BSK BSS] Database
KfnQP_N= 1                   # [EXTQP BSK BSS] Interpolation neighbours
KfnQP_Z= ( 1.000000 , 0.000000 )      # [EXTQP BSK BSS] Z factor  (c/v)
% BEnRange
  0.00000 | 2.00000 | eV    # [BSS] Energy range
%
% BDmRange
 0.020000 | 0.020000 | eV    # [BSS] Damping range
%
BEnSteps= 1000                # [BSS] Energy steps
% BLongDir
 0.000000 | 1.000000 | 0.000000 |        # [BSS] [cc] Electric Field
%
% BSEBands
   45 | 64 |                 # [BSK] Bands range
%
% BndsRnXs
   1 | 104 |                 # [Xs] Polarization function bands
%
NGsBlkXs= 1081         RL    # [Xs] Response block size
% LongDrXs
 0.000    |0.1000E-4 | 0.000    |        # [Xs] [cc] Electric Field
%
WRbsWF
```

# BIBLIOGRAPHY

[1] Gao, J.; Uribe-Romo, F. J.; Saathoff, J. D.; Arslan, H.; Crick, C. R.; Hein, S. J.; Itin, B.; Clancy, P.; Dichtel, W. R.; Loo, Y.-L. *ACS Nano* **2016**.

[2] Novoselov, K. S.; Geim, A. K.; Morozov, S. V.; Jiang, D.; Zhang, Y.; Dubonos, S. V.; Grigorieva, I. V.; Firsov, A. A. *Science* **2004**, *306*, 666–669.

[3] Fasolino, A.; Los, J.; Katsnelson, M. I. *Nat. Mater.* **2007**, *6*, 858–861.

[4] Novoselov, K.; Jiang, D.; Schedin, F.; Booth, T.; Khotkevich, V.; Morozov, S.; Geim, A. *Proc. Natl. Acad. Sci. USA* **2005**, *102*, 10451–10453.

[5] Novoselov, K. S.; Fal, V.; Colombo, L.; Gellert, P.; Schwab, M.; Kim, K.; et al. *Nature* **2012**, *490*, 192–200.

[6] Nicolosi, V.; Chhowalla, M.; Kanatzidis, M. G.; Strano, M. S.; Coleman, J. N. *Science* **2013**, *340*, 1226419.

[7] Morozov, S.; Novoselov, K.; Katsnelson, M.; Schedin, F.; Elias, D.; Jaszczak, J.; Geim, A. *Phys. Rev. Lett.* **2008**, *100*, 016602.

[8] Mayorov, A. S.; Gorbachev, R. V.; Morozov, S. V.; Britnell, L.; Jalil, R.; Ponomarenko, L. A.; Blake, P.; Novoselov, K. S.; Watanabe, K.; Taniguchi, T.; et al. *Nano Lett.* **2011**, *11*, 2396–2399.

[9] Moser, J.; Barreiro, A.; Bachtold, A. *Appl. Phys. Lett.* **2007**, *91*, 163513.

[10] Lee, C.; Wei, X.; Kysar, J. W.; Hone, J. *Science* **2008**, *321*, 385–388.

[11] Nair, R.; Blake, P.; Grigorenko, A.; Novoselov, K.; Booth, T.; Stauber, T.; Peres, N.; Geim, A. *Science* **2008**, *320*, 1308–1308.

[12] Balandin, A. A. *Nat. Mater.* **2011**, *10*, 569–581.

[13] Hernandez, Y.; Nicolosi, V.; Lotya, M.; Blighe, F. M.; Sun, Z.; De, S.; McGovern, I.; Holland, B.; Byrne, M.; Gun'Ko, Y. K.; et al. *Nat. Nanotechnol.* **2008**, *3*, 563–568.

[14] Dreyer, D. R.; Ruoff, R. S.; Bielawski, C. W. *Angew. Chem. Int. Ed.* **2010**, *49*, 9336–9344.

[15] Schniepp, H. C.; Li, J.-L.; McAllister, M. J.; Sai, H.; Herrera-Alonso, M.; Adamson, D. H.; Prud'homme, R. K.; Car, R.; Saville, D. A.; Aksay, I. A. *J. Phys. Chem. B* **2006**, *110*, 8535–8539.

[16] Li, X.; Cai, W.; An, J.; Kim, S.; Nah, J.; Yang, D.; Piner, R.; Velamakanni, A.; Jung, I.; Tutuc, E.; et al. *Science* **2009**, *324*, 1312–1314.

[17] Forbeaux, I.; Themlin, J.-M.; Debever, J.-M. *Phys. Rev. B* **1998**, *58*, 16396.

[18] Berger, C.; Song, Z.; Li, T.; Li, X.; Ogbazghi, A. Y.; Feng, R.; Dai, Z.; Marchenkov, A. N.; Conrad, E. H.; First, P. N.; et al. *J. Phys. Chem. B* **2004**, *108*, 19912–19916.

[19] Ohta, T.; Bostwick, A.; Seyller, T.; Horn, K.; Rotenberg, E. *Science* **2006**, *313*, 951–954.

[20] Bae, S.; Kim, H.; Lee, Y.; Xu, X.; Park, J.-S.; Zheng, Y.; Balakrishnan, J.; Lei, T.; Kim, H. R.; Song, Y. I.; et al. *Nat. Nanotechnol.* **2010**, *5*, 574–578.

[21] Lin, Y.-M.; Dimitrakopoulos, C.; Jenkins, K. A.; Farmer, D. B.; Chiu, H.-Y.; Grill, A.; Avouris, P. *Science* **2010**, *327*, 662–662.

[22] Schwierz, F. *Nat. Nanotechnol.* **2010**, *5*, 487–496.

[23] Yoo, E.; Kim, J.; Hosono, E.; Zhou, H.-s.; Kudo, T.; Honma, I. *Nano Lett.* **2008**, *8*, 2277–2282.

[24] Young, R. J.; Kinloch, I. A.; Gong, L.; Novoselov, K. S. *Compos. Sci. Technol.* **2012**, *72*, 1459–1476.

[25] Wallace, P. R. *Phys. Rev.* **1947**, *71*, 622.

[26] Neto, A. C.; Guinea, F.; Peres, N.; Novoselov, K. S.; Geim, A. K. *Rev. Mod. Phys.* **2009**, *81*, 109.

[27] Semenoff, G. W. *Phys. Rev. Lett.* **1984**, *53*, 2449.

[28] Haldane, F. D. M. *Phys. Rev. Lett.* **1988**, *61*, 2015.

[29] Gava, P.; Lazzeri, M.; Saitta, A. M.; Mauri, F. *Phys. Rev. B* **2009**, *79*, 165431.

[30] Castro, E. V.; Novoselov, K.; Morozov, S.; Peres, N.; Dos Santos, J. L.; Nilsson, J.; Guinea, F.; Geim, A.; Neto, A. C. *Phys. Rev. Lett.* **2007**, *99*, 216802.

[31] Pereira, V. M.; Neto, A. C.; Peres, N. *Phys. Rev. B* **2009**, *80*, 045401.

[32] Zhou, S.; Gweon, G.-H.; Fedorov, A.; First, P.; De Heer, W.; Lee, D.-H.; Guinea, F.; Neto, A. C.; Lanzara, A. *Nat. Mater.* **2007**, *6*, 770–775.

[33] Yang, L.; Park, C.-H.; Son, Y.-W.; Cohen, M. L.; Louie, S. G. *Phys. Rev. Lett.* **2007**, *99*, 186801.

[34] Nakada, K.; Fujita, M.; Dresselhaus, G.; Dresselhaus, M. S. *Phys. Rev. B* **1996**, *54*, 17954.

[35] Son, Y.-W.; Cohen, M. L.; Louie, S. G. *Phys. Rev. Lett.* **2006**, *97*, 216803.

[36] Dutta, S.; Pati, S. K. *J. Mater. Chem.* **2010**, *20*, 8207–8223.

[37] Chen, Z.; Lin, Y.-M.; Rooks, M. J.; Avouris, P. *Physica E* **2007**, *40*, 228–232.

[38] Han, M. Y.; Özyilmaz, B.; Zhang, Y.; Kim, P. *Phys. Rev. Lett.* **2007**, *98*, 206805.

[39] Kosynkin, D. V.; Higginbotham, A. L.; Sinitskii, A.; Lomeda, J. R.; Dimiev, A.; Price, B. K.; Tour, J. M. *Nature* **2009**, *458*, 872–876.

[40] Jiao, L.; Zhang, L.; Wang, X.; Diankov, G.; Dai, H. *Nature* **2009**, *458*, 877–880.

[41] Shifrina, Z. B.; Averina, M. S.; Rusanov, A. L.; Wagner, M.; Müllen, K. *Macromolecules* **2000**, *33*, 3525–3529.

[42] Wu, J.; Gherghel, L.; Watson, M. D.; Li, J.; Wang, Z.; Simpson, C. D.; Kolb, U.; Müllen, K. *Macromolecules* **2003**, *36*, 7082–7089.

[43] Yang, X.; Dou, X.; Rouhanipour, A.; Zhi, L.; Rader, H. J.; Mullen, K.

[44] Dössel, L.; Gherghel, L.; Feng, X.; Müllen, K. *Angew. Chem. Int. Ed.* **2011**, *50*, 2540–2543.

[45] Schwab, M. G.; Narita, A.; Hernandez, Y.; Balandina, T.; Mali, K. S.; De Feyter, S.; Feng, X.; Müllen, K. *J. Am. Chem. Soc.* **2012**, *134*, 18169–18172.

[46] Narita, A.; Feng, X.; Hernandez, Y.; Jensen, S. A.; Bonn, M.; Yang, H.; Verzhbitskiy, I. A.; Casiraghi, C.; Hansen, M. R.; Koch, A. H.; et al. *Nat. Chem.* **2014**, *6*, 126–132.

[47] Cai, J.; Ruffieux, P.; Jaafar, R.; Bieri, M.; Braun, T.; Blankenburg, S.; Muoth, M.; Seitsonen, A. P.; Saleh, M.; Feng, X.; et al. *Nature* **2010**, *466*, 470–473.

[48] Otero, G.; Biddau, G.; Sánchez-Sánchez, C.; Caillard, R.; López, M. F.; Rogero, C.; Palomares, F. J.; Cabello, N.; Basanta, M. A.; Ortega, J.; et al. *Nature* **2008**, *454*, 865–868.

[49] Konatham, D.; Bui, K.; Papavassiliou, D.; Striolo, A. *Mol. Phys.* **2011**, *109*, 97–111.

[50] Bergin, S. D.; Nicolosi, V.; Streich, P. V.; Giordani, S.; Sun, Z.; Windle, A. H.; Ryan, P.; Niraj, N. P. P.; Wang, Z.-T. T.; Carpenter, L.; et al. *Adv. Mater.* **2008**, *20*, 1876–1881.

[51] Hernandez, Y.; Lotya, M.; Rickard, D.; Bergin, S. D.; Coleman, J. N. *Langmuir* **2009**, *26*, 3208–3213.

[52] Shih, C.-J.; Lin, S.; Strano, M. S.; Blankschtein, D. *J. Am. Chem. Soc.* **2010**, *132*, 14638–14648.

[53] Fu, C.; Yang, X. *Carbon* **2013**, *55*, 350–360.

[54] Green, A. A.; Hersam, M. C. *Nano Lett.* **2009**, *9*, 4031–4036.

[55] Tummala, N. R.; Striolo, A. *ACS Nano..* **2009**, *3*, 595–602.

[56] Lotya, M.; Hernandez, Y.; King, P. J.; Smith, R. J.; Nicolosi, V.; Karlsson, L. S.; Blighe, F. M.; De, S.; Wang, Z.; McGovern, I.; et al. *J. Am. Chem. Soc.* **2009**, *131*, 3611–3620.

[57] Skaltsas, T.; Karousis, N.; Yan, H.-J.; Wang, C.-R.; Pispas, S.; Tagmatarchis, N. *J. Mater. Chem.* **2012**, *22*, 21507–21512.

[58] May, P.; Khan, U.; Hughes, J. M.; Coleman, J. N. *J. Phys. Chem.C* **2012**, *116*, 11393–11400.

[59] Liang, Y. T.; Hersam, M. C. *Macromol. Chem. Phys.* **2012**, *213*, 1091–1100.

[60] Li, D.; Mueller, M. B.; Gilje, S.; Kaner, R. B.; Wallace, G. G. *Nat. Nanotechnol.* **2008**, *3*, 101–105.

[61] Hamilton, C. E.; Lomeda, J. R.; Sun, Z.; Tour, J. M.; Barron, A. R. *Nano Res.* **2010**, *3*, 138–145.

[62] Fang, M.; Wang, K.; Lu, H.; Yang, Y.; Nutt, S. *J. Mater. Chem.* **2010**, *20*, 1982–1992.

[63] Kastler, M.; Pisula, W.; Wasserfallen, D.; Pakula, T.; Müllen, K. *J. Am. Chem. Soc.* **2005**, *127*, 4286–4296.

[64] Yan, X.; Cui, X.; Li, L.-s. *J. Am. Chem. Soc.* **2010**, *132*, 5944–5945.

[65] Hohenberg, P.; Kohn, W. *Phys. Rev.* **1964**, *136*, B864.

[66] Kohn, W.; Sham, L. J. *Phys. Rev.* **1965**, *140*, A1133.

[67] Hybertsen, M. S.; Louie, S. G. *Phys. Rev. B* **1986**, *34*, 5390.

[68] Rohlfing, M.; Louie, S. G. *Phys. Rev. B* **2000**, *62*, 4927.

[69] Plimpton, S. *J. Comput. Phys.* **1995**, *117*, 1–19.

[70] Hockney, R. W.; Eastwood, J. W. *Computer simulation using particles*; CRC Press, 1988.

[71] Car, R.; Parrinello, M. *Phys. Rev. Lett.* **1985**, *55*, 2471.

[72] Jorgensen, W. L.; Maxwell, D. S.; Tirado-Rives, J. *J. Am. Chem. Soc.* **1996**, *118*, 11225–11236.

[73] Aparicio, S.; Alcalde, R.; Davila, M. J.; Garcia, B.; Leal, J. M. *J. Phys. Chem. B* **2008**, *112*, 11361–11373.

[74] Berendsen, H.; Grigera, J.; Straatsma, T. *J. Phys. Chem.* **1987**, *91*, 6269–6271.

[75] Ryckaert, J.-P.; Ciccotti, G.; Berendsen, H. J. *J. Comput. Phys.* **1977**, *23*, 327–341.

[76] Tummala, N. R.; Striolo, A. *J. Phys. Chem. B* **2008**, *112*, 1987–2000.

[77] Cheng, A.; Steele, W. *J. Chem. Phys.* **1990**, *92*, 3858–3866.

[78] Zacharia, R.; Ulbricht, H.; Hertel, T. *Phys. Rev. B* **2004**, *69*, 155406.

[79] Spanu, L.; Sorella, S.; Galli, G. *Phys. Rev. Lett.* **2009**, *103*, 196401.

[80] Kocman, M.; Pykal, M.; Jurečka, P. *Phys. Chem. Chem. Phys.* **2014**, *16*, 3144–3152.

[81] Frisch, M. J.; Trucks, G. W.; Schlegel, H. B.; Scuseria, G. E.; Robb, M. A.; Cheeseman, J. R.; Scalmani, G.; Barone, V.; Mennucci, B.; Petersson, G. A.; Nakatsuji, H.; Caricato, M.; Li, X.; Hratchian, H. P.; Izmaylov, A. F.; Bloino, J.; Zheng, G.; Sonnenberg, J. L.; Hada, M.; Ehara, M.; Toyota, K.; Fukuda, R.; Hasegawa, J.; Ishida, M.; Nakajima, T.; Honda, Y.; Kitao, O.; Nakai, H.; Vreven, T.; Montgomery, J. A., Jr.; Peralta, J. E.; Ogliaro, F.; Bearpark, M.; Heyd, J. J.; Brothers, E.; Kudin, K. N.; Staroverov, V. N.; Kobayashi, R.; Normand, J.; Raghavachari, K.; Rendell, A.; Burant, J. C.; Iyengar, S. S.; Tomasi, J.; Cossi, M.; Rega, N.; Millam, J. M.; Klene, M.; Knox, J. E.; Cross, J. B.; Bakken, V.; Adamo, C.; Jaramillo, J.; Gomperts, R.; Stratmann, R. E.; Yazyev, O.; Austin, A. J.; Cammi, R.; Pomelli, C.; Ochterski, J. W.; Martin, R. L.; Morokuma, K.; Zakrzewski, V. G.; Voth, G. A.; Salvador, P.; Dannenberg, J. J.; Dapprich, S.; Daniels, A. D.; Farkas, .; Foresman, J. B.; Ortiz, J. V.; Cioslowski, J.; Fox, D. J.; *Gaussian09 Revision E.01*; Gaussian Inc. Wallingford CT 2009.

[82] Becke, A. D. *J. Chem. Phys.* **1993**, *98*, 5648–5652.

[83] Lee, C.; Yang, W.; Parr, R. G. *Phys. Rev. B* **1988**, *37*, 785.

[84] Miehlich, B.; Savin, A.; Stoll, H.; Preuss, H. *Chem. Phys. Lett.* **1989**, *157*, 200–206.

[85] Besler, B. H.; Merz, K. M.; Kollman, P. A. *J. Comput. Chem.* **1990**, *11*, 431–439.

[86] Kudin, K. N.; Scuseria, G. E.; Yakobson, B. I. *Phys. Rev. B* **2001**, *64*, 235406.

[87] Saathoff, J. D.; Clancy, P. *J. Phys. Chem. B* **2015**, *119*, 4766–4776.

[88] Chipot, C.; Pohorille, A. *Free energy calculations*; Springer, 2007.

[89] Carter, E.; Ciccotti, G.; Hynes, J. T.; Kapral, R. *Chem. Phys. Lett.* **1989**, *156*, 472–477.

[90] Oyer, A. J.; Carrillo, J.-M. Y.; Hire, C. C.; Schniepp, H. C.; Asandei, A. D.; Dobrynin, A. V.; Adamson, D. H. *J. Am. Chem. Soc.* **2012**, *134*, 5018–5021.

[91] Darve, E.; Pohorille, A. *J. Chem. Phys.* **2001**, *115*, 9169–9183.

[92] Giannozzi, P.; Baroni, S.; Bonini, N.; Calandra, M.; Car, R.; Cavazzoni, C.; Ceresoli, D.; Chiarotti, G. L.; Cococcioni, M.; Dabo, I.; et al. *J. Phys. Condens. Matter* **2009**, *21*, 395502.

[93] Perdew, J. P.; Burke, K.; Ernzerhof, M. *Phys. Rev. Lett.* **1996**, *77*, 3865.

[94] Heyd, J.; Scuseria, G. E. *J. Chem. Phys.* **2004**, *121*, 1187–1192.

[95] Becke, A. D. *J. Chem. Phys.* **1997**, *107*, 8554–8560.

[96] Jones, R. O.; Gunnarsson, O. *Rev. Mod. Phys.* **1989**, *61*, 689.

[97] Pourfath, M. *The Non-Equilibrium Green's Function Method for Nanoscale Device Simulation*; Springer, 2014.

[98] Hedin, L. *Phys. Rev.* **1965**, *139*, A796.

[99] Onida, G.; Reining, L.; Rubio, A. *Rev. Mod. Phys.* **2002**, *74*, 601.

[100] van Schilfgaarde, M.; Kotani, T.; Faleev, S. *Phys. Rev. Lett.* **2006**, *96*, 226402.

[101] Marini, A.; Hogan, C.; Grüning, M.; Varsano, D. *Comput. Phys. Commun.* **2009**, *180*, 1392–1403.

[102] Sottile, F.; Ph.D. thesis; Ecole Polytechnique X; 2003.

[103] Pang, A. L. J.; Sorkin, V.; Zhang, Y.-W.; Srolovitz, D. J. *Phys. Lett. A* **2012**, *376*, 973–977.

[104] Xu, Z.; Buehler, M. J. *ACS Nano..* **2010**, *4*, 3869–3876.

[105] Uddin, N. M.; Capaldi, F. M.; Farouk, B. *Comput. Mater. Sci.* **2012**, *53*, 133–144.

[106] Walther, J. H.; Jaffe, R. L.; Kotsalis, E.; Werder, T.; Halicioglu, T.; Koumoutsakos, P. *Carbon* **2004**, *42*, 1185–1194.

[107] Barone, V.; Hod, O.; Scuseria, G. E. *Nano Lett.* **2006**, *6*, 2748–2754.

[108] Hughes, J. M.; Hernandez, Y.; Aherne, D.; Doessel, L.; Mullen, K.; Moreton, B.; White, T. W.; Partridge, C.; Costantini, G.; Shmeliov, A.; et al. *J. Am. Chem. Soc.* **2012**, *134*, 12168–12179.

[109] Frenkel, D.; Smit, B. *Understanding molecular simulation: from algorithms to applications*; Academic press, 2001; Vol. 1.

[110] Xu, L.; Yang, X. *J. Colloid Interface Sci.* **2014**, *418*, 66–73.

[111] Prezzi, D.; Varsano, D.; Ruini, A.; Marini, A.; Molinari, E. *Phys. Rev. B* **2008**, *77*, 041404.

[112] Rozzi, C. A.; Varsano, D.; Marini, A.; Gross, E. K.; Rubio, A. *Phys. Rev. B* **2006**, *73*, 205119.

[113] Denk, R.; Hohage, M.; Zeppenfeld, P.; Cai, J.; Pignedoli, C. A.; Söde, H.; Fasel, R.; Feng, X.; Müllen, K.; Wang, S.; et al. *Nat. Commun.* **2014**, *5*.

[114] Aryasetiawan, F.; Gunnarsson, O. *Rep. Prog. Phys.* **1998**, *61*, 237.

[115] Chen, Y.-C.; De Oteyza, D. G.; Pedramrazi, Z.; Chen, C.; Fischer, F. R.; Crommie, M. F. *ACS Nano..* **2013**, *7*, 6123–6128.

[116] Ruffieux, P.; Cai, J.; Plumb, N. C.; Patthey, L.; Prezzi, D.; Ferretti, A.; Molinari, E.; Feng, X.; Müllen, K.; Pignedoli, C. A.; et al. *ACS Nano* **2012**, *6*, 6930–6935.

[117] Kammerlander, D.; Botti, S.; Marques, M. A.; Marini, A.; Attaccalite, C. *Phys. Rev. B* **2012**, *86*, 125203.

[118] Larsen, B. A.; Deria, P.; Holt, J. M.; Stanton, I. N.; Heben, M. J.; Therien, M. J.; Blackburn, J. L. *J. Am. Chem. Soc.* **2012**, *134*, 12485–12491.

[119] Jain, M.; Chelikowsky, J. R.; Louie, S. G. *Phys. Rev. Lett.* **2011**, *107*, 216806.

[120] Kudin, K. N.; Scuseria, G. E. *Phys. Rev. B* **2000**, *61*, 16440.

[121] Hanwell, M. D.; Curtis, D. E.; Lonie, D. C.; Vandermeersch, T.; Zurek, E.; Hutchison, G. R. *J. Cheminform.* **2012**, *4*, 17.

[122] Halgren, T. A. *J. Comput. Chem.* **1996**, *17*, 490–519.

[123] Lam, K.-T.; Liang, G. *Appl. Phys. Lett.* **2008**, *92*, 223106.

[124] Zhong, X.; Pandey, R.; Karna, S. P. *Carbon* **2012**, *50*, 784–790.